Università degli Studi di Ferrara

DOTTORATO DI RICERCA IN
"SCIENZE BIOMEDICHE, ENDOCRINOLOGICHE E NEUROFISIOLOGICHE"

CICLO XXII

COORDINATORE Prof. ALESSANDRO MARTINI

Microgravity affects the hair cell ionic currents of the frog semicircular canals

Settore Scientifico Disciplinare BIO/09

Dottorando
Dott. LEPARULO ALESSANDRO

_____
(firma)

Tutore
Prof. ROSSI MARIA LISA

_____
(firma)

Anni 2006/2009

SUMMARY

INTRODUCTION

Morphology

Vertebrate peripheral vestibular system, also called membranous labyrinth, is an even organ located in the temporal bone. In the frog it comprises: 1) three semicircular canals, that detect head angular accelerations, 2) the utricle and the saccule detecting linear accelerations; 3) amphibian and basilar papillae devoted to a pure auditory function.

The three semicircular canals are positioned orthogonally one to each other and the canal receptors, the hair cells, are located in an enlargement of the canal called ampulla. In the ampulla the hair cells constitute, with supporting and basal cells, the crista ampullaris. The crista is partially embedded in a mucopolisaccaridic structure: the cupula. The labyrinth is filled with endolymph, a fluid having a high potassium concentration. Endolymph bathes the apical membrane of the vestibular receptors, whose basolateral membrane is in contact with perilymph, a fluid whose composition is similar to that of the extracellular fluids.

Vestibular receptors are called hair cells owing to the presence of ciliary processes on their apical membrane. Hair cells have two types of cilia: a single kinocilium, located eccentrically, and the stereocilia, whose number largely varies in the different organs and whose height decreases on increasing their distance from the kinocilium. Between kinocilium and stereocilia as well as among adjacent stereocilia are present the so called 'tip links' that plays an important role in the mechano-electrical transduction process. The distal portion of the cilia are inserted into the cupula.

First order neurons contacting the hair cells belong to the VIII nerve. In its proximal part the diameter of the VIII nerve increases owing to the presence of the soma of bipolar cells constituting the Scarpa ganglion.

Morphological studies have revealed in the frog only a type of hair cells, called type II and the presence of two types of synapses in the basolateral hair cell membrane: afferent synapses in which the nerve terminals of the VIII nerve afferent fibres represent the post-synaptic elements (synaptic vesicles are present in the hair cells near the synaptic contacts); efferent synapses (the nerve terminals possess a large number of vesicles and belong to central neurons), in which the postsynaptic element is represented by the hair cells (Mammalian Vestibular Physiology, Eds. VJ Wilson and G Melvill Jones, Plenum Press, NY 1979, pages 5-39). The activation of the efferent pathway exerts either excitation or inhibition of the afferent discharge (Rossi et al., 1980; Rossi and Martini, 1991).

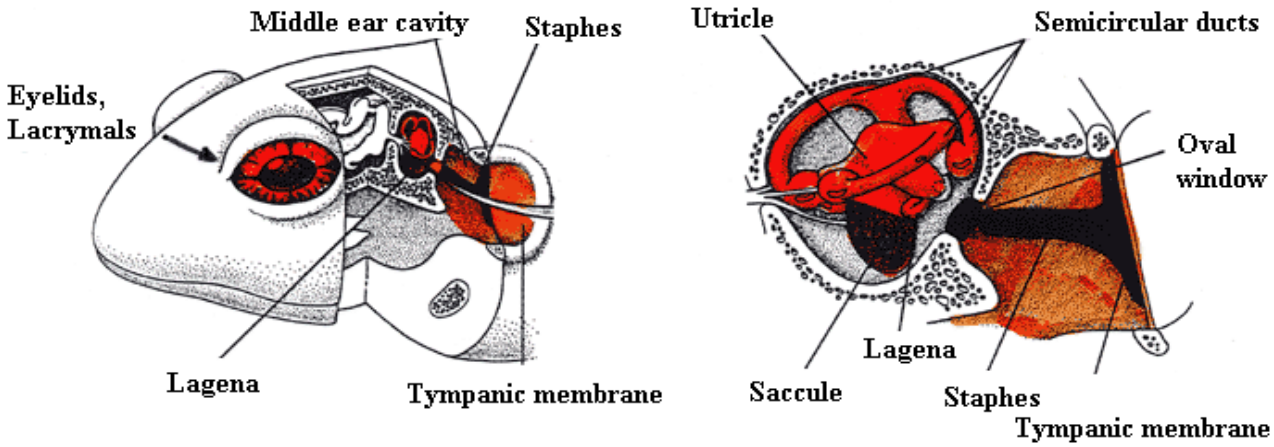

Fig. 1. The frog head and its ear.

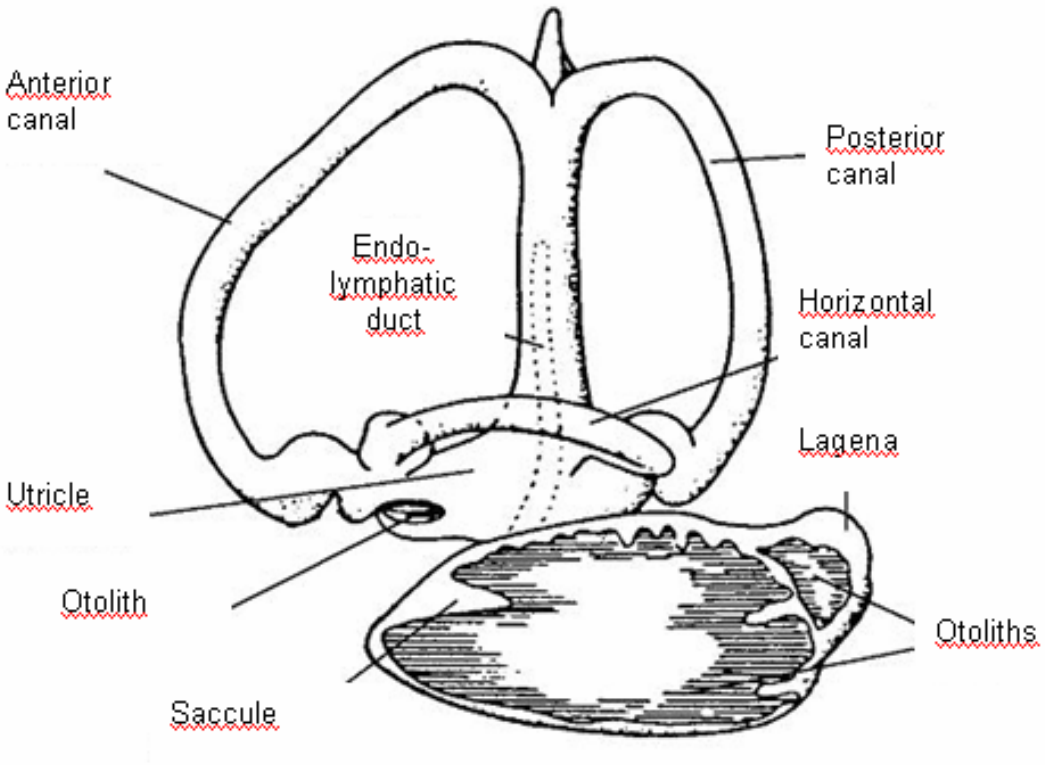

Fig. 2. The frog labyrinth.

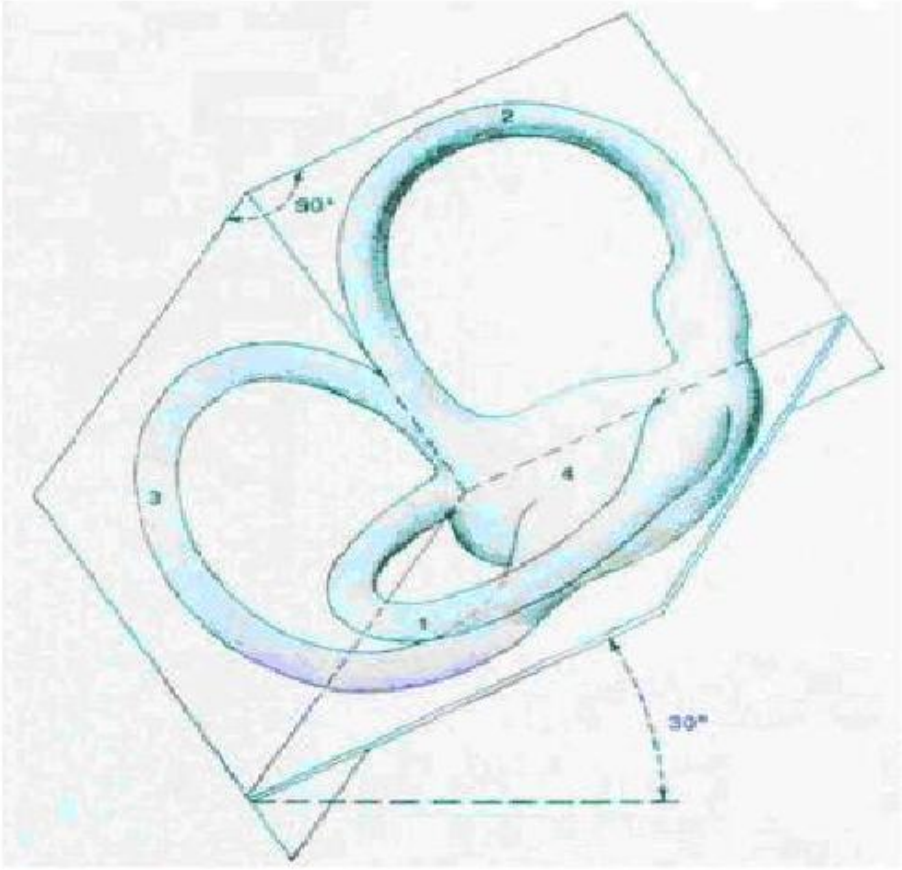

Fig. 3. Tridimensional picture of the labyrinth. The plane of the horizontal canal is rotated by 30° with respect to the horizontal plane.

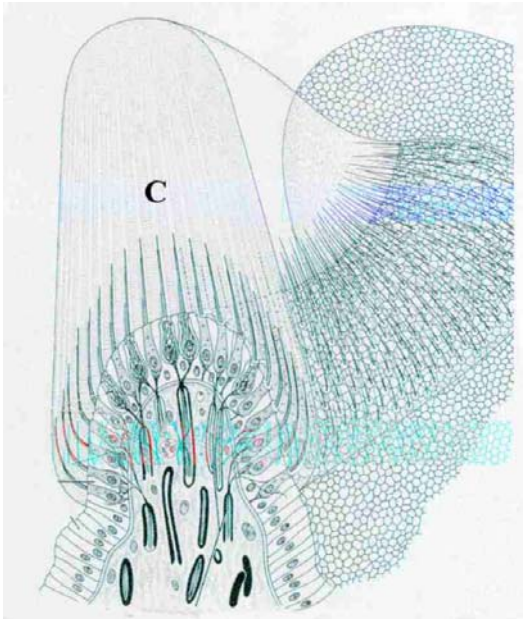

Fig. 4. Hair cells in the crista ampullaris. Note the hair bundles inserted into the cupula (C).

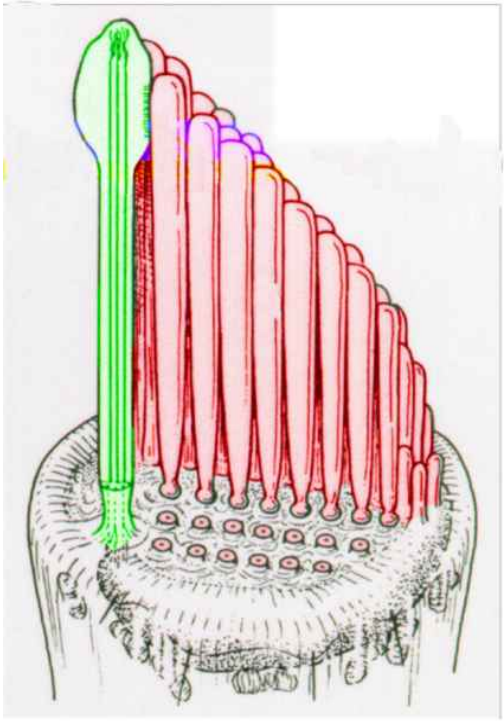

Fig. 5. Kinocilium (green) and stereocilia (red) inserted into the cuticular plate of the hair cell.

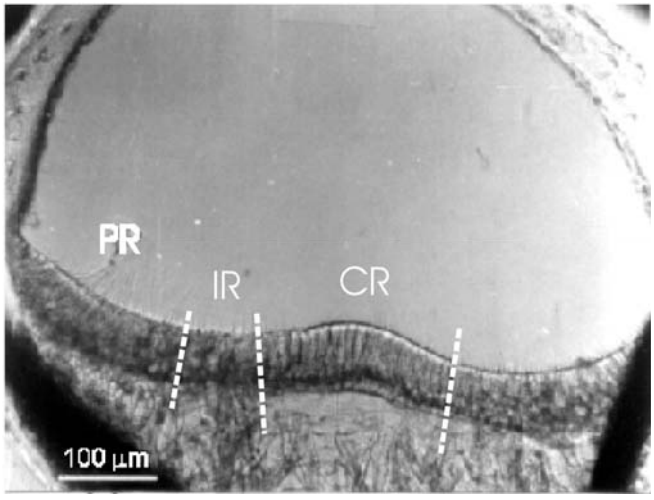

Fig. 6. Frog crista ampullaris from a living preparation. PR, peripheral region; IR, intermediate region; CR, central region.

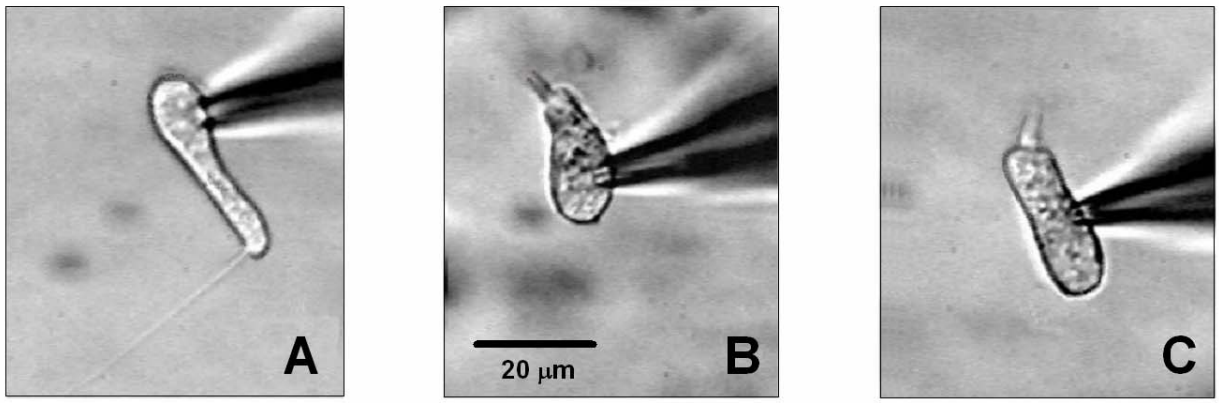

Fig. 7. Video recordings of three different hair cell type: *A*, club-like; *B*, pear-like; *C,* cylinder-like hair cell.

Semicircular canal biophysics

The mechanical events underlying hair cell stimulation have been described by developing a theoretical model called 'torsion pendulum model'. In this model the semicircular canal is assimilated to a circular torus, having a very small internal radius with respect its curvature radius, and containing a fluid (Mammalian Vestibular Physiology, Eds. VJ Wilson and G Melvill Jones, Plenum Press, NY 1979, pages 41-76). According to the model, following head rotation, and consequently canal rotation, the internal fluid is subjected to a movement, relative to its resting position, owing to the combined action of three forces:

- an inertial force, proportional to the canal angular acceleration and to the endolymph inertial moment;
- a friction force proportional to the endolymph viscosity and to canal angular velocity;
- an elastic force, bringing back the cupula, that is proportional to the angular displacement of the cupula itself from its resting position.

The mathematical processing of this model yields to the definition of two time constants: T1 and T2 (with T2 >> T1), whose meaning can be understood by examining the response frequency of the system.

In fact the gain, given as the ratio between the relative displacement of the endolymph and the angular velocity of a sinusoidal stimulus, is constant in a frequency range delimited by the reciprocals of the two time constants (in the frog $1/T_2$ = 0.6 Hz and $1/T_1$ = 60 Hz). In this frequency range the system behaves as a faithful transducer of head velocity. For frequencies ranging from 0 and 0.6 Hz, the system transduces acceleration, and for frequencies larger than 60 Hz, the system is a good transductor of the head position. Since most of the normal head movements occur in the frequency range between 0.6 and 60 Hz, it is reasonable to assume that the sensory response of the semicircular canals is normally interpreted by the central nervous system as a measure of head velocity.

Transduction mechanism

Cupula displacement mechanically deflects the kinocilium and the stereocilia inserted into the cupula. Ciliary deflection represents the stimulus for these mechanoreceptors. The asymmetry of the ciliary bundle is correlated with its directional sensitivity, in fact, ciliary deflection towards the kinocilium increases the probability of opening of the transduction channels located in the cilia and increases receptor potential amplitude

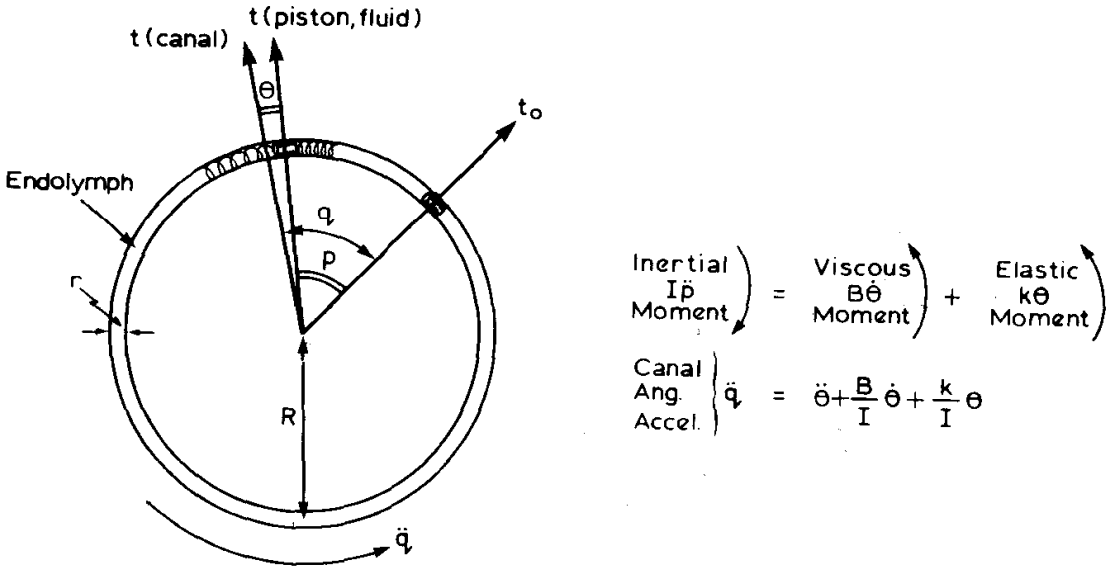

Fig. 8. Schematic drawing of the torsion pendulum model for the semicircular canal: R, radius of curvature; r, semicircular canal internal radius; q and η, endolymph density and viscosity. When the head rotates in a direction with an angular acceleration $\ddot{q}$, the canal remains still, so that the inertia of the endolymph produces a cupula deflection in a direction opposite to that of movement. When acceleration ceases, both the endolymph viscous moment and the cupula elastic moment take back the cupula in its resting position.

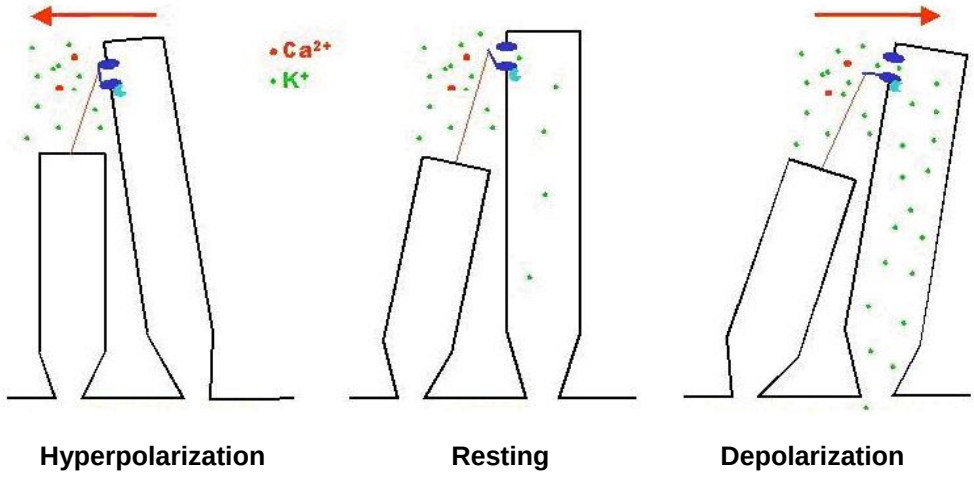

Fig. 9. Ciliary position during inhibition (left), at rest and during excitation (rigth).

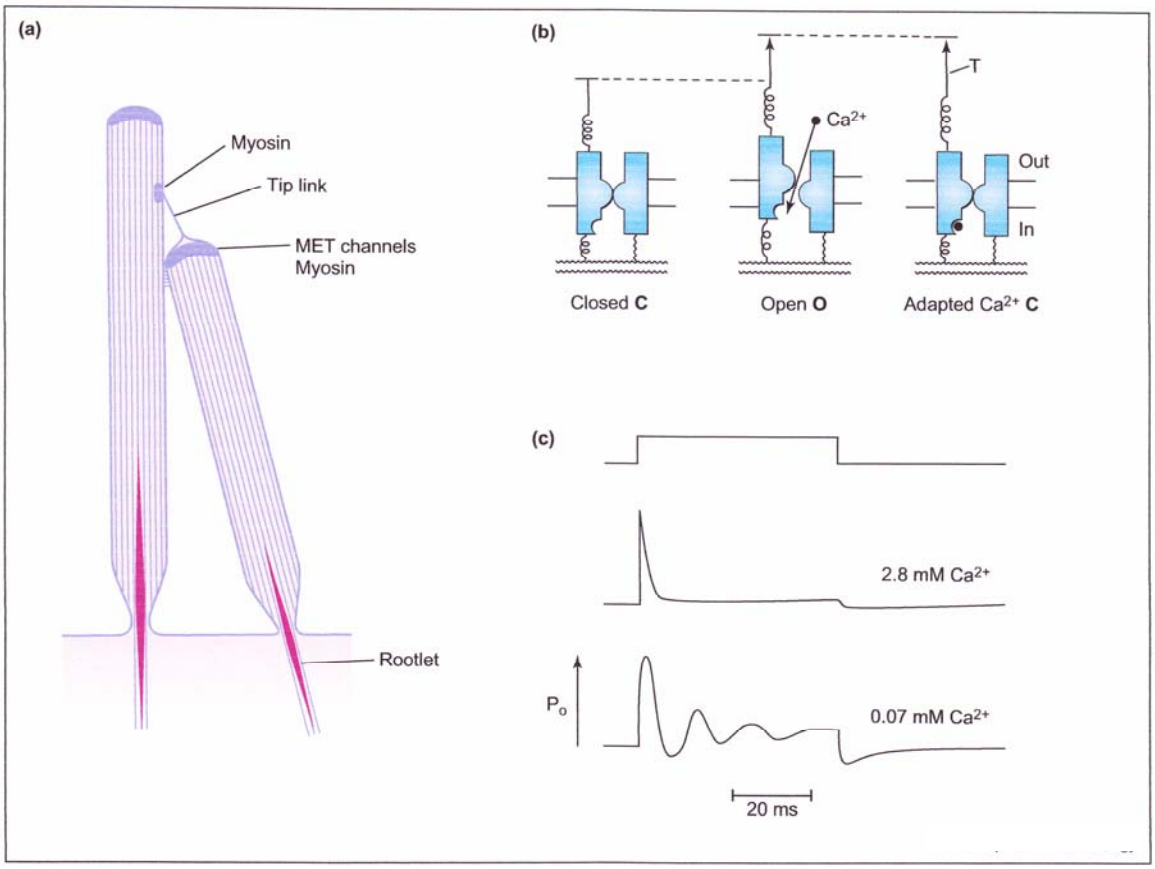

Fig. 10. Sites and action of hair cell adaptation. (**a**) Structural components of the stereocilia associated with transduction and adaptation, showing the electron dense plaques that represent sub-membranous protein complexes. Rotation towards the taller stereocilium exerts force on the tip link and opens MET channels at the stereociliary tip. Tension in the tip link may be adjusted adaptively by myosin arrays (1c, 7a or 15) at either end of the tip link; for example, myosin-1c in the upper plaque tensions the link by climbing up towards the barbed end of the actin filaments. Stereociliary position could also be influenced by the stiffness of the rootlets into the hair cell apex. (**b**) Hair bundle displacement tensions the tip link (T) which extends the internal and external gating springs causing the channel to go from the closed (C) to the open (O) configuration. Ca^{2+} entering the stereocilium through the open channel binds at the inner face of the channel and shuts it. This generates force by increasing tension in the gating springs. (**c**) Following a bundle deflection (top), the channel opens rapidly then recloses adaptively in a high concentration of 2.8 mM Ca^{2+}. Change in Po is plotted against time. When the extracellular Ca^{2+} concentration is reduced to 0.07 mM Ca^{2+}, a more realistic physiological value closer to that in cochlear endolymph, the adaptation becomes oscillatory at 77 Hz. The resonant frequency of the MET channel varies with hair cell CF. This model has been developed for cochlear hair cells (Fettiplace and Ricci, 2003).

The receptor response is maximal when acceleration is applied in the canal plane, while a zero response is obtained if acceleration is applied in a plane orthogonal to the plane of the canal itself.

The opening of the transduction channels allows K^+ inflow, which generates the receptor potential. The current hypothesis for the explanation of the transduction mechanism considers that stereociliary deflection increases the tip link tension that is translated to the mechano-electrical transduction channels through elastic elements that are called 'gating springs'; however, up to now the molecular structure of the transduction channels remains unknown. The probability of opening (P_0) of the transduction channels is modulated by the shift of the ciliary tuft up to a maximum value of 100-200 nm, which is less than the diameter of a stereocilia. To maintain the stereociliary movement in this narrow range of operativity and to preserve their high sensitivity to external stimuli, the transduction channels are subjected to many adaptation mechanisms controlled by Ca^{2+} concentration.

During a maintained displacement of the hair bundle (x), adaptation appears as a decline in the MET channel P_o. This decline reflects a translation of the P_o-x relationship along the displacement axis in the direction of the stimulus. At least two adaptation mechanisms can be distinguished on the basis of their different kinetics and mechanical correlates. Fast adaptation in turtle cochlear hair cells has a time constant (τ_A) of 0.3–5 ms. Slow adaptation, first reported in frog saccular cells, has a τ_A of 10–100 ms. However, both fast and slow mechanisms are now known to coexist in the same hair cell. The different balance of the two components in turtles and frogs may be due to the fact that turtle hair cells, being auditory in function, are exposed to higher stimulation frequencies than frog vestibular hair cells. The speed of adaptation may therefore be matched to the frequencies to which the cell is exposed. Consistent with this idea, fast adaptation is most conspicuous in mammalian cochlear hair cells with a $\tau_A = 4$ ms. Moreover, τ_A in the turtle varies with hair cell characteristic frequency (CF), and is faster in the cells tuned to higher frequencies: the corner frequency ($1/2\pi\tau_A$) of the high-pass filter imposed by fast adaptation is approximately two-thirds of the CF. This suggests that fast adaptation may play some role in hair cell frequency selectivity (the ability of the cell to distinguish different frequency components in the stimulus). Further support to this notion arises from the observation that, in physiological Ca^{2+} concentration, fast

adaptation can display resonance at frequencies in the turtle's auditory range.

Both types of adaptation are regulated by Ca^{2+} that enters the stereocilia through highly Ca^{2+}-permeable MET channels. Fast adaptation probably requires a direct interaction of Ca^{2+} with the MET channels to modulate their probability of opening. On the basis of the effects of intracellular calcium buffers, the distance Ca^{2+} diffuses to its target is estimated to be short, 15–35 nm from the mouth of the channel. Its resulting action occurs in less than a millisecond. Furthermore, Ca^{2+} can alter the time constant of channel activation as well as adaptation, arguing that it is intimately linked with channel gating. In contrast, slow adaptation is considered as an input control, in which a Ca^{2+}–dependent motor controls tension in the elastic elements in series with the channel. There is good evidence to implicate myosin-1c as the motor that drives slow adaptation in vestibular hair cells. One or both phases of adaptation could be mediated through an interaction with calmodulin, which is present at the tips of the stereocilia where it interacts with myosin-1c. Besides the two Ca^{2+}-driven mechanisms, other pathways may modulate the MET channel's operating range. For example, cyclic adenosine monophosphate (cAMP) shifts the P_o-x relation along the displacement axis in the positive direction, with no affect on fast adaptation. The cAMP effect may be mediated through phosphorylation of the MET channel or the myosin motor by protein kinase A.

A prediction of the gating spring model of transduction is that as the channel opens there is a decrease in hair bundle stiffness, and this is confirmed experimentally. Ca^{2+} interaction with the channel to modulate its P_o will therefore cause the bundle to move, connecting fast adaptation to bundle motion. In terms of polarity, a positive bundle deflection opens the MET channels and increases Ca^{2+} concentration, which recloses the channels and causes negative recoil. In contrast, the increase in Ca^{2+} produced by a positive bundle deflection detaches the myosin from the actin core of the stereocilium. This allows the myosin and its attachment to the tip link to slip down the stereocilium, which leads to further positive displacement of the bundle. Evidence for the range of movement of the tip-link's upper attachment point comes from the observation that if the tip links are severed with BAPTA (1,2-*bis*[o-Aminophenoxy]ethane-N,N,N',N'-tetraacetic acid), the electron dense plaque climbs 50–100 nm closer to the stereociliary tip

A reason for endowing multiple adaptation mechanisms is that the slower mechanism has a wider dynamic range to orient the bundle to a location where fast feedback control of the channels is effective. Thus, fast adaptation may tune the channel for small displacements around a resting position that is continually readjusted by slow adaptation.

Fast adaptation could theoretically participate in auditory frequency selectivity by filtering the MET current or by generating fast hair bundle movements that amplify the mechanical input. Hair bundles in the frog saccule exhibit the ability to mechanically amplify a signal leading to spontaneous oscillations. The oscillations occur at low frequencies (5–50 Hz) and it has been hypothesized that they are driven by the slow myosin motor, biasing the displacement-force relation of the hair bundle into a region of negative slope. In contrast, active bundle movements produced by Ca^{2+} binding to the MET channels can in principle occur at kHz frequencies, within the mammalian auditory range. Furthermore, trans-epithelial electrical stimulation of the isolated frog saccule experimentally evokes hair bundle oscillations at frequencies of up to 1 kHz. There is also *in vivo* evidence for active hair bundle motion at more than 1 kHz in the lizard hearing organ. However, it remains to be verified whether or not active motion of the outer hair-cell bundles can generate sufficient force to produce amplification in the intact mammalian cochlea. Tuning of the MET current in turtle auditory hair cells does not require concomitant active bundle motion because it occurs when the bundle is displaced with a rigid stimulating probe. This suggests that the energy associated with channel gating does not need to move the hair bundle in order to elicit oscillations in the current. The variation in resonant frequency (58–230 Hz), which is within the turtle's auditory range, may therefore involve differences in the MET channel. Several mechanisms for these differences have been proposed. The adaptation rate or resonant frequency increases with a higher stereociliary Ca^{2+} concentration, which could be brought about either by increasing the channel's Ca^{2+} permeability with CF or by increasing the conductance of the MET channels or their number per stereocilium. The evidence for this mechanism is that the maximum MET current increases with CF, and the rate of adaptation at a given CF varies with the magnitude of the current. It has been recently shown that the channel's Ca^{2+} permeability does not change with CF. However, there is evidence for a tonotopic variation in channel kinetics derived from noise analysis of the MET current and from measurements of the time course of current activation. An alternative view of modeling hair bundle amplification, is that both fast and slow adaptation processes combine to produce oscillations at a frequency determined by hair bundle geometry and intracellular Ca^{2+} dynamics. In the mammalian cochlea, the outer hair cells (OHC) are responsible for generating active mechanical amplification that provides the compressive non-linearity and frequency selectivity of the basilar membrane. The ability of OHCs to elongate and shorten in response to changes in membrane potential is thought to supply the mechanical energy for the process.

Prestin has been identified as the protein responsible for this 'somatic motility', concentrated in the lateral wall of the OHC. The voltage sensitivity of prestin is endowed by the intracellular binding of small anions such as Cl^-. Targeted deletion of prestin in mice results in an elevated threshold, reduced tuning, and loss of outer hair cell motility; these effects led to conclude that somatic motility alone was responsible for the active process. This conclusion can be criticized on the ground that any feedback process involving multiple elements would be compromised if one element were eliminated. For example, abolition of the endocochlear potential (EP) by treatment with the diuretic furosemide reduces amplification about 30-fold on average, even though the EP is not the source of the active process. Loss of the EP will approximately halve the MET current. Based on the same argument, halving of electromotility in prestin heterozygotes should have produced greater than the twofold elevation in cochlear threshold if somatic motility were the sole source of the active process. Furthermore, although OHC motility may supply the energy for amplification, there is no evidence that it is intrinsically frequency-selective. For cochlear models that reproduce realistically sharp tuning of the basilar membrane, the mechanical feedback from the outer hair cells must occur in a frequency-selective manner to ensure that it will supply force at the appropriate phase of basilar membrane vibration. The required tuning has been ascribed to a mechanical resonance in the tectorial membrane, but it could equally reside in the MET channels. If the channels in mammalian OHCs operate similarly to those in turtle hair cells, the transducer currents and any associated active hair bundle motion will be tuned over a frequency range governed by variations in the speed of fast adaptation. In the past years, evidence has emerged for the existence of at least two distinct Ca^{2+}-mediated mechanisms of hair cell transducer adaptation, which change in speed, range and function. A fast mechanism directly affects MET channel gating, whereas a slower one regulates the mechanical stimulus through the action of one or more unconventional myosins. Further insights into the roles of the different myosins may come from the elucidation of their subcellular localization using post-embedding immunogold techniques, or their modification and deletion in transgenic animals. The fast mechanism confers tuning on the MET channels and may be an important factor in cochlear frequency selectivity. Because adaptation shifts the hair cell's operating point, it may have an ancillary role in constantly adjusting and optimizing the signal-to-noise ratio of transduction. Cloning the MET channel should shed light as to how the channel interacts with Ca^{2+} and other subcellular components including myosins. It may also reveal the existence of multiple channel isoforms with Ca^{2+} affinity or kinetics specialized for operating in different frequency ranges.

Moreover, further electrophysiological studies in the mammalian cochlea will be needed to settle whether or not fast adaptation is present in outer hair cells and whether or not it is sufficiently fast to participate in the active processes. Evidence that this may be the case was recently obtained in rat OHCs, in which transducer currents exhibited fast Ca^{2+}-dependent adaptation with a τ_A of less than 0.2 ms, faster than any seen in turtle auditory hair cells.

The hair cell ionic currents

The calcium current

Ca^{2+} inflow through basolateral, voltage-gated Ca^{2+} channels of vestibular hair cells plays a crucial role in signal processing because it sustains transmitter release at the cytoneural junction and regulates membrane excitability (Martini et al., 2000).

The inward current was assessed by stepping the voltage to -20 mV. The current amplitude and waveform did not change if the voltage was stepped from any holding value between -140 and -60 mV: this indicates that, at any voltage below -60 mV, all channels were deactivated and steady-state inactivation was removed. The Ca^{2+} current had two typical waveforms: one (present in ~ 40% of the cells) was characterized by an initial peak, followed by an exponential decay to a plateau level (current sag component); the other waveform lacked the sag, and the current amplitude was constant throughout the depolarizing step. The sag might have been generated by the opening and the subsequent partial inactivation of a single channel population: however, this view does not explain the absence of the sag in some recordings, nor does it explain the lack of correlation between the sag properties (amplitude and time course) and steady-state current amplitude.

The presence of either of the responses was not correlated with the cell morphology and those cells exhibiting a sag response eventually ended in a plateau-response. Indeed, the mean current amplitude was not stable upon repeating the stimulation protocol (consisting of 20 depolarizing steps, from the holding potential to -70 mV, lasting 40 ms and repeated every 15 s), but it progressively declined to zero (run-down).

The sag component of the current (when present) was lost much earlier than the plateau component. Once the former component had completely disappeared, the latter began a progressive decline towards zero.

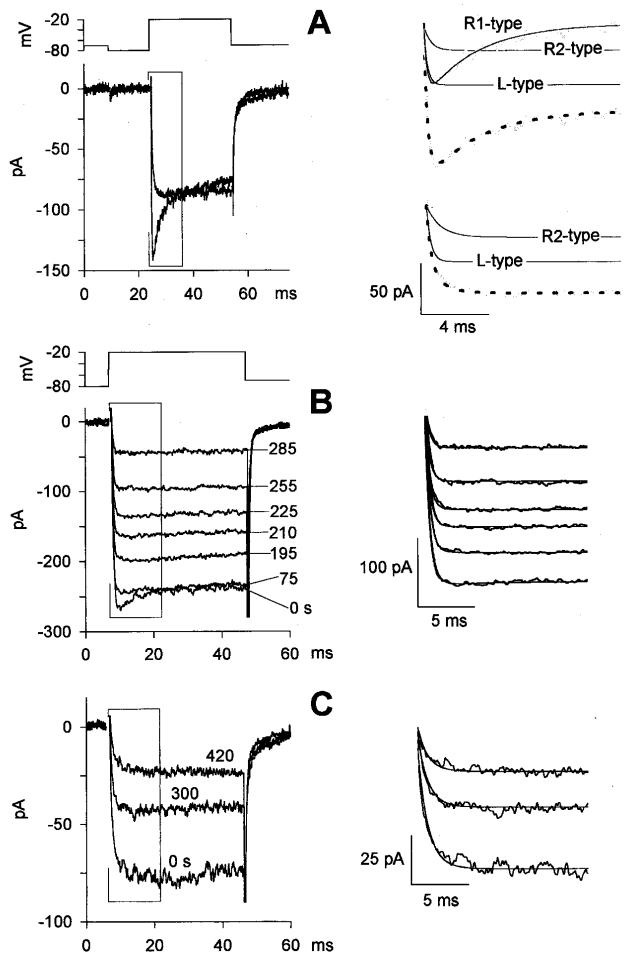

Fig. 11. Ca^{2+} current waveforms and typical rundown experiments. **A**, After measuring the leak resistance with a 15-ms hyperpolarization to -80 mV from the holding potential (-70 mV), the $Ca^{2\pm}$ current was elicited by a 30-ms depolarization to -20 mV. *Left,* typical Ca^{2+} current waveform recorded from two cells, one displaying and the other lacking the sag component. *Right,* activation and inactivation kinetics of the responses. Tracings on the left are fitted by Eq. 1 *(dotted traces).* The *solid thin traces* are the contribution of the two R-type and the L-type currents to the total current. The *RI -type* trace was constructed by fitting the sag component, which was singled out *(gray trace)*, as discussed in the text. *(***B***)* Ca^{2+} current run-down in response to repetitive 40-ms depolarizations to -20 mV from a potential of -80 mV, repeated every 15 s; representative traces are shown at seven recording times (indicated in s near each trace). *(***C***)* Ca^{2+} current run-down in response to the same depolarizing test pulses delivered at the indicated times (in s above each trace). Representative traces from *B* and *C* are fitted by Eq. 1, as shown on the right.

The sag response can be readily explained by assuming that depolarization opened at least two channel types generating two different calcium currents, both rising exponentially with a common time constant of 0.5 ms: the first exhibiting an inactivating time constant of a few ms, while the second did not inactivate.

The sag response was generated by a Ca^{2+} channel exhibiting a Ca^{2+}-dependent inactivation. The sag and the plateau amplitudes were reduced, and the sag kinetics slowed down, with a decrease in $[Ca^{2+}]_o$; the sag disappeared when Ca^{2+} was substituted with Ba^{2+}. Consistent with the notion that the Ca^{2+}-dependent inactivation is removed in Ba^{2+}, the current increase observed upon substituting Ca^{2+} with Ba^{2+} was smaller in those cells that lacked the sag component than in those where the sag was present. The effects of both $[Ca^{2+}]_o$ reduction and Ba^{2+} substitution were fully reversible upon returning to normal $[Ca^{2+}]_o$. To determine whether the Ca^{2+}-dependent inactivation was also voltage-dependent, recovery from inactivation was investigated using the standard two-pulse protocol. Two depolarizing steps to -20 mV were separated by progressively longer interpulses at two different holding potentials (-70 mV and -120 mV). The time interval between each one of the consecutive double-pulse protocols was 7 s, which allowed full recovery of the test current. Analysis of the fractional amplitude versus interpulse duration indicated that recovery from inactivation required times on the order of 100 ms at -120 mV and 300 ms at -70 mV. Such long recovery time is not consistent with the presence of a voltage-sensitive inactivating gate, which should act much faster; it is, however, compatible with the speed at which $[Ca^{2+}]_i$ is restored to its physiological levels upon returning to the holding potential. In order to better identify the channel types generating the compound Ca^{2+} current waveform, typical Ca^{2+} antagonists were used. It was found that 1 μM nifedipine reduced the current plateau fraction (leaving the sag component, when present, unaffected) by 57.1 ± 3.6% (n = 5), thus indicating the presence of an L-type channel. Since 5μM nifedipine reduced the plateau component by 68.4 6 ± 2.0% (n = 12), and 10 μM nifedipine produced nearly the same current reduction (again, either concentration did not affect the sag component), it can be concluded that ~70% of the plateau component was carried by an L-type channel. Nifedipine (5 μM) had nearly the same effect on the Ba^{2+} current amplitude (a mean decrease by 62.2 ± 6.3%; (n= 5) in those cells showing no sag component in the presence of external Ca^{2+}.

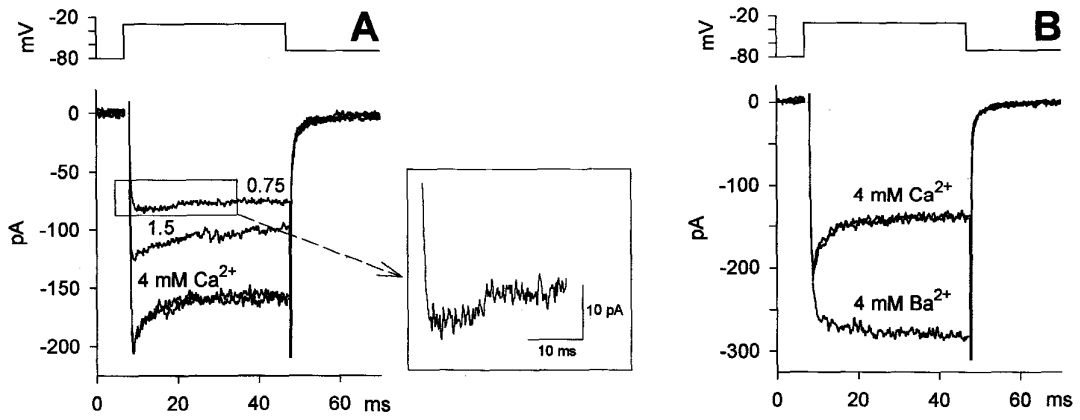

Fig. 12. Ca^{2+}-dependent inactivation of Ca^{2+} current. Voltage was stepped to -30 mV to maximize the sag component. **A**, Effect of $[Ca^{2+}]_o$ reduction (from 4 mM to 1.5 or 0.75 mM) on the Ca^{2+} current. *Inset:* enlargement of the current trace recorded in 0.75 mM Ca^{2+}, as indicated in the box. **B**, Absence of inactivation when Ca^{2+} is replaced by an equiosmolar concentration of Ba^{2+}. In *A* and *B* the two superimposed traces are the control and recovery in 4 mM $[Ca^{2+}]_o$, before and after the perfusion with 1.5 and 0.75 mM $[Ca^{2+}]_o$ (*A*), or 4 mM $[Ba^{2+}]_o$, (*B*).

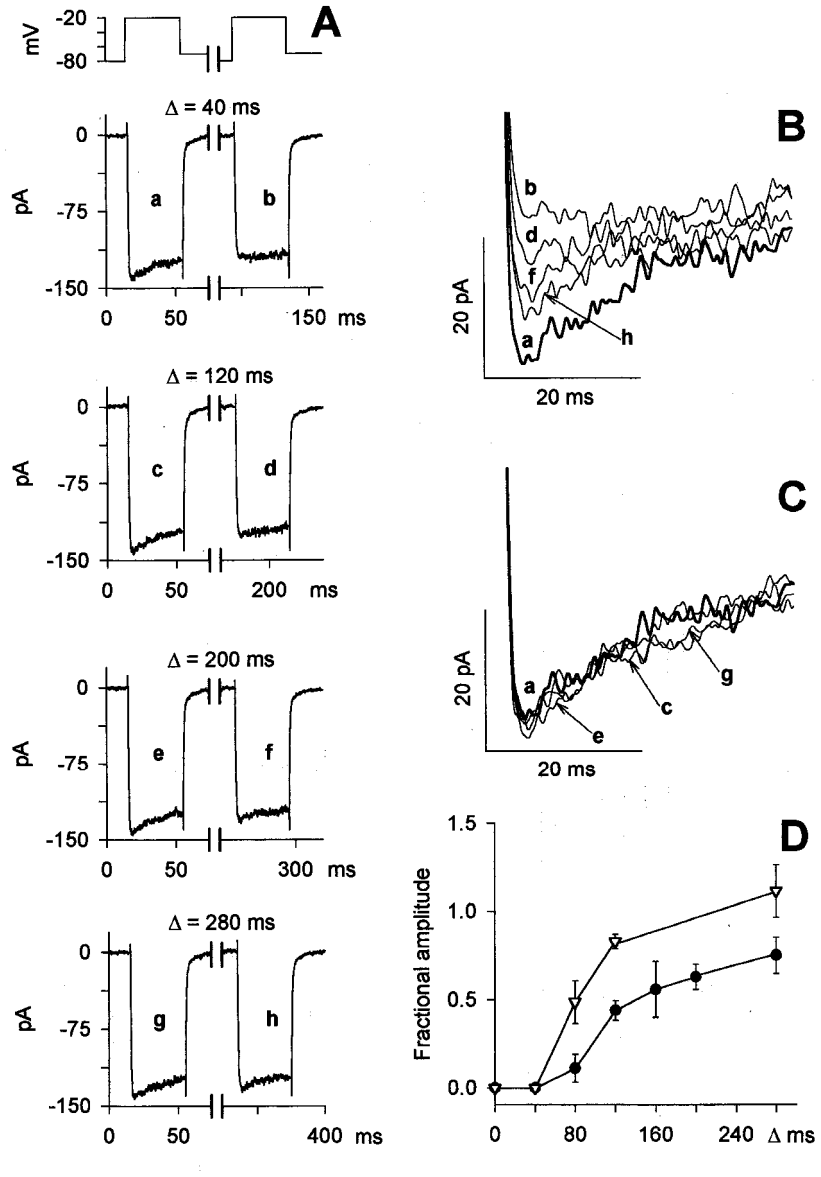

Fig. 13. Kinetics of current recovery from inactivation. **A**, After measuring the leak resistance, two consecutive 40-ms depolarizations to -20 mV were delivered, separated by 20, 100, 180, and 260 ms interpulses to -70 mV (interpulse holding potential). All interpulses were followed by an additional 20-ms step to -80 mV to re-evaluate leak resistance before delivering the second pulse (the time Δ is the interpulse duration). The time interval between each of the consecutive double depolarization protocols was 7 s. The Ca^{2+} currents elicited by the first depolarization (*A*, *traces a, c,* e, and *g),* and by the test depolarization (*A*, *traces b, d, f,* and *h)* are compared in **C** and **B**, respectively, on a faster time scale; the lowercase letters indicate the same traces in **A**, **B**, and **C**. **D**, Mean values of the ratio between the peak Ca^{2+} current elicited by the test depolarization and the peak Ca^{2+} current elicited by the prepulse. Interpulse holding potentials were -70 mV *(filled circles,* 8 cells) and -120 mV *(open triangles,* 8 cells)

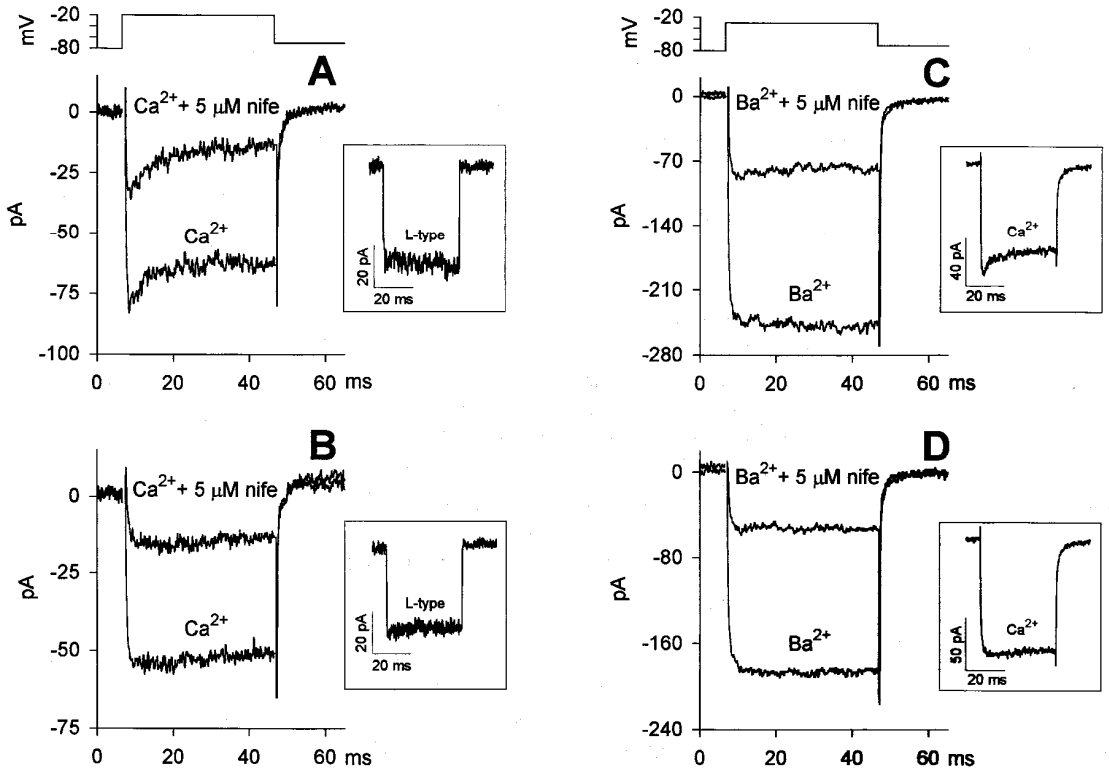

Fig. 14. Effect of nifedipine on the Ca^{2+} and Ba^{2+} currents (in 4 different cells). The recovery following each nifedipine application was complete and was omitted for clarity. Effect of nifedipine on the Ca^{2+} current in the presence, **A**, and in the absence, **B**, of the sag component; the L-type current resulting from the difference between the two traces on the left in *A* and *B* is shown in the corresponding *inset* on the right, **C**. Effect of nifedipine on the Ba^{2+} current in a cell presenting the sag component in Ca^{2+} *(inset* on the right) and in **D** in a cell exhibiting only the plateau component in Ca^{2+} (inset on the right).

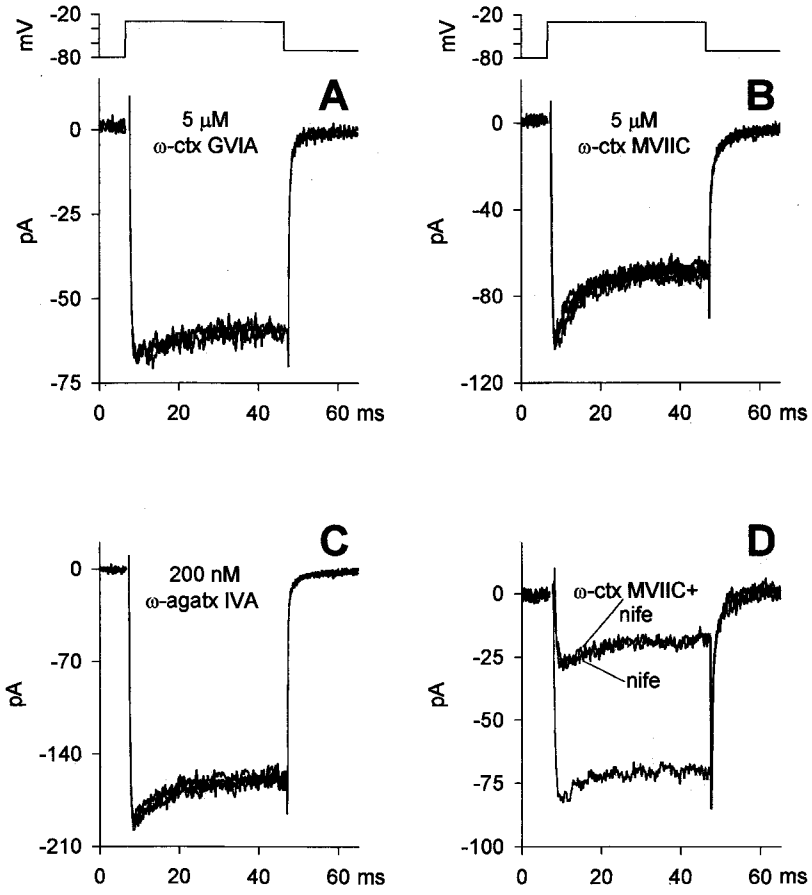

Fig. 15. Effect of ω-conotoxin GVIA, ω-conotoxin MVIIC, and ω-agatoxin IVA on the peak and the plateau component of the Ca^{2+} current in three representative cells. **A-C**, The responses to at least three subsequent depolarizing test pulses to -30 mV in the presence of the antagonist (indicated above each trace family) are compared with the control traces recorded before and after antagonist application. The effect of ω-conotoxin MVIIC during the nifedipine application is shown in **D** in a fourth cell.

The total current was unaffected by ω-conotoxin GVIA (5 µM, 7 cells), ω-conotoxin MVIIC (5 µM; 5 cells), and ω-agatoxin IVA (up to 0.4 µM; 5 cells), thus ruling out the presence of N- or P/Q-type Ca^{2+} channels. These compounds, as expected, did not affect the nifedipine-resistant current (5 µM nifedipine; 4 cells), indicating that this current was flowing through R-type channel component (Fig. 15).

When present, the sag component remained unaffected by the application of nifedipine, thus indicating that the sag was generated by the inactivation of the R-type current and not by a partial inactivation of the L-type. The progressive loss of the sag component during the initial phase of rundown occurred without any change in the plateau amplitude. This fact cannot be accounted for by the progressive loss of a Ca^{2+}-dependent, partial inactivation of a single R-type channel. Instead, it could be explained by the presence of a third channel type, which runs down completely before the onset of the plateau component reduction. This channel could be a T-type channel: however, no T-type channel has been reported to lose inactivation in Ba^{2+}. Thus, it can be concluded that two R-type channels generate the current left after the nifedipine application: one generates the sag and fully inactivates in a Ca^{2+}-dependent manner, the other does not inactivate and accounts for the remaining plateau. Cd^{2+} and Ni^{2+} were able to block the inactivating R-type channel; however, high concentrations of these cations were able to suppress the total current consistently with the almost complete suppression of the Ba^{2+} current induced by 100 μM Cd^{2+}.

In conclusion, the activation-inactivation phase $I_a(t)$ of the Ca^{2+} current waveform can be reasonably described by the following equation (Eq. 1):

$$I_a(t) = A_L \bullet (1 - e^{-(t/\tau R1)} + A_{R1} \bullet e^{-(t/\tau iR1)} \bullet (1 - e^{-(t/\tau aR1)}) + A_{R2} \bullet (1 - e^{-t/\tau aR2})$$

where A_L and τ_{aL} are the amplitude and the activation time constant of the L-type current; A_{R1}, τ_{aR1}, and τi_{R1} are the amplitude, activation, and inactivation time constants of the transient R-type current; A_{R2} and τ_{aR2} are the activation parameters of the plateau R-type current. The responses consisting of only the steady-state component were interpolated by Eq. 1 with $A_{R1} = 0$. The average amplitude of the plateau component, that is $AL + A_{R2}$, was -126 ± 6 8 pA (n= 53 cells); the absolute values of A_L and A_{R2} can be estimated from the relationship $A_L \sim 2.3 \times A_{R2}$, drawn from the nifedipine experiments. The A_{R1}, τ_{R1}, and τi_{R1} values were obtained upon fitting the sole experimental sag component. The sag was singled out by subtracting the current recorded after the full run-down of the sag from the total current recorded at the beginning of an experiment. The results of this procedure were τi_{R1} = 6.7 ± 0.8 ms (n = 22); A_{R1} = -42 ± 5 pA; τ_{R1} = 0.18 ± 0.03 ms (n = 10). The difference between the total current and the current recorded in nifedipine gave the waveform of the L-type current; τ_{aL}, assessed by fitting the rising phase of the latter current, was 0.35 ± 0.06 ms (n = 6). The time constant τ_{aR2},

drawn from the fit of the currents lacking the sag component in the presence of nifedipine was 0.68 ± 0.08 ms (n = 6). The above described procedure is presumably correct to calculate τ_{aL} and τ_{aR2}, providing that nifedipine does not affect τ_{aR2}. This condition is indeed satisfied here since, in all experiments, no significant difference was found between the values of τ_{aR2} obtained in 1 μM and in 5 μM nifedipine. The responses with or without the sag component had almost identical deactivation kinetics upon returning to the holding potential; in general, it was not possible to record the inward peak tail currents, probably because they were too fast to be resolved by our experimental arrangement. Thus, the deactivation phase $I_d(t)$ of the Ca^{2+} current can only be interpolated by:

$$I_d(t) = A_{dL} \bullet e^{(-t/\tau dL)} + A_{dR2} \bullet e^{(-t/\tau dR2)}$$

The parameters A_{dL} and τ_{dL} are the amplitude and time constant of the deactivation phase of the L-type current: the fit to these currents gave $A_{dL} = A_{aL}$ and τ_{dL} = 0.24 ± 0.05 ms (n = 6). The deactivation phase of the non-inactivating R-type current was calculated by the fit of the current in nifedipine. The resulting values were τ_{dR2} = 8.5 ± 0.6 ms (n = 20) and A_{dR2} = -18.0 ± 2.0 pA (n = 29 cells). To further characterize the three channel types it is necessary to determine their voltage dependence. Given the long recovery time from inactivation, the interpulse duration of the I-V protocols was kept longer than 1 s. Fig. 16 shows the voltage dependence of the Ca^{2+} current waveform in a typical cell. A peak superimposed on the plateau became appreciable at -40 mV (which is the activation threshold of the R-type channel generating the sag waveform), reaching a maximal value at -30 mV. The peak was progressively reduced by larger depolarizations, and became undetectable for voltages ≥0 mV. The plateau component, generated by the non-inactivating R-type channel and the L-type channel, was appreciable at -60 mV, peaked at -20 mV, and had a reversal potential of about +50 mV. The I-V relationships for the peak and plateau components are illustrated in panel *B* (open diamonds and filled circles, respectively). The normalized average I-V of the peak (open diamonds) and plateau (filled circles) components are shown in Fig.17; since no significant changes were found in the I-V relationships recorded using different pipette $[Ca^{2+}]$, the data for these I-V relationships were averaged together. The I-V of the plateau component exhibited a Vrev of +40 mV (Fig. 17 *A*, filled circles), smaller than would be expected from the Nernstian reversal potential for Ca^{2+} (>200 mV).

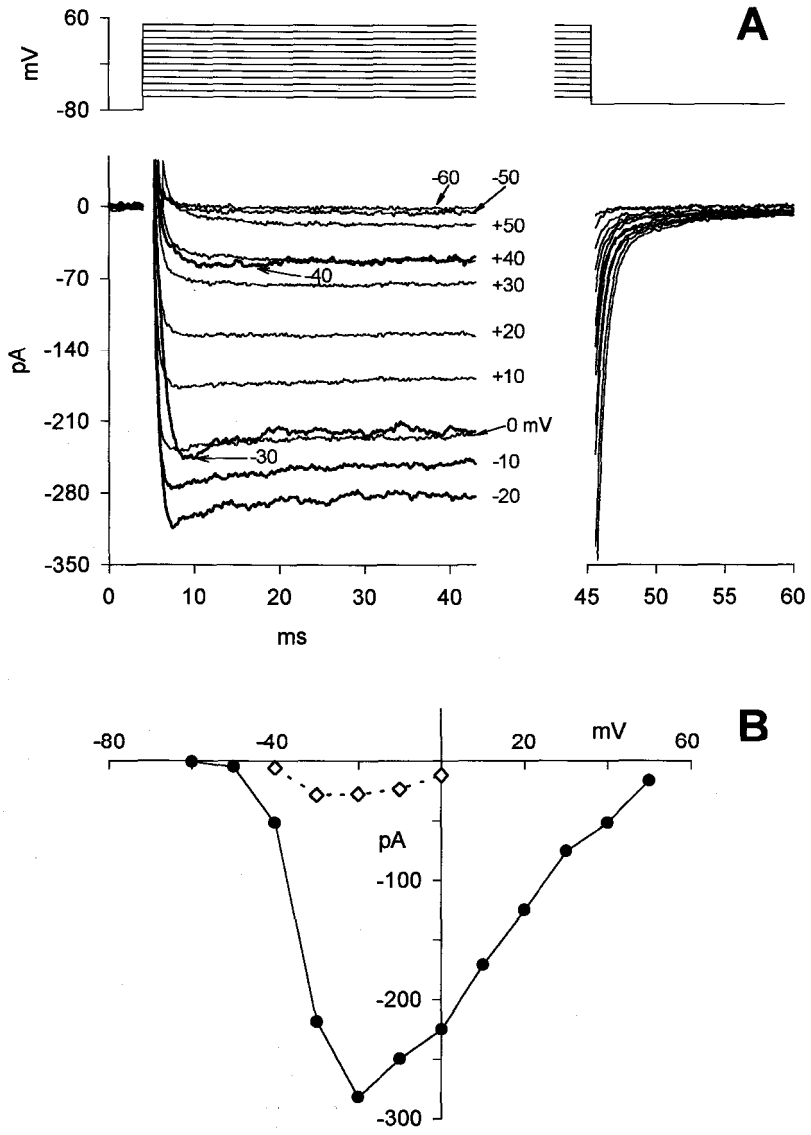

Fig. 16. I-V characteristics of the current exhibiting the sag. **A**, *left panel* Ca^{2+} currents were elicited by depolarizing voltage pulses from -60 mV to +50 mV in l0-mV increments, from a potential of -80 mV; *right panel,* deactivation kinetics upon returning to the holding potential (-70 mV). **B**, Steady state *(filled circles)* and peak *(open diamonds)* current amplitudes from each trace of the cell shown in *A* are plotted against the test potential.

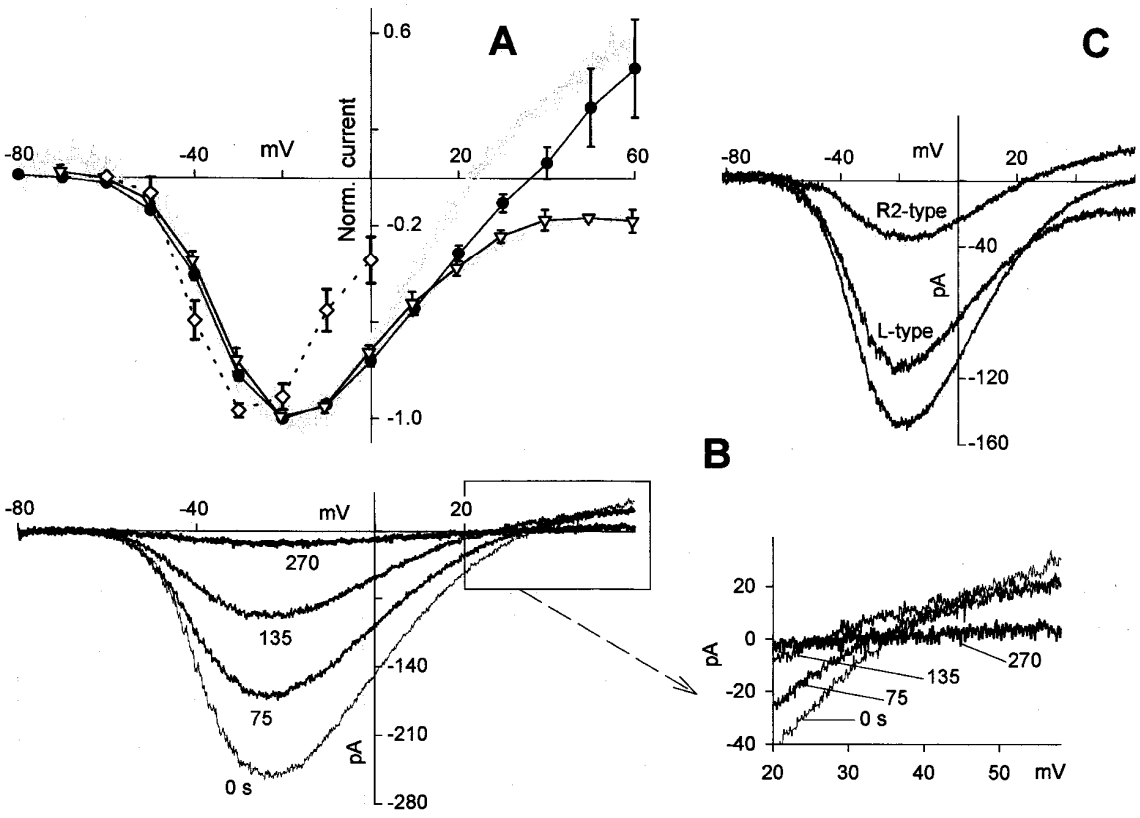

Fig. 17. Voltage dependence of the R-type and the L-type currents. Ca^{2+} currents in the presence of intracellular Cs^+ or NMG^+ (90 mM). **A**, Normalized I-V values of the average sag component in Cs^+ (i.e., the inactivating R-type current scaled to the maximal value of A_{RI}, attained at -30 mV, *open diamonds,* 15 cells); the average plateau component in Cs^+ (scaled to the maximal value of the plateau current, attained at -20 mV, *filled circles,* 15 cells) and in NMG^+ *(open triangles,* 7 cells); the R2-type component *(gray noisy trace)* and the L-type component *(gray noisy trace* matching the *open triangles)* of the cell in *C.* In NMG^+, voltages are corrected for the junction potential with respect to Cs^+ (+9 mV). **B**, I-V relationships in Cs^+, elicited during run-down by voltage ramps of steepness 0.63 mV/ms, from -80 mV to +60 mV, repeated every 15 s. These representative traces were recorded at the beginning of the experiment (0 ms, *thin trace)* and at three subsequent times (75, 135, and 270 s; *thicker traces)*; the current responses to the ramp for a voltage interval between +20 and +60 mV *(box)* are enlarged on the right. **C**, I-V relationships of a cell exhibiting a small V_{rev}, in response to a ramp of voltage (0.56 mV/ms): I-V of the total current *(unmarked trace),* of the current in the presence of nifedipine *(R2-type trace)* and of the current resulting from the difference between the two latter currents *(L-type trace).* (Vrev) of ~ +50 mV. The I-V relationships for the peak and plateau components are illustrated in panel *B* (open diamonds and filled circles, respectively).

However, the current never reversed for depolarizations up to +60 mV when $[Cs^+]_i$ was substituted with an equiosmolar concentration of the large impermeant cation NMG^+ (Fig. 17 *A*, open triangles). Furthermore, as shown in Fig. 17 *B*, the size of the outward current was progressively reduced as the Ca^{2+} current declined during the run-down indicating that most of the Cs^+ current flowed through the Ca^{2+} channel itself. The I-V relationships of the two channels generating the plateau component were isolated using a voltage ramp of appropriate steepness (0.56 mV/ms), so that the R-type channel generating the peak was inactivated and did not contaminate the plateau amplitude. The I-V relationship of the noninactivating R-type channel (R2) was obtained in the presence of 5 μM nifedipine; subtracting the R2-type channel I-V from the total current I-V (i.e., the current recorded in the absence of nifedipine), gave the I-V of the L-type current (Fig. 17 *C*). Interestingly, when normalized to the same maximal current amplitude (which was attained at +20 mV for both currents; Fig. 17 *A*), the R2-type and the L-type channel I-V values were indistinguishable up to ~0 mV; above this voltage, the L-type current I-V was always below that of the R2-type. In fact, at more depolarized voltages, the latter channel carried all the outward current. Accordingly, the normalized L-type current could not be distinguished from the normalized average I-V relationship recorded when the internal Cs^+ was substituted with NMG^+ (Fig. 17 *A*).

The run-down occurred in all cells after several minutes of whole-cell recording and was accelerated by the duration of channel activation, as illustrated in the experiment of Fig. 11 *C*, where the Ca^{2+} current was probed a few times over a long recording. Indeed, the run-down ensued later than it did during stimulation at higher frequency (Fig. 11 *B*). It has been shown that the run-down of L-type cardiac Ca^{2+} currents can be prevented by calpastatin, an inhibitor of the cytoplasmic Ca^{2+}-dependent proteases. To verify whether a similar mechanism operates in semicircular canal hair cells, 2 U/ml of calpastatin were incorporated into the pipette solution. Calpastatin completely prevented the run-down, even in cells where the initial response was not particularly large, and despite the heavily sustained and repetitive activation of the current. Indeed, the size and waveform of the current families illustrated in Fig. 18 remained virtually unchanged, although the cell was stimulated with three sequences of 20 depolarizing steps, delivered at 15-s intervals, and lasting 40 ms (*B* and *D*) or 280 ms (*C*; the whole-cell recording time was ~20 min).

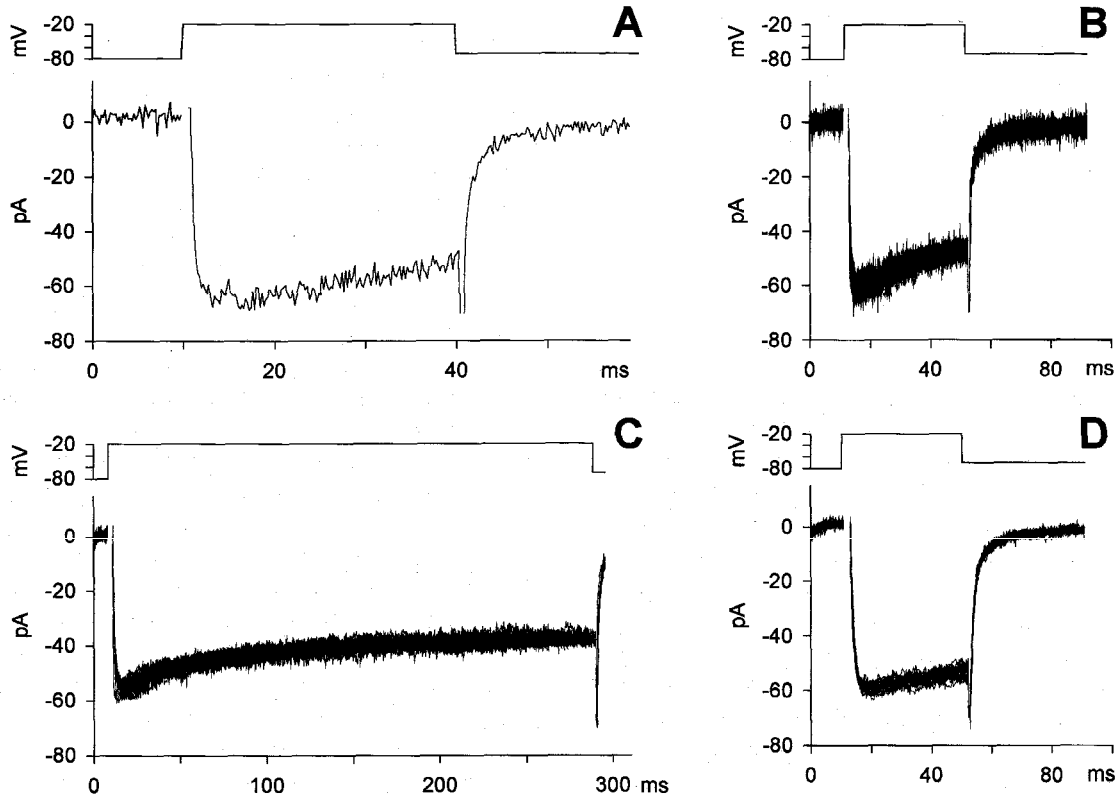

Fig. 18. Effect of intracellular perfusion of 2 U/ml calpastatin on the current amplitude and waveform. **A**, Typical Ca^{2+} current elicited by a depolarization to -20 mV from a potential of -80 mV. **B-D**, Responses of the same cell to a sequence of 60 depolarizing voltage pulses delivered every 15 s and lasting 40, 280, and 40 ms, respectively.

Surprisingly, in some cells the amplitude of the plateau component progressively increased upon repeating the depolarizing step (before the onset of the run-down; Fig. 19), even doubling in size when compared to the beginning of the recording. This phenomenon has been described in other systems and it is commonly referred to as current "run-up." The run-up observed here cannot be ascribed to the facilitation sustained by a kinase-induced phosphorylation of a site exposed by channel opening. Indeed, a 300-ms conditioning depolarization to +40 mV failed to induce any increase in either peak or steady-state amplitude of the current elicited by a test depolarization to +20 mV. The run-up of the plateau component was never accompanied by run-up of the sag component: this means that the inactivating R-type channel did not manifest run-up, but only run-down. Furthermore, the run-down kinetics of the latter channel was always independent of the run-up. To determine whether the run-up of the plateau component was generated by a progressive increase in either the L-type current or the non-inactivating R-type current (or by both events), the effect of nifedipine during the run-up occurrence was measured. Indeed, the non-inactivating R-type current did not appreciably change in amplitude, although the L-type current almost doubled in size (Fig.19 *C*). In summary: three distinct Ca^{2+} channel types have been identified in frog canal hair cells according to their biophysical and pharmacological properties. The one carrying most of the current is a non-inactivating L-type channel, the two other channels have been tentatively identified as R-type on the basis of their resistance to dihydropyridines, ω-cono- and aga-toxins. The first channel, termed R1, shows Ca^{2+}-dependent inactivation; the second, R2, sustains a non-inactivating current. The L and R2 currents, which activate at –60 mV and peak at –20 mV, may sustain the ongoing spontaneous transmitter release at the cytoneural junction, whereas the R1 component, which activates at a more positive membrane potential and peaks at –30 mV, may be functionally important in evoking the fast synchronous transmitter release in response to short, strong stimuli.

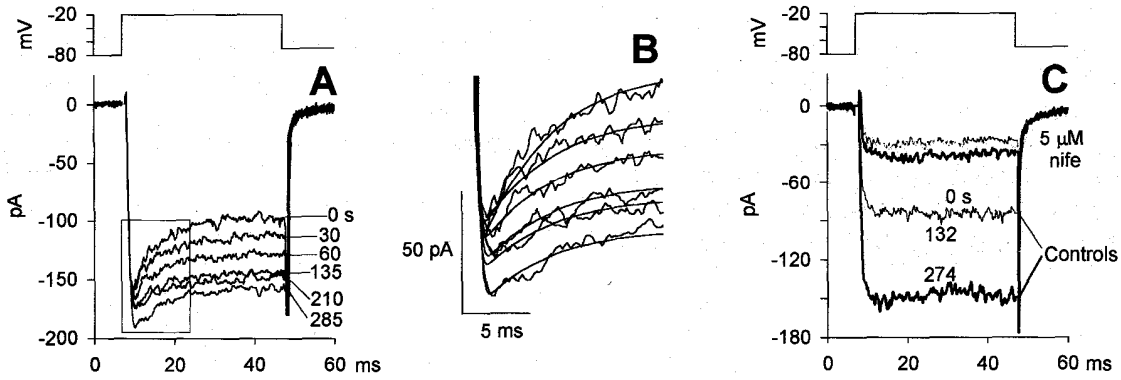

Fig. 19. Run-up of the plateau component. Current was tested with 40-ms depolarizing voltage steps to -20 mV, repeated every 15 s; **A**, Cell displaying a particularly large peak current, where the run-down of the peak component and the run-up of the plateau component were evident. Representative traces were recorded at the beginning of the experiment (0 s) and at five subsequent times indicated near each trace. **B**, Enlargement of the same traces as in *A (box)* and fits to Eq. 1 of the data *(smooth lines).* **C**, Run-up of a cell lacking the sag component and effect of nifedipine on the current recorded at 0 s *(thin black trace),* 132 s *(thick gray trace),* and 274 s *(thick black trace).*

The potassium currents

Major K^+ voltage-dependent currents in frog labyrinth have been found to include: 1) a fast transient current, I_A; 2) a delayed current, generated by a mix of a non-inactivating current, I_{KV}, and a Ca-dependent current, I_{KCa}. Previous attempts at dissecting these individual currents, or at least the fast transient IA from the delayed currents, based on pharmacological treatments or voltage protocols, have been only partially successful (Masetto et al., 1994). In our lab a detailed analysis the kinetic properties of the development and removal ("recovery") of inactivation of the fast and slow potassium currents has been recently carried out. A straightforward voltage protocol, capable to isolate almost pure current tracings, in each hair cell and over a wide membrane potential range, has been developed. This way, the independent description of activation and inactivation kinetics was derived for both I_A and delayed currents. Finally, attention has been paid to the currents evoked by protocols that reproduce physiological conditions, i.e. depolarisations starting from appropriate membrane potential levels within the voltage range into which the cell is expected to physiologically operate. The role of I_A in hair cell electrogenesis is controversial, since in many cases (e.g., at the presumed resting potential of saccular or cochlear hair cells) I_A might hardly be available. We have shown in our lab that in the frog semicircular canal it is possible to precisely isolate the I_A, reliably define its time course, and describe its inactivation mechanism and its kinetics; the A current so characterised results to dynamically contribute to membrane potential shifts – and sensory signal processing – during the excitatory-inhibitory phases of the normal hair cell activity, and its contribution is likely to become more relevant under conditions of activation of the efferent inhibitory system. These results (Martini et al., 2009) are described here in detail, since they are necessary for a better understanding of the new findings presented below.

Hair cell passive properties

It was obviously impossible to localise the original position of each dissociated hair cell within the crista ampullaris. However, the cell type could be recognised: the cells used in that study were classified, and their passive parameters are listed as follows:

Cell type	Cell input resistance GΩ	Cell input capacitance pF	Zero current membrane potential mV
Cylinder-like (n = 71)	1.5 ± 0.1	9.5 ± 0.4	-69.8 ± 2.2
Pear-like (n = 27)	1.1 ± 0.1	10.2 ± 0.7	-67.5 ± 3.3
Club-like (n = 7)	1.2 ± 0.6	8.5 ± 0.4	-72.1 ± 3.6
Uncertain (n = 9)	1.4 ± 0.4	10.7 ± 1.4	-66.3 ± 5.3

These data indicate that the basic resting properties of the isolated hair cells that survive the dissociation procedures were relatively homogeneous; it should be noted that the present zero-current membrane potential values are slightly more negative than those previously measured in dissociated cells or in intact hair cells in thin slices of the crista ampullaris of the frog.

General properties of the currents

The profile of the active currents evoked by depolarisation in isolated hair cells strongly depends on the starting membrane potential. The typical behaviour is summarised in the families of currents illustrated in Fig. 20 a-c. Slow, persistent, noisy outward currents characterise the responses to depolarising steps from a holding potential of -40 mV; conversely, a large and partially transient outward current prevails, when starting from a -90 mV holding level. Current inactivation, and its voltage dependence, appears therefore to constitute a critical aspect in dissecting potassium currents.

Currents evoked from -40 mV holding potential

In control hair cells examined at mildly negative holding potential, namely -40 mV, the I_A current can be considered to be fully inactivated (see below). The only currents that can be activated under this condition are the delayed potassium currents, I_{KD}, i.e. a mix of a non-inactivating current, I_{KV}, and a Ca-dependent fraction, I_{KCa}. From this holding potential, currents were evoked by voltage commands up to +80 mV. The compound outward current rapidly built-up up to a value proportional to the applied voltage step and thereafter settled, in about 50 ms, to a persistent level.

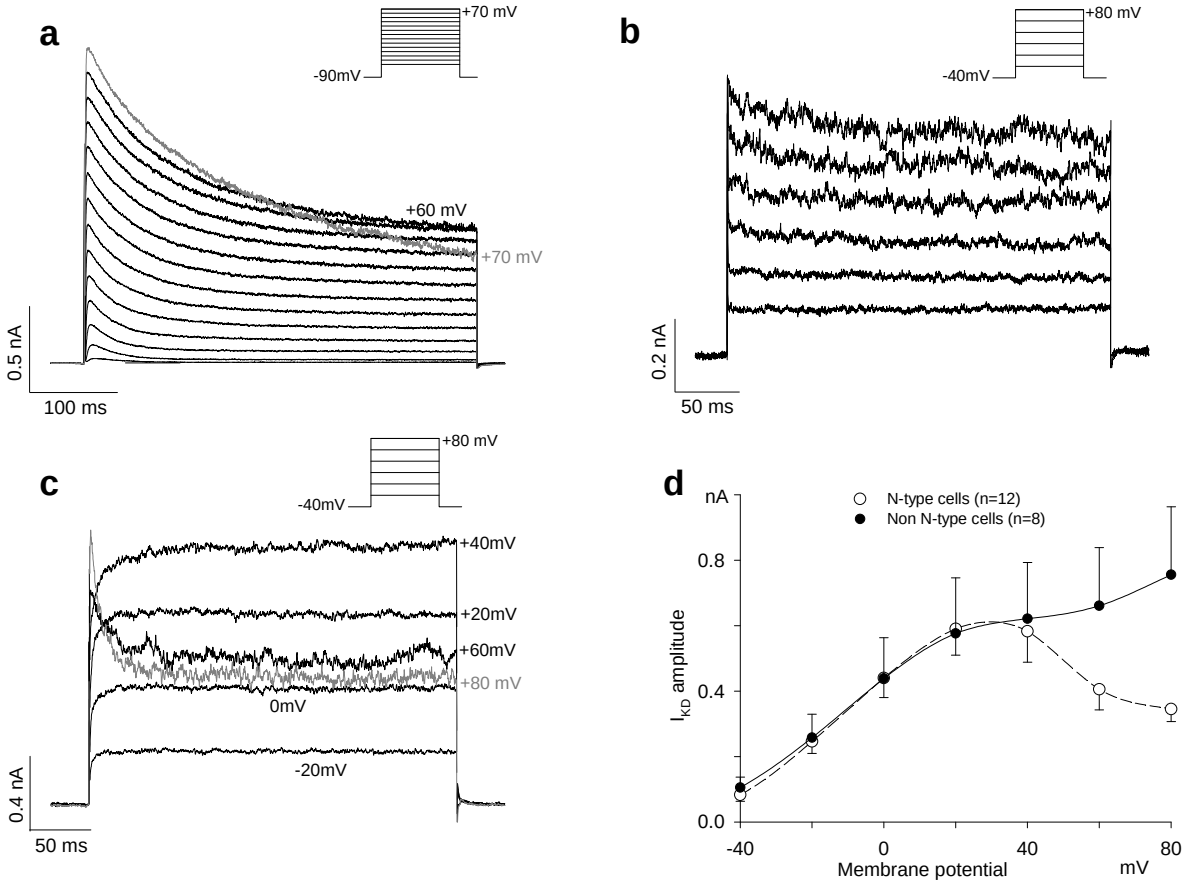

Fig. 20. (**a**) Representative family of currents evoked in the -60/+70 mV voltage range, in 10 mV steps, in an isolated hair cell held at -90 mV. Note the late decay of current flow in the +60/+70 mV tracings. (**b-c**) Current tracings evoked in the -20/+80 mV voltage range (in 20 mV steps) in typical non-N (**b**) or N-type (**c**) hair cells from a -40 mV holding potential. (**d**) Mean I-V plots for hair cells classified as N-type (open circles; n = 12) or non-N-type (filled circles; n = 8).

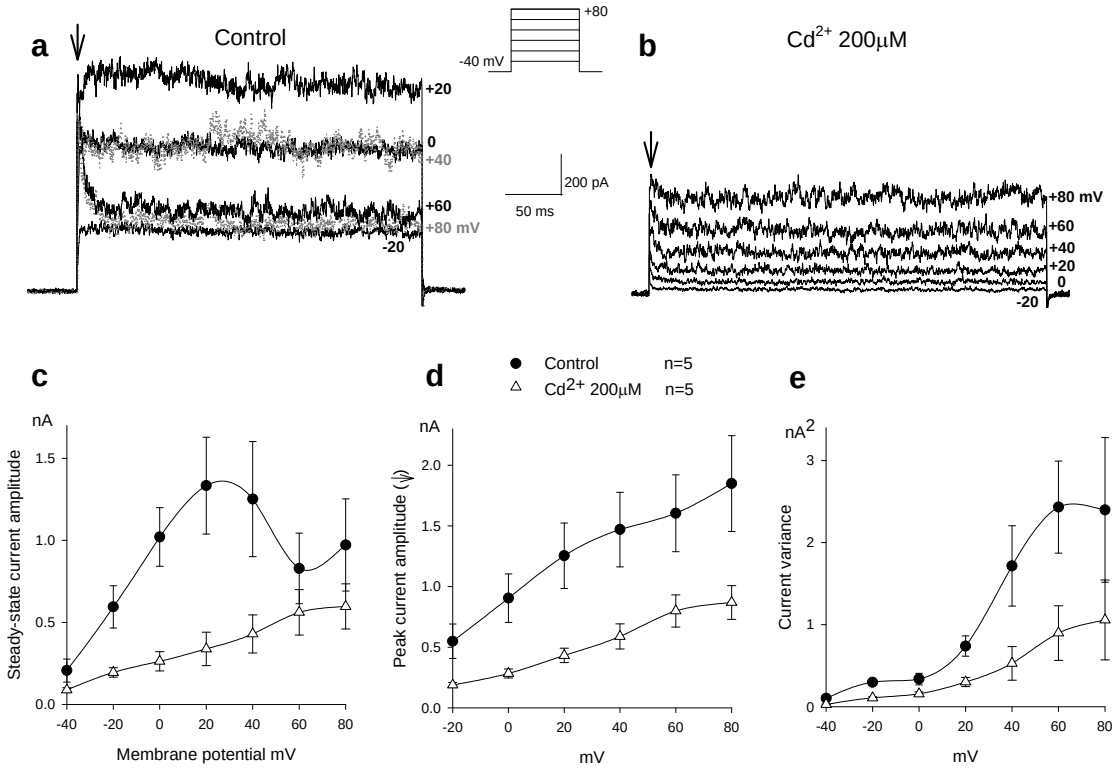

Fig. 21. (**a-b**) Typical current families elicited in the same hair cell in the -40/+80 mV voltage range before (**a**) and after (**b**) fast application of 200µM Cd^{2+}. Holding potential was -40 mV throughout. (**c-d**) Mean I-V plots from 5 cells in the -40/+80 mV voltage range before (filled circles) and after fast perfusion of 200 µM Cd^{2+} (triangles). Steady-state current amplitude is illustrated in (**c**), while the amplitude of the early transient peak (arrows) is shown in (**d**). (**e**) Noise variance of the steady-state current recorded at different voltage levels in the two cell groups illustrated in (**c-d**).

This steady level monotonically increased with the command voltage, up to +80 mV, in 8 out of the 20 cells of our sample (Fig. 21 b,d - filled circles), while in the remaining 12 cells its magnitude only increased up to +20 mV, and clearly decreased above +40 mV (Fig. 21 c,d - open circles), giving rise to a prominent local peak in the current profile and to a "N-shaped" steady-state I-V plot (the N shape arises because the steady current increases again, above +60 mV; see also Fig. 21 c). The mean I-V curves of the non-N and N-type cells are shown in Fig. 20 d.

The component of K^+ current that rapidly sets off and vanishes at very positive potentials may be related to the kinetics of Ca^{2+} inflow, which initially is intense but rapidly fades as the command membrane potential approaches the Ca^{2+} equilibrium potential. The involvement of Ca^{2+} inflow was confirmed in a group of hair cells, in which the N-type profile of the I-V curves was particularly evident. Rapid perfusion of 200 μM Cd^{2+} onto the cell (a powerful blocking procedure for any voltage-dependent Ca^{2+} channel) abolished a major fraction of the outward current and the initial peak at highly positive potentials (Fig. 21 b,d). The current tracings became virtually square at all voltage levels, with an initial peak slightly higher than the steady value (this may constitute either a partial inactivation of I_{KV} or a shift in K^+ distribution); a monotonic current-to-voltage relation was generated and the N-shape behaviour of control cells was completely cancelled (Fig. 21 c). The current noise variance, measured on a 100 ms section of the recording at steady state during the command voltage step, was drastically reduced by Cd^{2+} (Fig. 21 e), suggesting that a major contribution to the variance arises from Ca-activated channels. Consistently, the fraction of current noise variance abolished by Cd^{2+} was not the same at all potentials. In general, noise variance should change with $p \cdot (1 - p)$, where p is the open probability of the channel; thus the noise variance abolished by Cd^{2+} should be minimal when Ca^{2+}-dependent channels are scarcely or strongly activated: experimentally, the effect of Cd^{2+} on current variance was small at negative membrane potential values, where I_{KCa} is little activated because Ca^{2+} channels are shut, was maximal for mildly positive potentials and decreased at highly positive potentials, where the driving force for Ca^{2+} begins to decrease; however, it was also depressed near 0 mV, where Ca^{2+} influx should be maximal (and the open probability of I_{KCa} is likely to approach 1, thereby reducing noise variance). Voltage-dependent calcium currents are well characterised in frog hair cells. The calcium participation in the whole current flow of Figs. 20, 21 is quantitatively limited (a mean amplitude of about -15/-20 pA at +20 mV), as compared with the potassium current amplitudes.

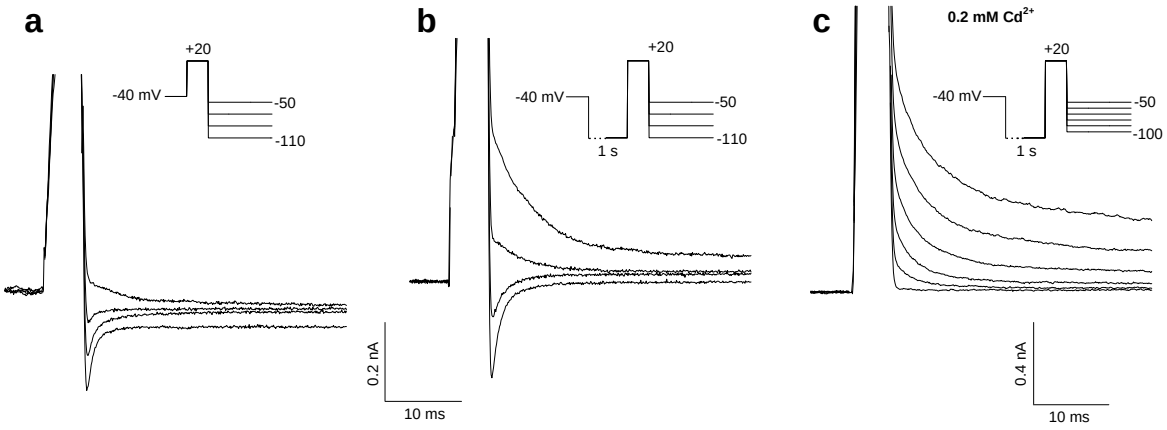

Fig. 22. Tail currents recorded in hair cells upon repolarising the membrane in the -50/-110 mV voltage range. Currents were evoked by 5 ms pulses to +20 mV, starting from a holding potential of -40 mV (**a**), or after 1s preconditioning at -110 mV (**b,c**); peak amplitudes of the currents during the depolarising pulse (out of scale) were 0.71, 1.82 and 3.94 nA, respectively. (**a,b**) from the same cell; (**c**) from a different cell exposed to 200 μM Cd^{2+}. Plots of tail current amplitude vs. membrane potential (not shown) suggest a current equilibrium potential of -61 mV in (**a**), -81 mV in (**b**) and -100 mV in (**c**).

The presence of calcium conductances is more readily evident in observing how much the reversal potential of the tail currents departs from K^+ equilibrium potential under different conditions.

With relatively small potassium currents (holding potential -40 mV; Fig. 22 a), the apparent reversal potential of the tail current following a pulse to +20 mV was about -61 mV (peak outward current 0.7 nA and mean reversal potential of the tail current -52.0 ± 5.6 mV, in a 4-cell sample). The application of a preconditioning 1-s pulse at -110 mV recruited further potassium current components and the reversal potential shifted to -81 mV (Fig. 22 b): the peak outward current during the pulse to +20 mV reached 1.8 nA, and the mean reversal potential for the tail currents was –80.0 ± 5.6 mV, in the same 4-cell sample. Independent of the holding potential, almost pure potassium currents were observed after blockade of calcium ion inflow by Cd^{2+}; under these conditions the tail current null point approached the Nernstian equilibrium potential for potassium ion (-96 mV; Fig. 22 c).

The N-shaped profile in the I-V curves, observed with a holding potential of -40 mV, cannot generally be seen with more negative holding potentials, because the recordings, and especially the initial part of the responses, are dominated by large outward currents with a monotonically increasing amplitude. However, in some cells late currents did display a discernible decrease at very positive potentials, also when starting from a –90 mV holding potential (e.g. Fig. 20 a, +60 and +70 mV).

Participation of chloride current in these effects was ruled out by substituting isethionate for chloride ions, or by using specific chloride channel blockers such as 9AC (data not shown). Similarly, any I_A component was excluded by considering that the activation of this current starts at -40 mV membrane potential.

In turtle hair cells with free-standing hair bundles, sensory mechano-transduction channels are opened by depolarisations positive to 0 mV. Though no adaptation or inactivation was reported for this current in other systems, we performed a series of tests to exclude that transducer channels contributed to the transient outward component observed here. No effects on the currents were observed after applying permeating channel blockers such as 1 mM methylene blue (which is expected to block about 90% of the transduction current at +60 mV), or 50 μM gadolinium chloride, or after substituting TRIS for external sodium. Thus, calcium involvement remains the most plausible explanation for the appearance of a transient component of I_{KD} and the decrease of late current at highly positive potentials. Calcium ions entering the cell during the early large depolarisation would strongly activate I_{KCa}, which is usually both Ca- and

voltage-dependent. Close to the equilibrium potential, however, calcium inflow would rapidly wane and I_{KCa} would consistently decline, since this current apparently requires to be continuously fed by a maintained calcium influx. The deactivation time constant of maxi K^+ channels in a membrane patch from guinea-pig myocytes after application of a transient calcium pulse was about 18 ms at +50 mV, and about 20 ms for BK channels activated by calcium sparks released from the sarcoplasmic reticulum. A similar observation was obtained in rat chromaffin cells after brief calcium immission. The decay time course of the outward current transients of Fig. 20 c and 21 a are in line with these findings, thus suggesting that this behaviour might actually be related to deactivation of a Ca-dependent current.

Currents evoked from more negative holding potentials

As previously reported, hair cells express a fast transient potassium current, I_A, which is completely inactivated at potentials above -40 mV. Hyperpolarising conditioning pulses remove this inactivation. Following such conditioning, positive voltage pulses evoke a mix of currents in which the delayed current described above summates to the I_A. A simple procedure to isolate the I_A component consists in subtracting the tracings without preconditioning to those obtained after preconditioning at negative potentials. As originally observed in *Anisodoris*, this manoeuvre can be successfully applied only if the slow outward current is not affected by any voltage-dependent inactivation. In hair cells, difference tracings usually exhibit a persistent current pedestal at times when I_A inactivation should be complete; return to zero level is only observed when the conditioning pulse is to mildly negative membrane potentials (about –70 mV) or particularly brief - see for example Fig. 23 d(a). Under these conditions, the I_A current recovered by the short preconditioning pulse is fully inactivated within about 200-300 ms, and the sole delayed current fraction, unaffected by the brief/mild preconditioning pulse, survives at later times. It appears, therefore, that two distinct mechanisms of inactivation coexist at hair cells: they separately involve I_A and delayed currents, and are removed by conditioning pulses with different time courses and voltage dependencies. To better understand these processes, the development and removal of current inactivation have been separately analysed for the two current types.

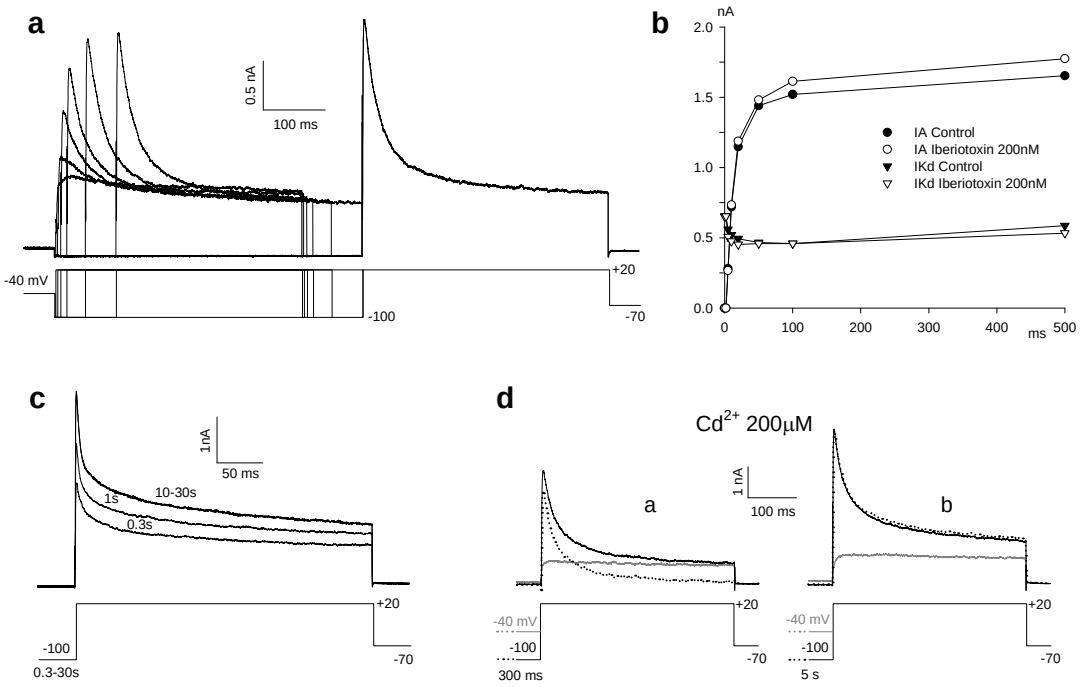

Fig. 23. (**a**) Time course of fast IA recovery at -100 mV. Starting from a –40 mV holding potential (I_A fully inactivated), the currents were elicited at +20 mV following a conditioning pulse of variable duration at –100 mV. (**b**) The amplitudes of the transient peak (I_A, circles) and the steady-state component (I_{KD}, triangles) of the evoked currents are plotted vs. the conditioning period duration (filled symbols), and compared with the same measurements after exposure of the same cell to 200nM iberiotoxin (open symbols). Note the time course of IA inactivation removal as opposed to the lack of any significant effect on I_{KD} amplitude. (**c**) The I_A and I_{KD} growth following long-lasting conditioning pulses of increasing duration (0.3, 1, 10 and 30 s) demonstrates the presence of a slow recovery component in both conductances. Each trial was followed by a 30 s period at -40 mV to allow for complete inactivation. (**d**) Recordings obtained in the presence of 200µM Cd^{2+} to show the calcium-independence of the slow conductance modifications. A short preconditioning of 300 ms at -100 mV, insufficient to remove any I_{KD} inactivation, selectively removes inactivation of I_A, that can be dissected out as a current decaying to zero by utilising the subtraction procedure (dotted, a). Recovery of both IA and I_{KD} current fractions from inactivation is revealed in the same cell by a 5 s sojourn at -100 mV. Eight cycles were subsequently repeated, in which the cell was preconditioned, pulsed to +20 mV, maintained at -40 mV for 30 s and pulsed to +20 mV without preconditioning. The first and last (dotted) cycles are illustrated to demonstrate the lack of memory from previous episodes (b).

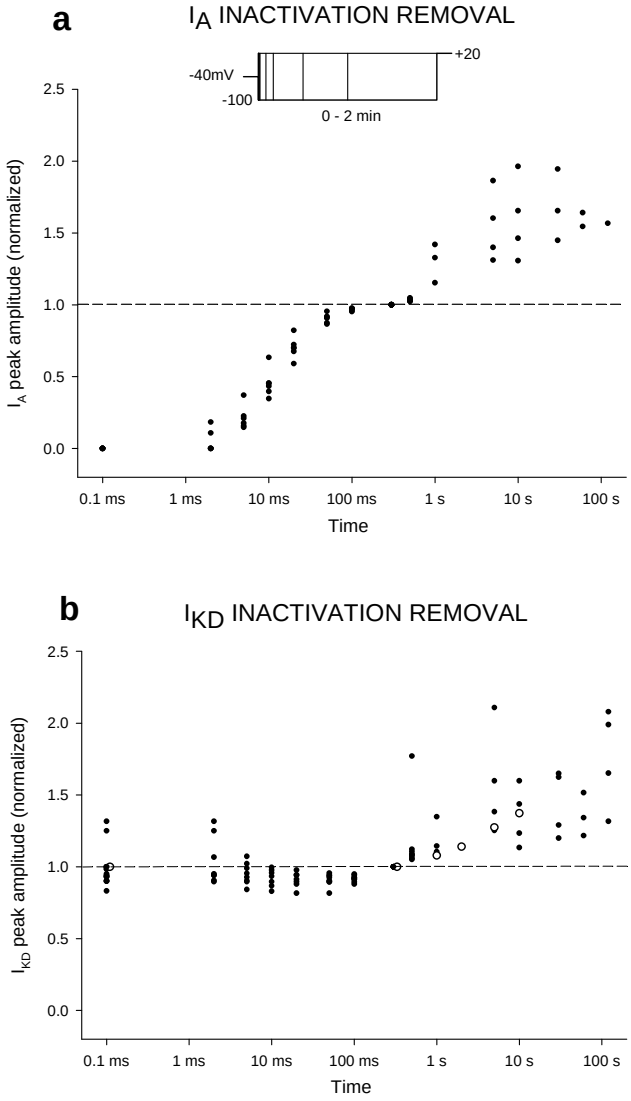

Fig. 24. Time course of I_A and I_{KD} fast and slow inactivation removal. (**a**) Peak I_A amplitudes from experiments similar to those illustrated in Fig. 23 a,c are plotted vs. the duration of the conditioning pulse at -100 mV. Holding potential was – 40 mV throughout. Data were obtained from 6 cells to analyse fast removal (2-300 ms conditioning duration range), or from 10 different cells to analyse slow inactivation removal (300 ms-100 s conditioning duration). In the latter experiments, successive trials were separated by a 30 s period at -40 mV to avoid any summation in the recovery mechanism. All data are normalised to the responses obtained from each cell following a 300 ms conditioning period. (**b**) Plot of I_{KD} steady-state amplitude vs. duration of the conditioning period at -100 mV. The plot demonstrates the absence of fast recovery and the presence of slow inactivation removal. Data from 8 cells for 2-300 ms conditioning at -100 mV; data from 10 different cells for the long-lasting conditioning. All data normalised as in (**a**). Open circles illustrate data from a cell conditioned at -70 mV.

The kinetics of fast and slow removal of I_A and I_{KD} inactivation

Fast inactivation removal at -100 mV was studied in double-pulse experiments. I_A recovery was evaluated by holding the cells at –40 mV (I_A fully inactivated) and stepping to +20 mV after a conditioning pulse (–100 mV) of variable duration. Peak I_A was computed by subtracting to such current recordings the current measured with no pre-pulse. I_{KD} recovery was evaluated in the same current difference tracings after 400 ms at +20 mV, when I_A is completely inactivated. The cumulative results are shown in Fig. 24, left part of the graphs (conditioning pre-pulse durations in the 2-300 ms range). The behaviours of both I_A and delayed currents are illustrated in Fig. 23 a,b. As concerns the transient component, it is evident that a fast process of I_A recovery (inactivation removal) operated, and displayed a single exponential time course (see Fig. 24 a). The mean value of its time constant, τ_{hA} , was 18.2±1.6 ms at -100 mV; fast recovery was complete within about 80 ms in all the hair cells of the sample, and was stable for an additional 100 ms period thereafter. In this same range of preconditioning pulse durations, no changes were observed in I_{KD} amplitude (see Fig 24 b), thereby indicating that possible inactivation of delayed K^+ currents was not removed by brief preconditioning pulses (I_{KD} amplitude at +20 mV = 844±139 pA without preconditioning vs. 870±172 pA after 300 ms preconditioning at -100 mV).

In 6 different cells, fast I_A recovery was studied at -70 mV, a membrane potential close to the zero-current level of the isolated cells. Again, inactivation removal ensued with a single-exponential time course; the mean value of τ_{hA} = 18.3±4.6 ms was virtually identical to the value observed with pre-pulses at -100 mV. A 5-ms sojourn at -70 mV was thus sufficient for the cell to recover 2 nS A-conductance. In the same experiments, inactivation removal of the delayed current component was negligible during the first 200 ms of the conditioning step.

In addition to fast inactivation processes, slow voltage-dependent recovery mechanisms are present in the frog hair cells, and their characterisation is illustrated in the right part of the graphs in Fig. 24. A typical experiment is shown in Fig. 23 c: the cell was clamped at -100 mV for a time period of 300 ms to 30 s, and a final test depolarisation to +20 mV was then applied. Both I_A and delayed current fractions increased in amplitude as the long-lasting conditioning pulse was prolonged. The maintained current fraction markedly increased, whereas there was no apparent change in the time course of the I_A currents. The kinetics of inactivation removal of the slow components was studied in a group of 10 cells, in experiments similar to those used to describe fast recovery; the results are illustrated in Fig. 24 ab, over the time scale range to the right of 300 ms pre-conditioning

duration. All data from each cell are normalised to the corresponding measurement for 300 ms conditioning pulse duration, to make data from different cells readily comparable. Fast recovery was only observed for the I_A component and was complete within 300 ms (previous observations, Fig. 24 a, left part). A second slow phase of inactivation removal ensued after this time (these new experiments). Single cells were maintained at a holding potential of -40 mV, and held at this potential for at least 30 s between successive conditioning episodes, thus ensuring that slow inactivation processes had fully developed before starting with a new conditioning period.

The slow removal of I_A inactivation at -100 mV consistently increased the peak I_A evoked at +20 mV. After 10 s preconditioning (n = 4) peak I_A reached a value 1.6 times larger than after completion of fast recovery (300 ms). Slow I_A recovery did not display consistent, well defined kinetics, and occasionally proceeded for even more than 1 min during preconditioning. It is worth noting that although recovery took tens of seconds, the onset of IA inactivation was always fast, and was generally complete within a 1-s sojourn at -40 mV.

The delayed current, which was originally thought to be exempt of inactivation, did not display any fast recovery but exhibited a well detectable process of slow inactivation recovery from inactivation, which only ensued after a delay of about 300 ms. Data from 10 cells are presented in Fig. 24 b. Full recovery produced a consistent amplitude increase for the delayed current: the increase factor averaged 1.4 after 5 s preconditioning (n = 5) and 1.8 after 100 s preconditioning (n = 4; Fig. 24 b). Even larger effects were noticed in single sets of experiments (see, for example, Fig. 25 b and Fig. 28). The kinetics of inactivation removal followed a single exponential time course in these experiments; typically, in a cell maintained at -70 mV (Fig. 24 b, open circles) a time constant of 3.3 s was estimated.

Contrary to I_A, whose fast and slowly recovering components both fully inactivated within 1 s, the delayed current inactivation developed over a more complicated time course. To study the kinetics of this process, the hair cell was held at –70 mV; pre-conditioning was performed by applying a 2-s step at -100 mV (inactivation removal), followed by a 400 ms depolarisation at +20 mV (I_A inactivation); after a variable interval at –40 mV, during which I_{KD} inactivation developed, a test pulse to +20 mV was applied to fully activate any available I_{KD}: the sequence was repeated several times, and the kinetics of inactivation development were deduced from the decline of the response as a function of the time interval between conditioning and test pulse.

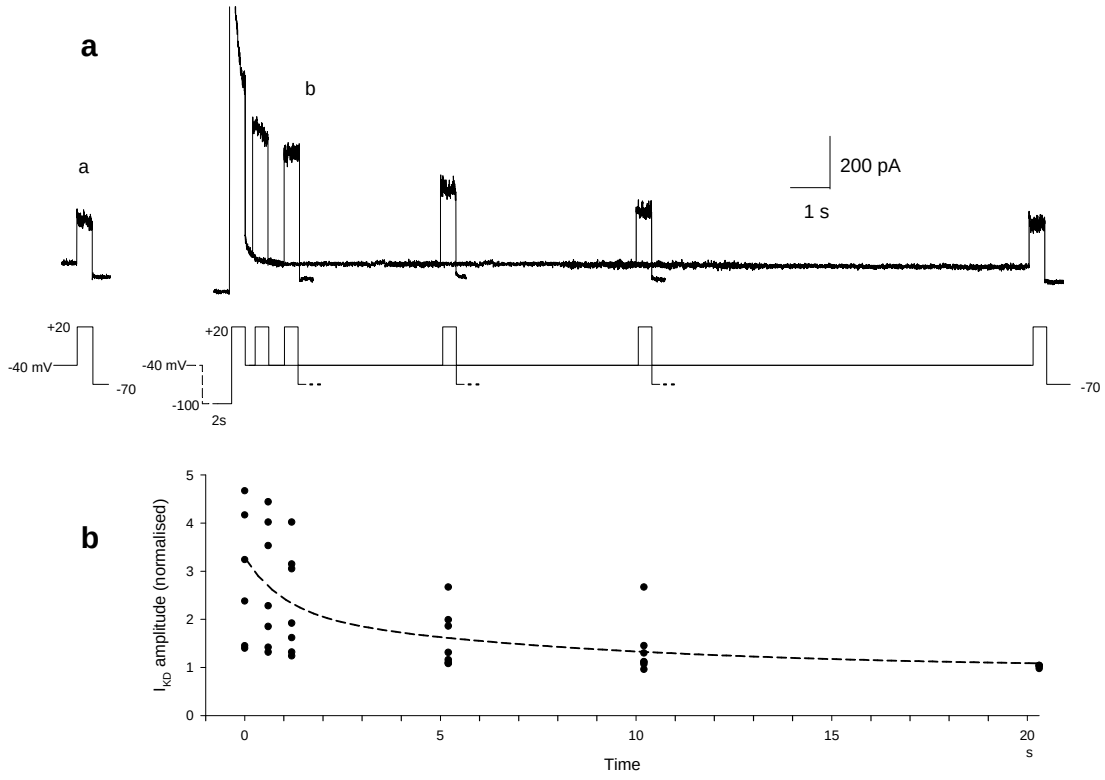

Fig. 25. Analysis of the time course of I_{KD} inactivation development, measured by pulsing a cell to +20 mV at variable time intervals following a 2 s conditioning step at -100 mV, to remove inactivation. (**a**) Typical behaviour of a cell repeatedly pulsed to +20 mV to evoke both I_A (peak out of scale) and I_{KD}, and thereafter maintained at -40 mV to preserve I_A inactivated; test voltage commands to +20 mV were subsequently applied after intervals of increasing duration (200 ms to 20 s) to evaluate the development of I_{KD} inactivation (current tracings are superimposed; b). A 30 s period at -40 mV was allowed between successive trials to reset inactivation mechanisms. I_{KD} amplitude in the absence of conditioning is shown in (a). (**b**) Time course of the development of I_{KD} inactivation at -40 mV in a 7 cell sample. Data, from experiments similar to that shown in (**a**), are normalised to the preconditioning current amplitude. The dashed curve represents a two-exponential best fit to data points (time constants: τ_{fast} = 0.95 s and τ_{slow} = 7.69 s).

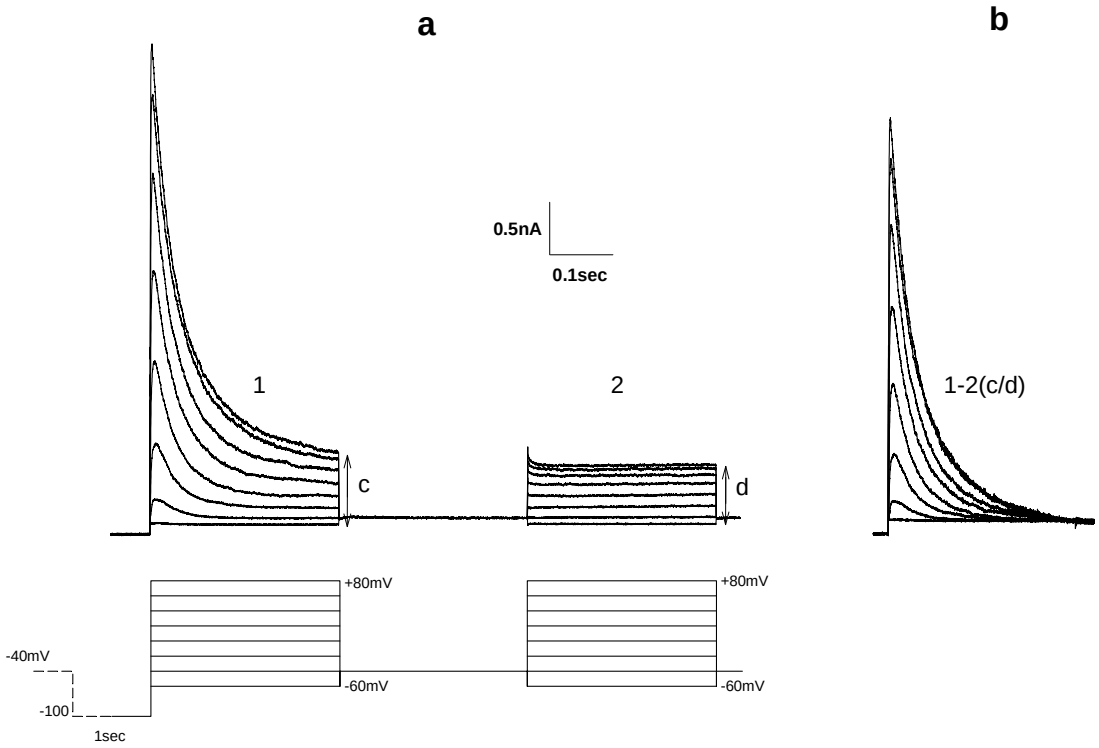

Fig. 26. Time course of I_A and I_{KD} fast and slow inactivation removal. (**a**) Peak I_A amplitudes from experiments similar to those illustrated in Fig. 23 a,c are plotted vs. the duration of the conditioning pulse at -100 mV. Holding potential was – 40 mV throughout. Data were obtained from 6 cells to analyse fast removal (2-300 ms conditioning duration range), or from 10 different cells to analyse slow inactivation removal (300 ms-100 s conditioning duration). In the latter experiments, successive trials were separated by a 30 s period at -40 mV to avoid any summation in the recovery mechanism. All data are normalised to the responses obtained from each cell following a 300 ms conditioning period. (**b**) Plot of I_{KD} steady-state amplitude vs. duration of the conditioning period at -100 mV. The plot demonstrates the absence of fast recovery and the presence of slow inactivation removal. Data from 8 cells for 2-300 ms conditioning at -100 mV; data from 10 different cells for the long-lasting conditioning. All data normalised as in (**a**). Open circles illustrate data from a cell conditioned at -70 mV.

The process proved to be unexpectedly slow, as illustrated by the typical tracings of Fig. 25a and by the plot of the cumulative data from 7 cells shown in Fig. 25b. The effect of preconditioning persisted for more than 10 s: 1 s after preconditioning the amplitude of the delayed current was larger than in the absence of preconditioning and recovery (Fig 25 a(a)) by a mean factor of 2, and 5 s after preconditioning it was still larger by a factor of 1.4. Two time constant components could be detected during the onset of inactivation; the mean τ values in the cell group illustrated in Fig. 25 b were 0.95 s for the fast component, and 7.69 s for the slow component. The inactivation mechanisms described above (fast and slow inactivation removal or development) were Ca^{2+}-independent, and no memory was maintained in the cell from previous episodes. This is shown in Fig. 23 d, in which the same cell bathed in 200μM Cd^{2+} was exposed to 8 successive cycles of slow inactivation removal/development, without any permanent modification in the I_A or delayed current characteristics. Similarly ineffective on fast inactivation removal was the application of 200 nM iberiotoxin, a well known blocker of the Ca-dependent potassium conductance in many systems.

It may be appropriate to observe that whereas the I_A is fully inactivated by depolarisation (and thereafter undergoes the fast and slow recovery processes), the inactivation process and the very slow recovery from such inactivation appear to affect only a minor fraction of the delayed currents.

I_A and I_{KD} dissection

In these experiments, the I_A current exhibited fast onset of inactivation and both fast and slow mechanisms of inactivation removal, while the delayed current did not display any fast inactivation process, and the slow recovery mechanism arose with a substantial delay. These conclusions indicate that an appropriate mix of voltage-time conditioning parameters can neatly dissect the I_A component [Fig. 23 d(a)], and provide the rationale for an efficient voltage protocol to study the I_A and delayed currents in isolation, dissected in the same cell in the absence of any pharmacological treatment. An example is illustrated in Fig. 26 In Fig. 26 (**a**) the cell was held for *30 s at -40 mV*, to fully inactivate I_A and the fraction of delayed currents subject to inactivation; a 1-s conditioning pulse at -100 mV was applied to remove inactivation of both I_A and delayed currents, which were thereafter evoked together during a 300 ms test pulse (Fig. 26 a1) The cell was then returned to -40 mV for 300 ms and subjected to a second 300 ms pulse to the same test voltage. The procedure was repeated with test voltages in the –60/+80 mV range (in 20 mV steps). The interval at –40 mV between the two test pulses in each

cycle features a sufficiently positive voltage to maintain full I_A inactivation (thus the second test pulse only evokes pure I_{KD} components) and a duration which minimises the development of slow current inactivation; in fact, amplitudes at "c" are slightly larger than at "d" in Fig. 26. In line with the predictions of Fig 25 b (dashed curve), the amount of inactivation that develops during the 300 ms sojourn at -40 mV, between the two test pulses, accounts for a mean 17% decrease of delayed current amplitude (c/d ~ 1.1 in Fig. 26 a). Once the second pulse currents (Fig. 26 a2) are corrected for this, the difference currents (1 - 2 × c/d in Fig 26 a) dissect out the complete IA family over the whole voltage range (Fig.26 b). A non-N-type hair cell is illustrated in this figure; the I_A isolation was equally successful in the case of N-type hair cells (not shown).

I_A general properties

By applying the procedure just described, separate I-V curves were obtained for peak I_A and maximum I_{KD} over the -50/+80 mV voltage range; they are shown in Fig. 27 a,b (filled circles). As concerns I_A, the current appeared to be significantly activated at membrane potentials more positive than -40 mV; above this value, its amplitude increased monotonically with increasing depolarisation. A first-order kinetics could be detected from the analysis of the current rise time course and a voltage-dependent activation time constant was defined (2.5 ± 0.4 ms at -40 mV; 1.1 ± 0.3 ms at 0 mV; 0.8 ± 0.3 ms at +40 mV; 0.6 ± 0.2 ms at +80 mV – n = 9). Once activated, the I_A then systematically declined to zero. In all examined cells the decay time courses of the currents, evoked in the -40/+0 mV voltage range, were mono-exponential (τ_f = 42.0 ± 9.9 ms at -40 mV; 30.8 ± 6.5 ms at -20 mV and 27.1 ± 6.0 ms at 0 mV). Above 0 mV, the current decay was described by a double-exponential time course in 10 out of 12 cells examined, because the current decay was initially faster than at later times (Figs. 26 b and 29 b). The second time constant, which flanked the fast time constant detected at less positive voltage, accounted for a progressively larger fraction of the total current (up to 80%). Both time constants proved to be voltage-independent in the +20/+80 mV range (τ_f = 16.1 ± 4.1 ms at +20 mV, 16.6 ± 3.4 ms at +80 mV; τ_s = 111.9 ± 24.6 ms at +20 mV, 114.4 ± 22.3 ms at +80 mV). The omission of calcium in the bath, or the perfusion with Cd^{2+}, did not affect the peak I-V curve or the time course of I_A decay in three cells, so that the results were pooled. In the hair cells, thus, I_A appears as a genuine current which is not influenced by Ca^{2+} influx. A double-exponential decay of I_A current has been described by Norris et al. (1992) in 'fast' and 'slow' isolated hair cells of the leopard frog. Similarly, Russo et al. (2007) have recently demonstrated the presence of

two classes of I_A in thin slices of the frog crista ampullaris, which differed in exhibiting fast or slow inactivation rates depending on their localisation in the slice. The present data are, quantitatively, significantly different from those reported there. The large variability in the I_A decay parameters observed in our experiments, especially as concerns τ_f values, could actually reflect sampling from a mix of different types of hair cells; the different procedures of current isolation and the limited size of our sample, however, make any direct comparison with previous data inconclusive. The mean I-V curve for I_A is illustrated in Fig. 27 a. From these data the g_A conductance was estimated using the relation $g = I/(V - V_K)$, with $V_K = -96$ mV, as is the case for pure potassium currents. A g_A conductance vs. voltage relationship was obtained, which was well described by a Boltzmann-type equation with the following parameters: size, g_{Amax} = 13.3 nS; centre voltage, Vc = -5.7 mV; slope factor, VS = 24.3 mV.

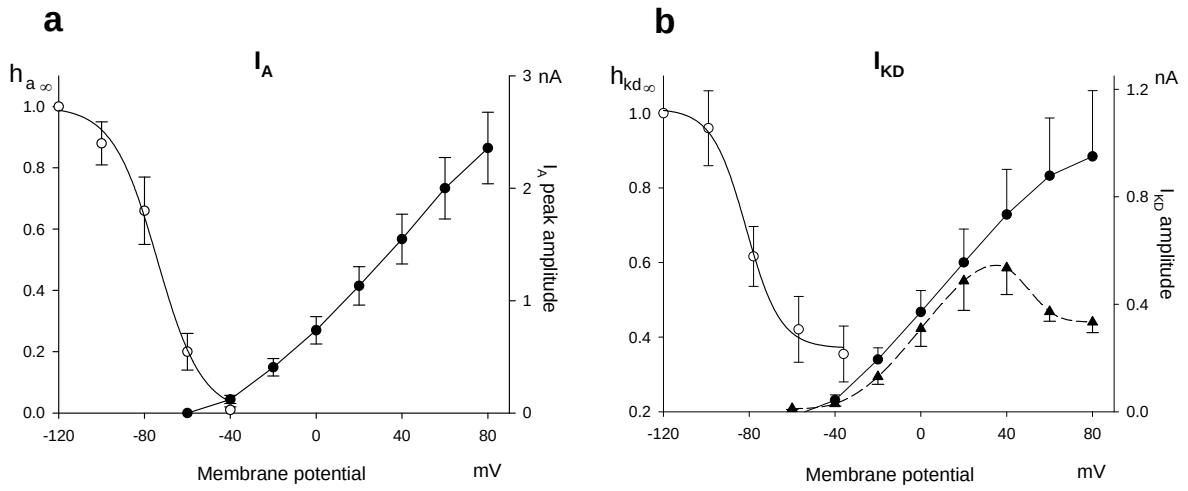

Fig. 27. (**a**) Mean I-V curve (filled circles, n = 12) and steady-state inactivation curve, $h_{a\infty}$, (open circles, n = 7) for I_A. Data from difference tracings to isolate IA according to the procedure illustrated in Fig. 26. (**b**) Mean I-V curves of N-type (triangles, n = 5) and non N-type hair cells (filled circles, n = 10), and steady-state inactivation curve, $h_{kd\infty}$ (open circles, n = 6) for I_{KD}. Steady-state inactivation parameters (normalised) were obtained from experiments similar to that illustrated in Fig. 28. Peak current amplitudes relative to their maximal value were considered for IA and I_{KD}. Note the presence of the non-inactivating I_{KD} fraction at -40 mV in the $h_{kd\infty}$ curve. See text for best fitting Boltzmann-type equations.

I_{KD} general properties

In the present experiments no hair cells completely lacked the I_A component. The delayed currents were thus investigated either when evoked from holding potentials sufficiently positive to inactivate the I_A (-40 mV in the examples of Fig. 20) or from any more negative voltage level (-100 mV in Fig. 27 b), after applying the isolation procedure described in Fig. 26. Under both conditions the results were consistently reproducible, and in particular the current profiles, the I-V plots, the activation-deactivation kinetics of the current, the marked increase in noise with larger depolarising steps, the presence of cells with a non-N or a N-type behaviour, above +40 mV, and the presence of a current fraction blocked by cadmium. These results mutually validate the dissection procedures and indicate that the same current type is dealt with by using both approaches. For mild depolarisations the current description was simple. The onset was fitted by a single time constant of 0.9 ± 0.1 ms at -20 mV, 1.1 ± 0.2 ms at 0 mV and 1.7 ± 0.4 ms at +20 mV (n = 16). The peak current amplitude was rapidly attained and was maintained constant during the whole voltage step, giving a virtually rectangular shape to the tracings evoked in the range -40/+0 mV (in 32/35 cells of our sample); the rectangular profile was preserved up to +20 mV in 21/35 cells, and up to +40 mV in 12/35 cells (Figs. 20, 21, 26). For large positive pulses the current time course was complicated with increasing frequency by the onset of a transient peak (Figs. 20 c and a) and/or the occurrence of a mild current decay during long-lasting pulses. These phenomena reflect the inactivation process described above. I_{KD} tail currents, upon repolarisation, were so small and fast to result largely submerged in the capacitive transients. In a few favourable examples (see Fig. 22), the current rapidly deactivated with a mean time constant of 1.1 ± 0.1 ms at -70 mV and 1.6 ± 0.3 ms at -90 mV (n = 5). From the I-V plots of Fig. 27 b, g_{KD} was estimated in non N-type cells. A conductance-voltage relationship was obtained, well described by a Boltzmann-type equation with the following parameters: g_{KDmax} = 5.5 nS, Vc = –14.9 mV and V_S = 16.7 mV. In a 3-cell sample exposed to 200 µM Cd^{2+} the Boltzmann parameters of the corresponding g_{KD} conductance-voltage curve were: g_{KDmax} = 2.9 nS, Vc = - 10.0 mV and V_S = 44.5 mV.

Isolation and properties of I_{KCa}

The calcium-dependent fraction of I_{KD} in single hair cells was evaluated by applying 200 µM Cd^{2+} by fast superfusion. The difference current recorded before and after blockade of Ca^{2+} influx isolates I_{KCa}. This conventional procedure is illustrated in Fig. 28 a-c (the number of tracings presented is reduced for clarity). The mean I-V curve for I_{KCa} in 5 N-

type-cells is shown in Fig. 28 d (data from the cell sample illustrated in Fig. 21 c; the mean I-V curves for I_{KD} and I_{KV} are reported here for direct comparison). Tracings in Fig. 28 a-c indicate that I_{KCa} dominates the outward currents elicited by steps at command voltages up to +40 mV, but its contribution is reduced to an initial, rapidly vanishing peak, for more positive potentials; this entirely sustains the transient peak in the compound I_{KD}, as no transients are apparent in I_{KV} tracings. In this example, the deactivation (or early switch off) of I_{KCa} was so strong to virtually cancel any sustained current at later times after the transient; the current noise variance decreased, from the +40 to the +80 mV tracing, and slow frequency components were mostly reduced, suggesting that slow, large-conductance calcium-dependent potassium channels were no more activated. Similarly, the N-behaviour observed in the I-V relationship for I_{KD} (Fig. 20 d) becomes more evident when applied to the sole I_{KCa} curve (Fig. 28 d).

At mildly depolarised levels (below 0/+20 mV), only minor differences occur in the current time course when comparing the tracings recorded in the three current families (I_{KD}, I_{KV} or I_{KCa}); thus the major result of dissection appears to be a variable voltage/dependent scaling of the amplitude of the individual currents (Fig. 28 a-c). The activation time constant was measured in the I_{KCa} tracings. The following mean values were obtained: 1.12 ± 0.35 ms at -20 mV; 0.78 ± 0.28 ms at 0 mV; 0.78 ± 0.30 ms at +40 mV; 0.23 ± 0.07 ms at +60 mV. The overall description of the compound I_{KD} presented above thus applies, especially within the voltage range of physiological interest (see below), also to its calcium-dependent fraction.

From the data of Fig. 28 d, the ratio I_{KCa}/I_{KD} was 0.62-0.77 in the -40/+20 mV voltage range; it became smaller at more positive membrane potentials (0.40 and 0.35 at +60 or +80 mV, respectively).

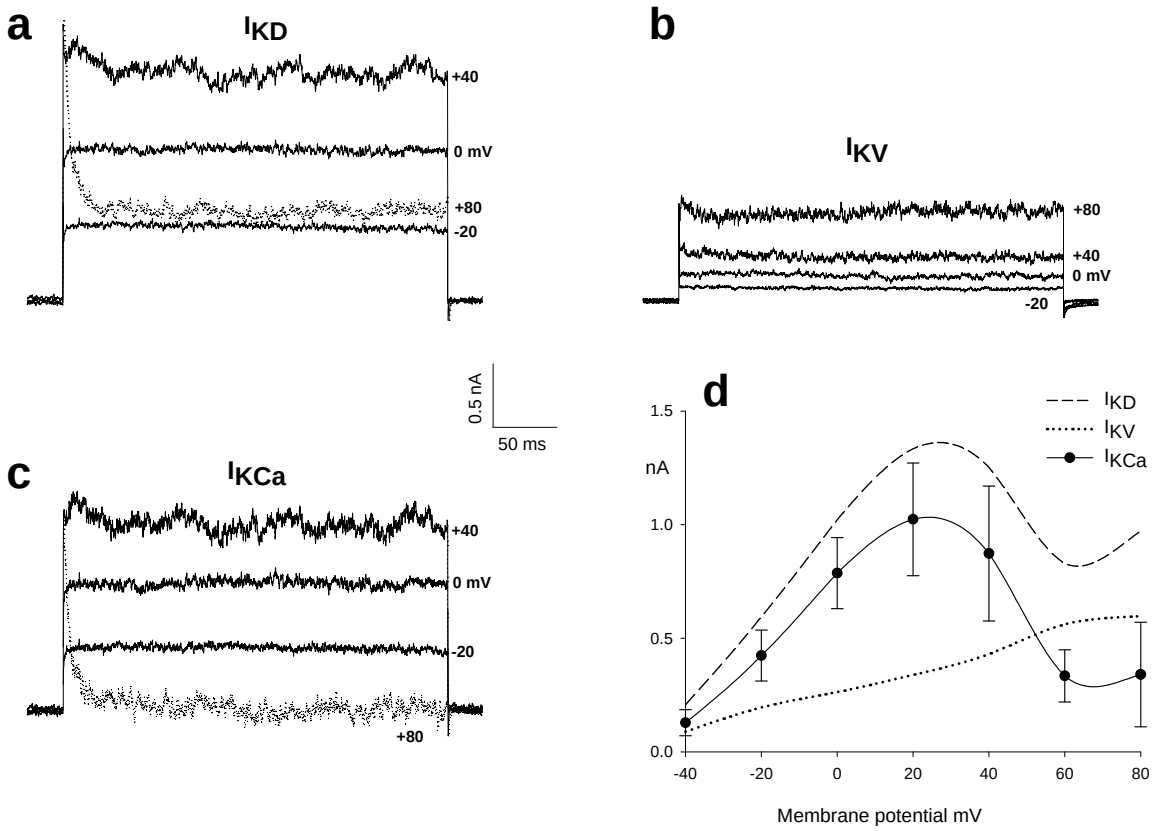

Fig. 28. Dissection of the currents building up I_{KD}. (**a-c**) Fast application of 200µM Cd^{2+} to the hair cell in control saline (**a**) reveals the I_{KV} current component (**b**). The difference current (**a – b**) dissects the calcium-dependent current fraction, I_{KCa}, at the different command levels (**c**). Tracings in a and,b are recorded from the same cell held at -40 mV throughout. The number of tracings presented is reduced for clarity. (**d**) Mean I-V relationship for I_{KCa} isolated in five hair cells. The corresponding I-V curves for I_{KD} (dashed) and I_{KV} (dotted) measured in the same cell sample are illustrated for direct comparison (same data as shown in Fig. 21 c).

Steady-state inactivation curves for I_A and I_{KD}

Due to the presence of inactivation processes, the maximum values of I_A and I_{KD} depend on the holding potential. The steady-state value of the inactivation process was studied by varying the holding potential and depolarising the cell to a fixed test voltage. According to the same rationale illustrated in Fig. 26, the test pulse was applied twice, before and after a 500 ms sojourn at -40 mV (Fig. 29 a). This procedure allowed us to dissect pure I_A tracings (Fig. 29 b) by using the subtraction protocol. The steady-state inactivation curves obtained for $h_{a\infty}$ and $h_{kd\infty}$ are illustrated in Fig. 27 a,b (open circles) and show the mean values measured for each of the two currents in the studied cells (n = 6-7). Peak I_A and steady-state I_{KD} currents were normalised to their largest value; since I_{KD} did not completely inactivate (no significant differences were measured between the delayed current amplitudes evoked starting from -40 or -30 mV holding potential), the $h_{kd\infty}$ curve reflects the presence of a consistent current available at -40 mV. The continuous line through I_A data points (Fig. 27 a, open circles) depicts a normalised Boltzmann-type equation with Vc = -70.2, V_S = 9.21 mV. The corresponding equation for $h_{kd\infty}$ *is* $h_{kd\infty} = 0.64 \cdot \left[1 + \exp\left(\left(V + 83.2\right)/7.57\right)\right]^{-1} + 0.36$ (fitted in Fig. 27 b to open circles), which indicates that 64% of the current could be inactivated at steady state in a voltage dependent manner according to a Boltzmann-type equation with Vc = -83.2, V_S = 7.57 mV.

Cell subpopulations

Analysis of the magnitude and kinetic properties of the three dissected components of outward currents, I_A, I_{KV} and I_{KCa}, did not display any consistent correlation with the cell shape or cross-correlation among them in different cells, so that it was not possible to group the N cells here studied into subpopulations, based on the differential properties of the K currents.

Currents evoked by sinusoidal voltage commands

Receptor potentials recorded from bullfrog saccular hair cells during direct mechanical stimulation of their hair bundle with a triangular wave (back and forth) produced slightly asymmetrical sinusoidal membrane potential changes from the resting potential (-58 mV in those experiments), following the displacement of the hair bundle tip. As the amplitude of the stimulation increased, the response saturated abruptly on bending the hair bundle in the inhibitory direction but not on flexing in the excitatory direction, during which graded potentials occasionally larger than 15 mV were elicited

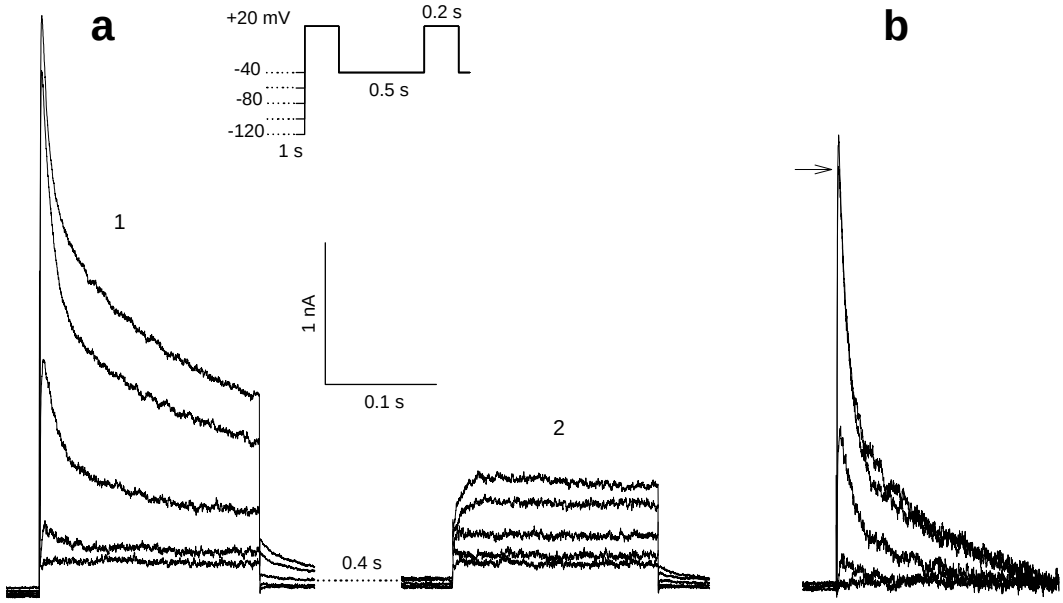

Fig. 29. (**a**) Measurement of steady-state inactivation. 1,2 illustrate currents evoked by pairs of pulses to +20 mV, separated by 0.5 s at –40 mV (to fully inactivate I_A), following 1 s conditioning in the -40/-120 mV voltage range. Both IA and I_{KD} contribute to tracings in (1), whereas the sole I_{KD} contributes to tracings in (2). The same subtraction procedure, as illustrated in Fig. 26 a, isolates the pure I_A family shown in (**b**). Arrow in (**b**) indicates, as a reference, the peak amplitude of the I_A evoked after conditioning at -100 mV.

(Hudspeth and Corey, 1977). Similar large transient depolarisations, which followed the mechanical stereociliary displacement, were recorded in vestibular hair cells of the chick: their amplitude was 24 mV at -43 mV holding potential and 30 mV at -70 mV holding potential (Ohmori, 1985). We mimicked the receptor potential time course by driving the hair cell membrane potential with a sinusoidal waveform that fluctuated from -70 to -10 mV, to simulate the excitatory/inhibitory deflections of the hair bundle, or from -40 to -10 mV range to simulate the excitatory effects only (Fig. 30). The currents evoked during the sinusoidal voltage shifts exhibited clear-cut asymmetries related to voltage and time. Currents were activated and deactivated by membrane potential according to the curves shown in Fig. 27; a first clear-cut asymmetry is evident for potentials more negative than -50 mV, where only passive currents are present. Additionally, hysteresis is apparent in comparing the rising and falling phases of the evoked current: the hyperpolarising portion of the command effectively removed I_A inactivation, causing an initial excess in outward current due to I_A activation, that appears as a shoulder in the current profile during the depolarising phase of the cycle [Fig. 30 a(a)]. The excess of total outward charge evoked at membrane potential levels positive to -50 mV during the depolarising vs. repolarising phase of the command was +22% (hysteresis index; h.i. = 1.22) during the first cycle of Fig. 30 a. Conversely, when membrane potential fluctuated within the -40/-10 mV voltage range, active currents operated during the whole cycle and the on-off phases became virtually symmetrical; furthermore, I_A was inactivated all over, and no hysteresis was evident in the current time course [Fig. 30 a(b); h.i.= 1.03]. These effects, observed during the 1 Hz cycle (Fig. 30 a), were qualitatively still discernible at 0.1 Hz (Fig. 30 b). Here the voltage range was from –80 to –20 mV, and the response to hyperpolarisation was more flattened, suggesting that cell input conductance further decreased below –70 mV. Furthermore, hysteresis was less evident, because the very slow depolarisation rate produced a slow I_A activation, effectively counteracted by concomitant inactivation, and the resulting shoulder in the rising phase of the current response was markedly reduced. It will be noted that the maximal value of outward current was similar at the positive peak of both responses [Fig. 30 b(a,b)], confirming that at this level I_A was inactivated in both cases and that the delayed current was the only flowing current. Also at 0.1 Hz the response became symmetrical and lost any hysteresis when the command voltage fluctuated in a range where active currents operate and IA is virtually inactivated [-50 to –20 mV, Fig. 30 b(b)]. The value of the hysteresis index during -70/-10 mV voltage cycles at 0.1 Hz was in the 1.15 - 1.19 range (n = 5); the corresponding values at 1 Hz ranged 1.22 – 2.43 (n = 6).

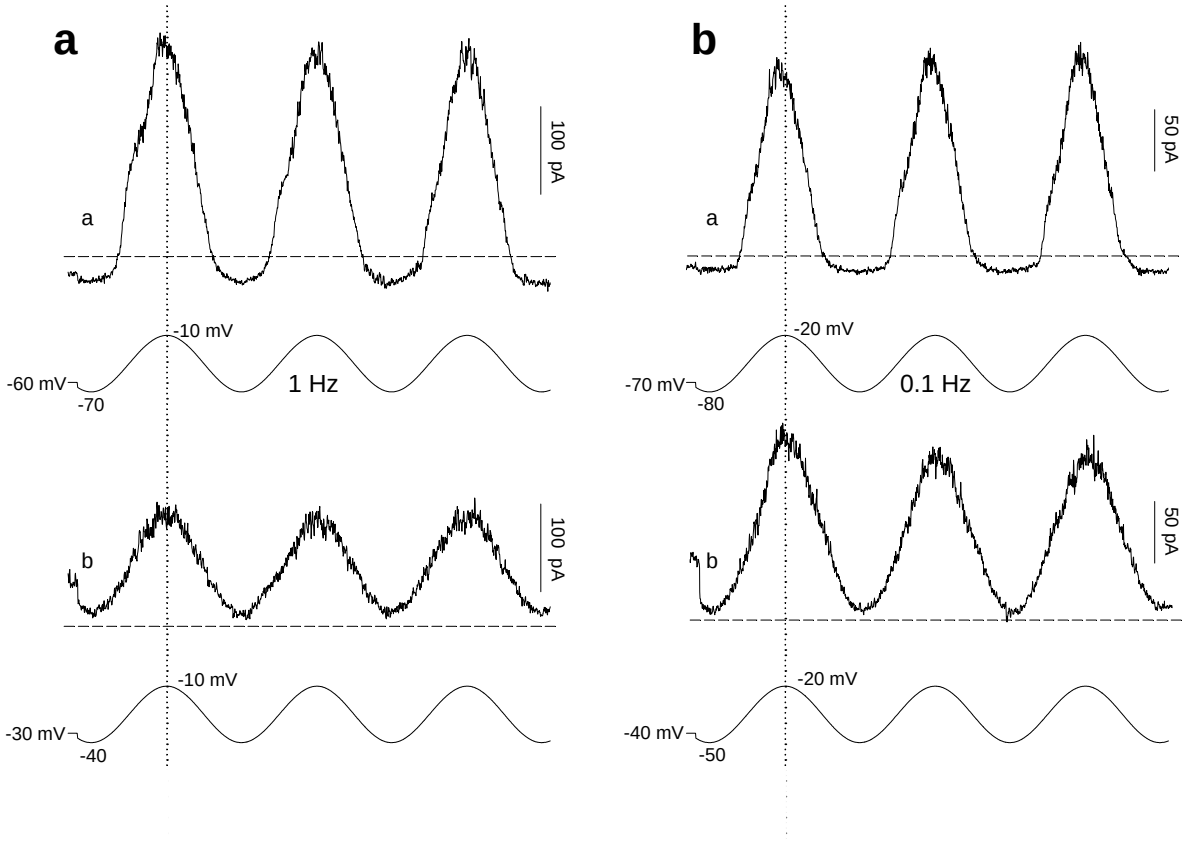

Fig. 30. Currents elicited by sinusoidal voltage commands mimicking the effects of a receptor potential generated by bidirectional (excitatory-inhibitory, **a**) or unidirectional (excitatory, **b**) hair bundle movements. (**a**) The same cell was subjected to a sinusoidal voltage command oscillating at 1 Hz from –70 mV to -10 mV (**a**) or from –40 mV to -10 mV (**b**). (**b**) Sinusoidal voltage command oscillating at 0.1 Hz from –80 to -20 mV (**a**) or from –50 to -20 mV (**b**). Dashed lines show zero-current level. Dotted vertical lines are centred at the positive peak of the voltage command.

The mean hysteresis index was 1.03 ± 0.03 during the -40/-10 mV cycles in either cell sample. It will be noted that the excitatory phase of the voltage command activates the inward calcium current, so that the true unbalance between the on- and off-phase outward charge might be partly masked by inward Ca^{2+} current and be actually larger than reported. Hysteresis was exhibited even during -70/-40 mV voltage cycles (minimal I_{Ca} activation; slight IA activation – Fig. 27 a) and when calcium movements were blocked by external Cd^{2+}, leaving exclusively the I_A and the fraction of I_{KD} activatable by the voltage excursions alone. These results indicate that IA participates in shaping the hair cell response not only when evoked by the abrupt voltage steps used in the voltage-clamp experiments, but also under conditions that more closely approach the physiological mode of hair cell activation.

Comments on voltage-dependent potassium currents

The present findings indicate that the fast transient current I_A and the delayed current components that build the I_{KD} represent separate systems and that they coexist in the hair cell of the frog semicircular canals, possibly with different physiological roles. The kinetic properties of the two currents proved useful in defining a simple voltage protocol to dissect the two components over a wide voltage range. The central observations were that inactivation removal exhibits a slow kinetic component, in addition to the well known fast recovery of I_A, and that partial inactivation, with slow onset and recovery kinetics, affects I_{KD} as well. If the latter aspect is not taken into account, the fact that I_{KD} may vary in amplitude, according to its time- and voltage-dependent inactivation status, complicates the usual procedure of I_A dissection. The current subtraction procedure works well in other systems that do not exhibit any I_{KD} inactivation (Belluzzi et al., 1985; Connors and Stevens, 1971). Here we show that it can be successfully applied also to the hair cell, provided that the inactivation mechanism of the slow current is considered. Previous attempts at separating the two current families have relied on voltage protocols similar to those adopted here, but which did not contemplate any I_{KD} inactivation process (Norris et al., 1992), or by means of pharmacological treatments such as application of 4AP (Masetto et al., 1994), a drug that is not selective for IA and potentially blocks other potassium currents as well. Here, almost pure I_A and I_{KD} current tracings are isolated by a simple subtraction manoeuvre.

Results from our experiments indicate that the two current types should be considered as completely independent entities and coexist in each hair cell. Qualitatively, the I_A activates according to first-order kinetics, rapidly and completely inactivates to zero, its

steady-state inactivation curve is centred about to the zero-current (i.e. resting) membrane potential, the inactivation-activation curves are sufficiently well separated apart to narrow down and virtually eliminate the related 'window current' (thus irrelevant in controlling the resting status). I_{KD} is a persistent current that only marginally inactivates; its activation-deactivation is fast. I_{KD} actually represents a compound current, arising from the mix of I_{KV} plus I_{KCa} (the calcium-dependent fraction sustains some 60-70% of the whole delayed current). However, they are not separately activatable under physiological conditions so that their mix operates as a single functional entity. The only exception to this general behaviour is represented by the rapid vanishing of I_{KCa}, but not I_{KV}, at very positive command potentials (>+40 mV), which is likely due to rapid waning of Ca^{2+} influx and generates in many cells a decline in the I-V curve for I_{KD} at potentials in that region.

Quantitatively, many parameters of K^+ currents, such as the I_A current decay time course, the I_{KD} amplitude and time course, displayed a large variability in the present experiments. This might be related to the intrinsic heterogeneity of hair cells, fished out from different localisation in the crista ampullaris (Masetto et al., 1994; Russo et al., 2007), or from the variability among different animal groups; alternatively, it might reflect a biased sampling due to the cell dissociation procedures. Analysis of the magnitude and kinetic parameters of the K^+ current components in the various cells of our sample did not pinpoint any cross-correlation, or correlation with the shapes of the cell, that could permit to group them into functional subpopulations. In general, much of the variability is reduced if analysis is limited to the restricted voltage range of physiological interest, and in spite of variability a number of principles and properties of excitability have been characterised and might be more generally applicable.

Our biophysical analysis has explored a wide membrane potential range, to define the general, basic properties of current activation, deactivation and inactivation. This range is much larger than that physiologically involved in normal cell behaviour. The steady level and physiological migrations of the membrane potential in native hair cells of semicircular canals are unknown; similarly unknown are the hyperpolarising/depolarising effects of the physiological stimuli during normal cell activity.

The data here reported suggest some constraints on a number of relevant biophysical parameters. The zero current membrane potential can be considered close to the cell membrane potential of the "silent" hair cell, i.e. in the absence of active ionic conductances and receptor current flow. This level is about -70 mV in our experiments, and might represent the most negative membrane potential level attainable by the isolated

cell, considering that, in spite of a Nernstian equilibrium potential for potassium ion estimated to -96 mV, most pure potassium channels are closed at -70 mV. A second relevant voltage level is the activation potential of the voltage-dependent calcium current involved in sustaining quantal release at the cytoneural junction (Robertson and Paki, 2002); previous observations have estimated this potential in the range -50/-40 mV (Martini et al., 2000). This is a membrane potential value compatible with the cell passive properties and the depolarising current provided by the average fraction of transduction channels that are open in the native cell at rest (Kennedy et al., 2003; Kros et al., 1992; Zeddies and Siegel, 2004); this would explain the significant intensity of quantal release at rest (Rossi et al., 1994). An additional parameter is represented by the receptor current equilibrium potential, evaluated at about zero mV. The hair cell membrane potential is thus expected to fluctuate from a 'resting' status close to -40 mV, sustained by a maintained receptor current flowing through the transduction channels open at rest, towards -70 mV, when these channels are closed by the inhibitory deflection of the cupula, or towards a more positive voltage level (never exceeding zero mV) after deflection of the sensory hair bundle and activation of additional transduction channels, during the excitatory movements of the cupula. The calculated variation of membrane potential due to mechanical excitation of type II hair cells was estimated to attain a span of 40 mV (Soto et al., 2002).

The distinct potassium currents activated during these membrane potential shifts have different properties, but their roles may be complementary. The delayed potassium current of the basolateral membrane is significantly activated at -40 mV; it activates and deactivates rapidly around this level and does not inactivate during potential changes (it requires a significant delay and a long-lasting sojourn at any new membrane potential level to modify its steady-state inactivation status); it is efficiently driven and faithfully follows the voltage excursions and this way it counteracts the depolarising action of the receptor current; its calcium-dependent component is limited at about -20 mV, although the calcium inflow through the voltage-dependent channels is maximal at this voltage (Martini et al., 2000). Functionally, its flow is expected to be modulated by voltage fluctuations over the whole physiologically relevant range of membrane potential values (-70 to -10 mV), and to blunt the voltage shifts produced by time-varying receptor current; prolonged hyperpolarisations or depolarisations are expected to increase or reduce, respectively, the contribution of I_{KD} to overall currents. During sensory hair bundle deflections in the inhibitory direction, the contribution of I_{KD} to overall cell currents presumably is marginal, because its threshold potential is close to –40 mV and

its amplitude is relatively small. Conversely, during slow, prolonged excitations, the delayed potassium currents are likely to operate in isolation, due to the inactivation properties of I_A. In fact, the calcium-independent I_A is virtually inactivated at the membrane potential level of the resting hair cell (receptor channels partially open) and, obviously, at more depolarised potentials. However, in the membrane potential range below –40 mV, I_A inactivation is very effectively removed. The I_A steady-state inactivation curve is very steep and is centred close to the cell membrane potential corresponding to receptor current flow cessation; moreover, inactivation removal is fast (a time constant of about 20 ms), so that a brief hyperpolarisation is sufficient to provide the cell with a significant amount of g_A, capable of generating remarkable I_A intensities upon subsequent depolarisation, even in the voltage range in which small depolarisations produce mild I_{KD} flow. Thus, I_A flow and kinetics are relevant over the whole cycle of deflections of the hair cell sensory bundle both in the excitatory and inhibitory directions.

The native hair cell is exposed in the crista ampullaris to the central control via efferent systems (see for a review: Fuchs, 1996). In particular, nicotinic inhibitory efferent fibres impinge on hair cells in the frog labyrinth; their activation results in cell hyperpolarisation (Housley et al., 1990) and drastic decrease in quantal secretion at the cyto-neural junction, even during the excitatory phase of sinusoidal stimulation (Rossi et al., 1980). The presence of nicotinic efferent inhibition of the afferent discharge has been recently confirmed in turtle posterior crista (Holt et al., 2006). As a result of hyperpolarisation from efferent fibre activation, the range of sensory modulation over which I_A may physiologically recover from inactivation would actually extend more widely than envisaged here for the dissociated cell. The inhibitory action of the efferent system can produce complete block of mEPSP and spike discharge, even during strong excitatory stimulation (Rossi et al., 1980); its effect is therefore more powerful than that of maximal inhibitory hair bundle deflection in the absence of efferent control (which never produces complete blockade of mEPSP emission). This suggests that the conductances activated by the efferent system produce outward currents sufficiently large to offset any inward current that receptor channels may activate; this would probably be complemented by a larger I_A inactivation removal. The consequent increase of I_A currents would thus strengthen the repolarising power of the hair cell during stimulation thereby further reducing transmitter release at the cyto-neural junction.

In summary, the delayed potassium current can be viewed as a current fraction continuously modulated by voltage, whose magnitude only partially changes with time, following prolonged depolarisations or hyperpolarisations. It is expected to mildly

counteract the receptor current fluctuations on a short time scale (fast activation-deactivation over tens of ms) and to slowly boost it on a long time scale (inactivation and recovery cycle, over several seconds). The I_A contribution, on the contrary, is always transient. The recent history of membrane potential sets the magnitude of its contribution – by determining its degree of inactivation from 0 to 100%. I_A has a rapid onset and can be very intense; this way it systematically counteracts the receptor current, but its efficacy depends at any moment on the prevailing membrane potential: sudden activation of transduction current in a well polarised cell will be counteracted by I_A much more efficiently than in an active, partially depolarised hair cell. In this perspective, I_A might be systematically involved during the normal excitability cycle of the cell. A 'buffering capacity' of IA has been envisaged in previous studies, as a stabilizer of the membrane potential (Housley et al., 1989) or as a hyperpolarising buffer to oppose sudden depolarisations of the hair cell (Norris et al., 1992). This suggestion is now more precisely specified and circumstantiated by direct evidence based on a better understanding of the current kinetic mechanism.

Afferent synaptic transmission

In the frog labyrinth, synaptic transmission between hair cells and afferent nerve fibres at the cytoneural junction is chemically mediated. Subthreshold potentials, mEPSPs, and spikes can be recorded from single fibres of the posterior nerve. At rest, mEPSP frequencies vary among the different units (10-300/s) though there is a predominance of units displaying high resting rates (> 100/s); conversely, spike rates are rather low (0-20/s). Since the first observations, subthreshold potentials were recognized as EPSPs owing to the wide variability in their amplitudes (Rossi et al., 1977; 1980). However, there is no evidence at this synapse that a multiquantal mechanism of release (i.e. synchronous and correlated fusion of several vesicles to release their content) is operating, so that the subthreshold potentials could well correspond to asynchronous release of single quanta, i.e. each of them might be a true miniature EPSP (mEPSP).

In the majority of the units, the high frequency of synaptic events produces extensive overlapping of the individual mEPSPs, making it difficult to estimate individual peak amplitudes. We have previously estimated mEPSP amplitude and rate of occurrence at the posterior canal cytoneural junction, at rest and during mechanical stimulation, by treating the signal originating from the summation of the events as shot noise (Rossi et al., 1989) mEPSP amplitude remains relatively constant at rest and during rotation, suggesting the uniquantal nature of the events. If each mEPSP were generated by a s ingle quantum of transmitter, then noise

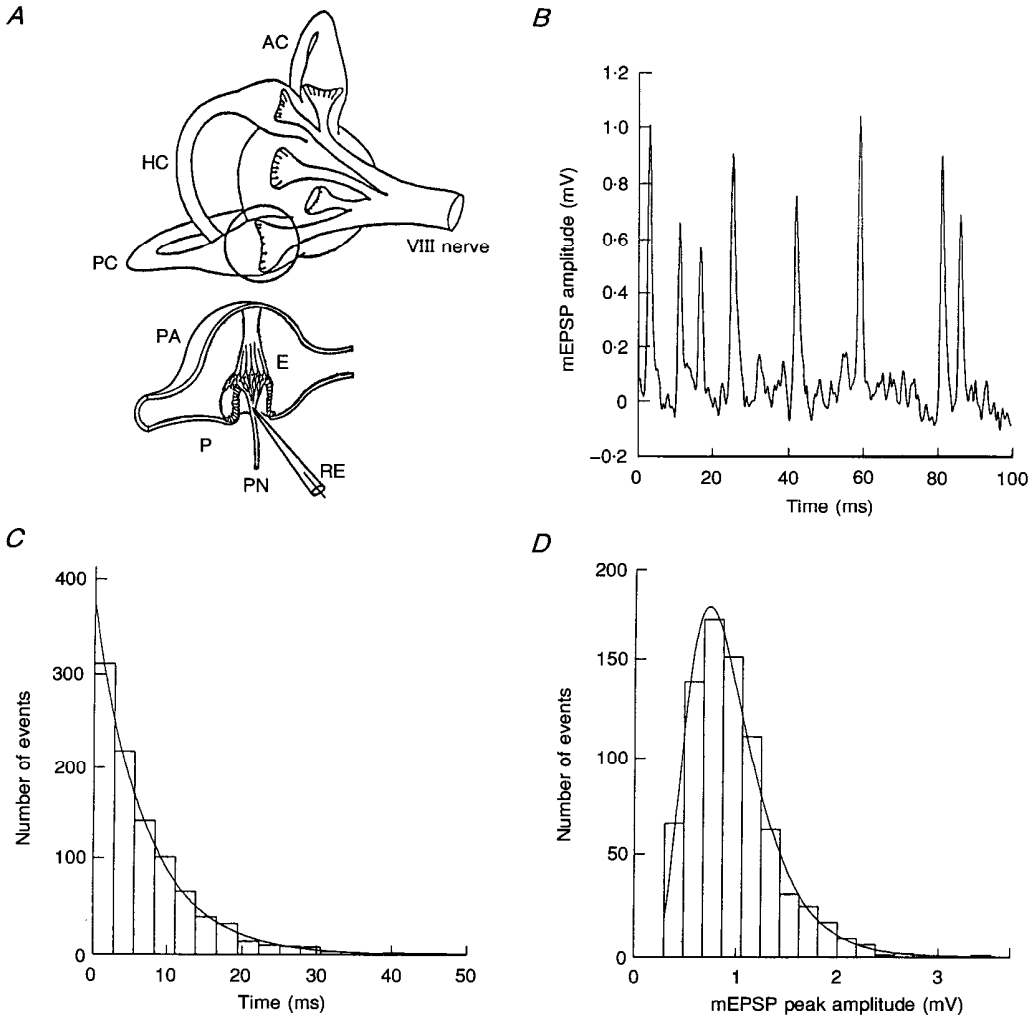

Fig. 31. Analysis of a unit with low resting activity. **A**, schematic drawings of the isolated frog labyrinth (top) and the transverse section of the posterior ampulla (bottom). The section corresponds to the encircled portion of the posterior canal. PC, posterior canal; HC, horizontal canal; AC, anterior canal; PA, posterior ampulla; P, perilymph; E, endolymph; PN, posterior nerve; RE, recording electrode. **B** shows a typical recording taken from a unit with a low mEPSP resting rate (90/s). Note the variable peak amplitudes and that the events do not overlap. **C** illustrates the time-interval histogram (n= 956) between successive events taken from the unit shown in *B* and the fit with a single exponential *(P* > 0.75, goodness-of-fit test). **D** shows the peak amplitude histogram (n = 792) from the same unit and the fit with a log normal distribution function *(P* > 0.50).

analysis during sustained intense synaptic activity could yield information about the size of the readily releasable pool of transmitter quanta, as well as the time constants of quantal turnover and synaptic vesicle recycling. However, the uniquantal nature of these events is far from be definitively proven. It is therefore important to preliminarily clarify whether the large sub-threshold potentials arise from giant mEPSPs, multiquantal events, or the summation of randomly occurring independent unitary events of comparable size.

Quantal analysis

1) Analytical fit to mEPSP waveform

In order to quantitatively evaluate changes in mEPSP size and waveform, a multistage AC-trigger routine was used to detect the events. The rising phase of the event was discriminated from sharp fluctuations in baseline noise by the detection of three successive samples with slopes greater than an empirically set value. The mEPSPs were aligned by saving a record on disk for each event, which comprised four pretrigger samples (0.8 ms) and sixteen to thirty-six samples (3.2-7.2 ms) after the trigger. Twenty-five to one hundred records containing isolated events (with the saved portion of their time course free of overlap to other events) were selected and averaged. The average mEPSP waveform was fitted using a modified γ-distribution function, w(t):

$$\text{mEPSP} = h\,w(t) = h\,(\beta t)^{\gamma} \exp(-\beta t) I\,\Gamma(\gamma + 1),$$

where h is a size factor (height, mV), β (s^{-1}) defines the time scale, Γ indicates the Euler γ-function, i.e.

$$\Gamma(\gamma + 1) = \int_0^{\infty} \beta^{\gamma+1} t^{\gamma} \exp(-\beta t) dt,$$

and γ determines the shape of w(t), from a single exponential (γ= 0) to a near-Gaussian shape for γ> 10. The time to peak is τ=γ/β, and the peak amplitude is:

$$V_p = \text{hw}(\tau) = h\gamma^{\gamma} \exp(-\gamma)/\Gamma(\gamma + 1).$$

Note that by this relation, V_p can be converted to h and vice versa, and that such conversion just requires the knowledge of γ and is independent of the time scale, β. However, this procedure could be performed only on recordings in which the mEPSP rate did not exceed 100 s^{-1}.

2) Peak vs. area relation for mEPSPs and mEPSP waveform

In the units with low mEPSP rate a linear relation was observed between peak amplitude and time integral of the mEPSPs. Thus the ratio between area and peak amplitude constitutes a meaningful and reasonably measurement of 'mEPSP equivalent duration' (Fig. 32).

3) Wiener filtering

When mEPSP rates exceeded 100 s^{-1}, postsynaptic potential waveform and size analysis were performed by examining the recordings after Wiener filtering. This procedure was also performed on traces with rates <100 s^{-1} and the results compared with direct measurements. The single-event waveform, necessary for building the Wiener filter, was deduced from autoregressive fit to the autocorrelation of the signal. A fixed autoregressive order (five) was used for the approximated fit. From noise analysis theory, when a signal is generated by the random summation of homogeneous events, the autocorrelation of the signal has the same shape as the autocorrelation of the single event. The mEPSP waveform at the cytoneural junction is `minimum phase', as indicated from both theoretical considerations (the output of physical, causal, stable filters is minimum phase) and experimental observation (Rossi et al., 1989). Autoregressive fit to the autocorrelation yields the analytical minimum-phase approximation to the event waveform, $w_a(t)$, that was used to construct a Wiener filter, with transfer function $W^*(f)/[(vv\ (f)^2] + N)$, where W(f) is the Fourier transform of $w_a(t)$, * indicates complex conjugate, and *N* is an arbitrary constant which accounts for noise in … the recording (usually set between 1/20 and 1/10 of the signal variance). The time-domain form of the Wiener filter was computed as a 128 sample time series, and a truncated form (8 negative and 16 positive lags) was used for filtering in the time domain, as the values of the filter series were negligible outside this interval. Thus, filter-dependent transient artifacts affected only the first twenty-four samples (about 5 ms) of the filtered recordings. After Wiener filtering, the junctional recordings with overlapping events were transformed into spiking in which the location of each 'spike' indicated the occurrence of a mEPSP and the size of the spike was proportional to the amplitude of the corresponding mEPSP. To reduce high frequency noise in the filtered signal a further filtering (smoothing) was performed using a five-point bell shaped window (a Gaussian function with 0.57-sample standard deviation).

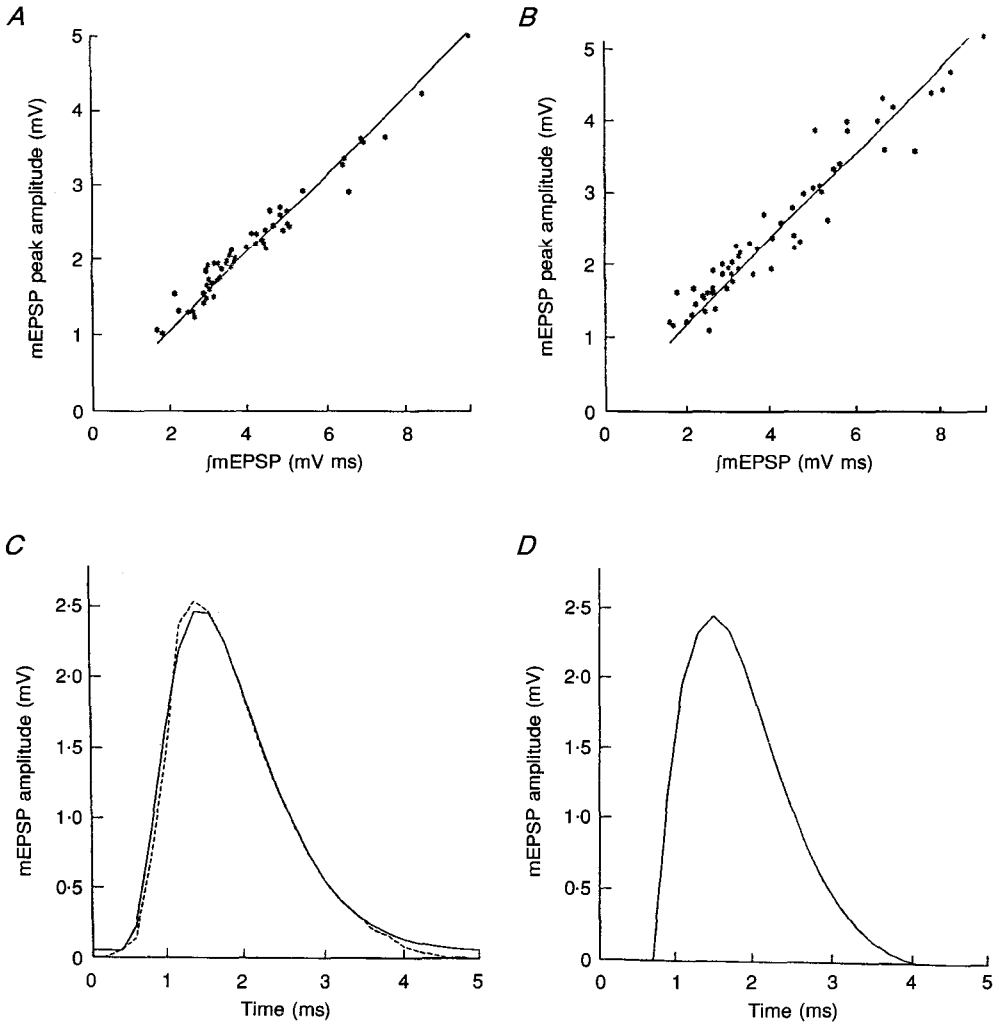

Fig. 32. Peak vs. area relation for mEPSPs and mEPSP waveform. **A** and **B** show the linear relation between mEPSP peak amplitude and the area under a mEPSP (2 different units, correlation coefficient = 0.98 and 0.96, respectively). **C ,** illustrates the analytical fit (continuous line) with a modified y-distribution function ($\gamma = 3$, $\beta = 2730$ s') to the average (dashed line) of 30 events taken at rest from a unit with low mEPSP frequency. **D** , shows the waveform obtained in the same unit from the autoregressive fit to the autocorrelation of the recording.

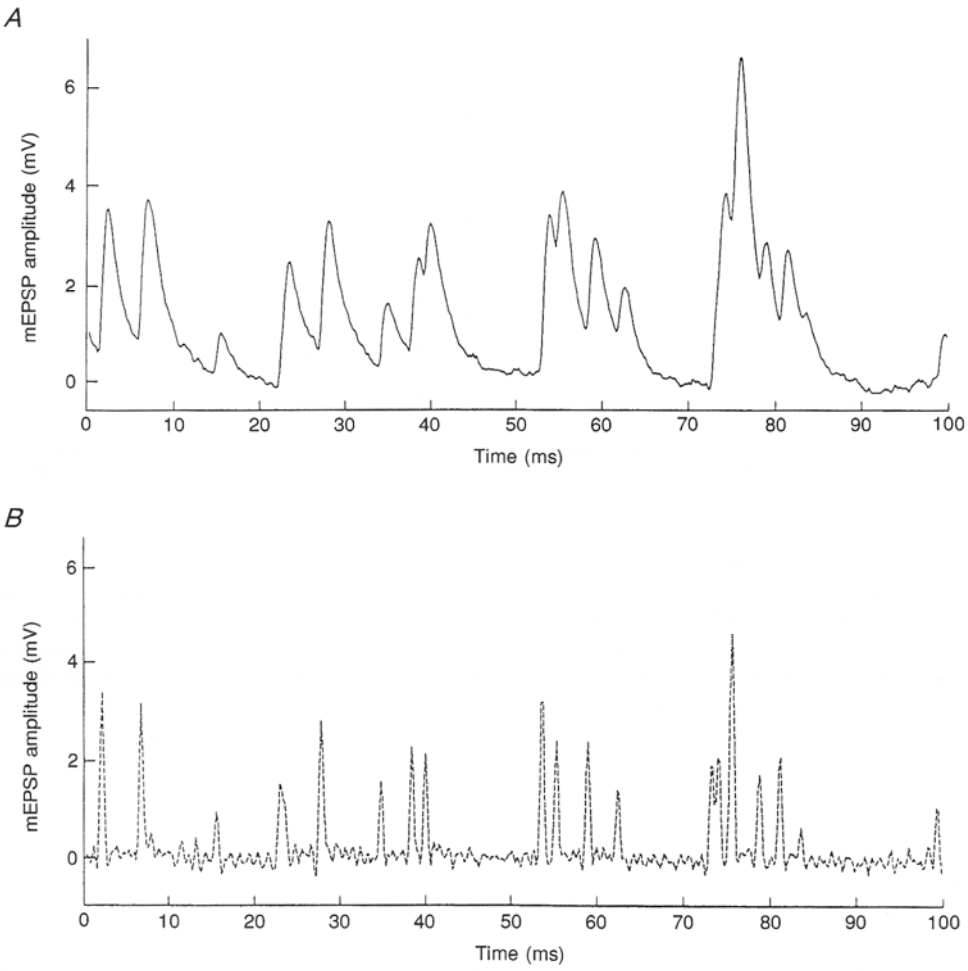

Fig. 33. The effect of the Wiener filter. **A**, shows a recording taken at rest from a unit with a high resting mean mEPSP rate (170/s). Note the extensive overlap among events. **B**, shows the same recording after Wiener filtering. In this trace the location of each `spike' indicates the occurrence of a mEPSP and the size of the spike corresponds to the amplitude of the original event.

4) mEPSP size

The peak amplitude, V_p was used to characterize mEPSP size. For non-overlapping mEPSPs, V_p could be directly measured on recordings; for averaged events fitted by γ-distribution functions, V_P was computed from the height factor, *h*, using the relation indicated above. For Wiener-filtered recordings, the heights of the sharpened, spiky mEPSPs were measured as the distance of the maximum from baseline, and the corresponding values for V_p automatically computed by correcting for the ratio between the mean peak amplitudes of twenty isolated mEPSPs on the same recording before and after Wiener filtering.

In this way it was possible to compare the mEPSP size distributions obtained from measurements of the peak amplitude of isolated mEPSPs with those obtained in the same records after Wiener filtering, and with the height of the averaged mEPSP. Histograms of mEPSP peak amplitude values and time intervals were obtained from the Wiener filtered recordings and fitted by maximum-likelihood procedures using log normal or exponential distributions, respectively. Goodness-of-fit tests were performed. For amplitude histograms, fits with other distribution functions, such as Gaussian and γ-distributions, were also considered. The adequacy of single log normal (or normal) functions in fitting size distributions, and of single exponential functions in fitting time-interval distributions, were examined using the principle of extra sum of squares: the improvements in the fits, obtained by using the sum of two or more functions (several log normal or normal functions with arbitrary areas and additive mean and variance, for sizes; or several exponentials with arbitrary weights for intervals) rather than a single function, were evaluated from the variance ratio $F = ((SS1 - SS2)/(d..f. 1 - d.f. 2))/(SS2/d.f. 2)$ where d.f. 1 and SS1, or d.f. 2 and SS2, indicate the degrees of freedom and sums of normalized square errors ((observed – expected)^2/(expected) for each class), using either the simpler or the more complex fit, respectively. The significance of the improvement was read on F-statistic tables. Histograms from the same units under different experimental conditions were compared by applying the non-parametric Kolmogorov-Smirnov (KS) test to cumulative histogram plots.

Peak values were measured directly after Wiener filtering *(A)* or on the original traces *(B)* from a single unit displaying a high mean resting mEPSP rate (196/s as estimated from the unfiltered record *vs.* 222/s from the filtered record). Note the highly skewed distribution in *B,* as opposed to the narrower and less skewed distribution obtained after filtering *(A)*. The histogram in *A* is well fitted by a single log normal function. The distribution in *B* can also be fitted by a single log normal function, but an equally good fit is obtained by the sum (continuous line) of several log normal functions (dashed lines): the first and tallest one has the

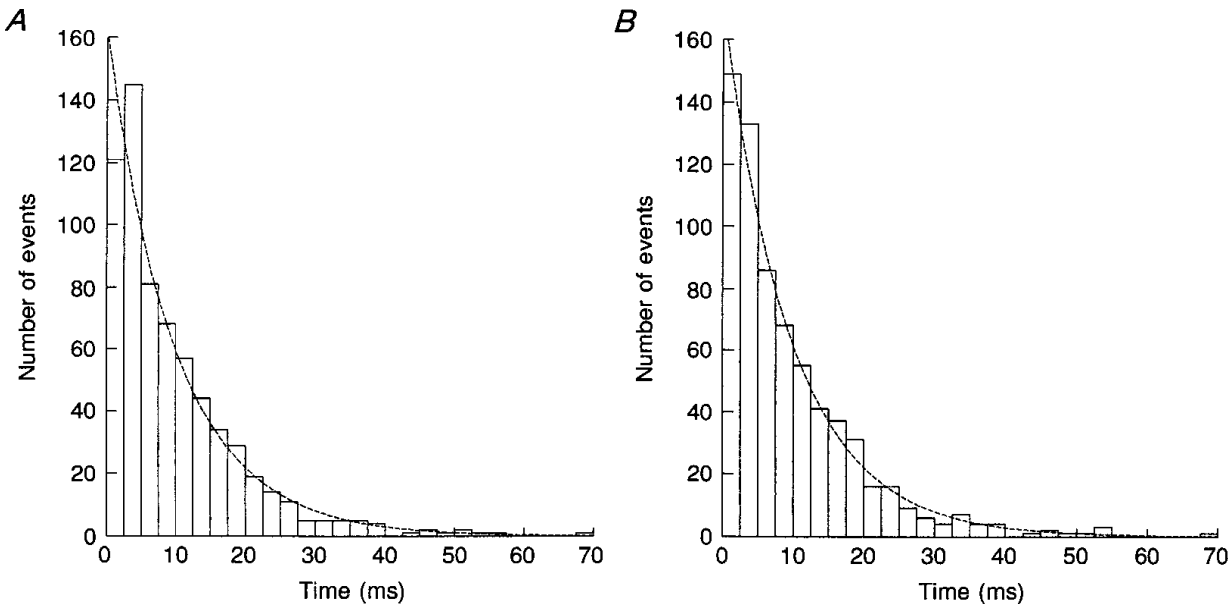

Fig. 34. Time intervals were measured before *(***A,** n = 656) and after *(***B**, n = 675) Wiener filtering, on the same record from a unit with rather a low mean mEPSP rate (100/s), where a direct evaluation of time intervals between events was still possible. Both distributions are fitted by a single exponential function; however, the fit is remarkably improved, particularly for short intervals, after filtering *(*$P > 0.10$ in *A* vs. $P > 0.75$ in *B,* goodness-of-fit test).

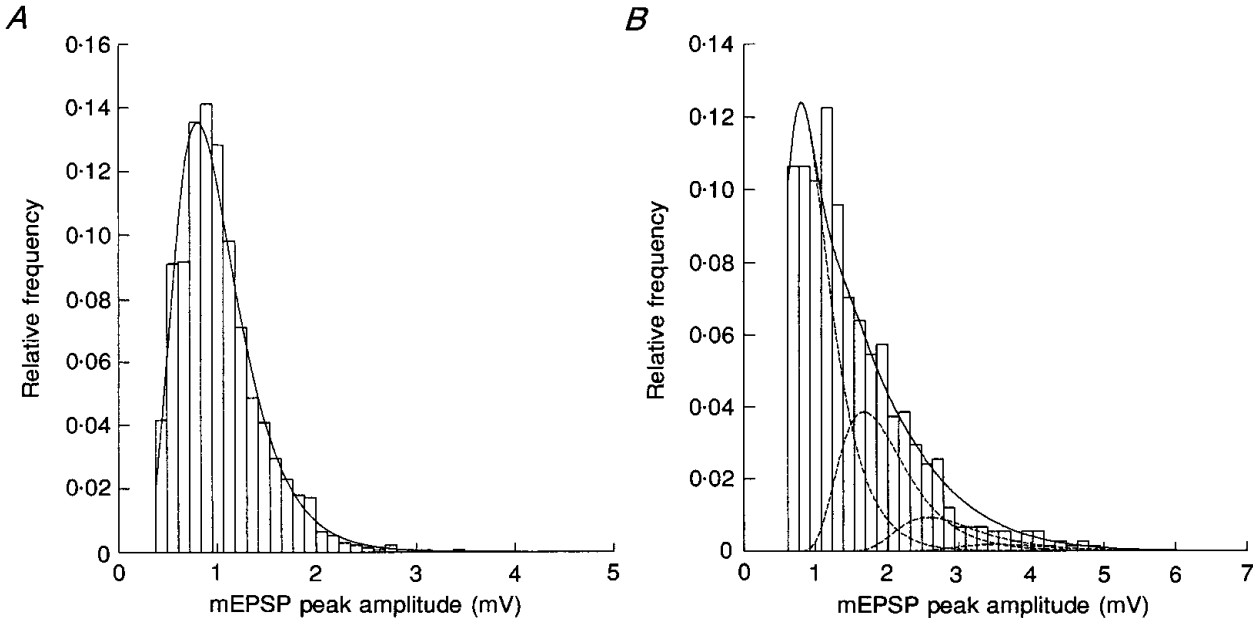

Fig. 35. Peak values were measured directly after Wiener filtering *(***A***)* or on the original traces *(***B***)* from a single unit displaying a high mean resting mEPSP rate (196/s as estimated from the unfiltered record *vs.* 222/s from the filtered record). Note the highly skewed distribution in *B,* as opposed to the narrower and less skewed distribution obtained after filtering *(***A***)*. The histogram in *A* is well fitted by a single log normal function. The distribution in *B* can also be fitted by a single log normal function, but an equally good fit is obtained by the sum (continuous line) of several log normal functions (dashed lines): the first and tallest one has the same parameters which provide best fit to the distribution observed after Wiener filtering *(μ_{log},* -0.0642; o^{-}_{log}, 0.3964, in *A),* whereas the others have double, triple (and so on) mean and variance. The areas enclosed by the peaks are proportional to the probability of occurrence of 1, 2, 3 (and so on) events within a brief time interval of duration, *T,* according to Poisson statistics; the mean number of events (in) occurring during such an interval *T* is the only free parameter in the fit, and its best-fitting value, m = 0.88, indicates that effective summation of events ensues when they occur within a time interval *T*= m/mean rate 4 ms.

same parameters which provide best fit to the distribution observed after Wiener filtering *(p_{log}*, -0.0642; σ_{log}, 0.3964, in *A),* whereas the others have double, triple (and so on) mean and variance. The areas enclosed by the peaks are proportional to the probability of occurrence of 1, 2, 3 (and so on) events within a brief time interval of duration, *T,* according to Poisson statistics; the mean number of events (in) occurring during such an interval *T* is the only free parameter in the fit, and its best-fitting value, m = 0.88, indicates that effective summation of events ensues when they occur within a time interval *T*= m/mean rate 4 ms.The histograms of mEPSP peak amplitude at rest, in units with low resting rates of release, are continuous, unimodal, and smoothly skewed towards high values (thus ruling out a significant incidence of giant events), and resemble peak amplitude histograms of unitary events at other synapses. Moreover, the size histograms are well fitted by log normal distribution functions like the miniature endplate potentials (mEPPs) at the frog neuromuscular junction. This suggests that such potentials are unitary, i.e. produced by the release of a single quantum of transmitter, and can be called mEPSPs. The exponential distribution of time intervals between successive mEPSPs supports this interpretation and the idea that single quanta are released at random, independently of one another.

When the recordings were sharpened by inverse filtering, using a Wiener filter computed from the minimum-phase waveform derived from the autocovariance of the signal, the histograms of peak amplitudes lost most of their skewness and became very similar to those obtained with low release rates. This finding supports the idea that we are dealing with unitary events, mEPSPs. After Wiener filtering, time-interval histograms at rest were well fitted by single exponentials even with rather high release rates, suggesting random occurrence of mEPSPs.

Microgravity

Information on head position and movement is elaborated in the central nervous system by integrating sensory information coming from labyrinth organs with visual and somesthesic information. Most of the vestibular information is directly or indirectly affected by gravity; thus changes in gravity conditions are bound to interfere with sensation, perception and central elaboration of such information. Many common and evident disturbances of this system arise during central processing and integration of sensory information, due to incoherence between visual and gravity (vestibular, neck muscle tension, etc.) sensory inputs. However, primary alterations of vestibular function are expected to occur, as altered gravity is likely to produce significant and measurable interference with transduction processes at the vestibular organs and with neural

encoding of the static and dynamic stimuli the head is exposed to.

A series of structural and functional alterations have been reported to occur in several cellular systems following exposure to conditions of altered gravity. However, up to now functional data on vestibular organs are not available.

The two main aspects in evaluating the effect of gravity on vestibular function are (i) possible interference with vestibular function during exposure to altered gravity conditions and, (ii) alterations which may ensue following such exposure. In principle, both aspects would be amenable to instrumental investigation. However, it is easier and more productive to study the changes induced in the function of vestibular organs which detect linear and angular accelerations (utricle and semicircular canals) by a prolonged exposure to altered gravity conditions.

A condition of decreased gravity ("microG") can be simulated by placing the anaesthetised frog in a "random positioning machine" (RPM), which continuously changed the orientation of the animal with respect to the gravitational axis. This is considered a standard way to simulate the absence of gravity, especially to study cell culture and tissue preparations. The problems in applying the procedure to a small animal, and in particular in studying labyrinthine function, are twofold: on the one hand the frog must be anaesthetised, and anaesthesia may produce by itself specific effects both locally and in terms of cross-talk with central nervous structures; on the other hand the microG simulation procedure intrinsically implies a remarkable degree of continuous stimulation of vestibular organs, as the head is subjected to continuously changing angular accelerations around variable spatial axes. Due to this latter problem, a series of control procedures must be setup, to carefully dissect any possible effect of microgravity from effects related to the manipulation of the animal and the stimulation of the vestibular organs during the microG simulation protocol.

A delicate question regards what would be the most appropriate labyrinthine organ to perform this kind of study. At first, one would think that the sacculus (and possibly the utricle) should be the most appropriate sensors, as they are in charge of the detection of linear accelerations and the perception of the orientation of the head with respect to the gravitational axis. However, exposure to simulated microG in the RPM implies crucial differences from true absence of gravity: whereas in the absence of gravity the labyrinth is not exposed to any external linear acceleration, in the RPM machine the average linear acceleration is null along any axis in space, but the preparation – and the otolithes in the sacculus and utricle – are continually exposed to a linear acceleration with the "normal" module of 9.8 m/s^2 and a continuously varying direction. Thus, in these organs the

simulation of zerogravity is not appropriate and it is not possible to devise a control procedure that separates the stimulation in the RPM from the effect of an average null gravity. On the contrary, semicircular canals do not sense, in principle, linear accelerations; at difference with true absence of gravity, the semicircular canals are exposed, in the RPM simulation, to continuously changing angular accelerations; however, if one of the canals is positioned so that its axis coincides with the axis of rotation of the internal frame of the RPM (see Methods), then it can be exposed to exactly the same kind of stimulation in the presence of a normal gravitational field, provided that only the internal frame of the RPM is rotated, in the same way, keeping its axis still and vertical.

The possible effects of microG treatment were examined *a posteriori* by studying: 1) the alterations of the biophysical properties of calcium and potassium currents of frog labyrinthine hair cell isolated from the semicircular canals; 2) the function of the receptor epithelium at the posterior ampulla in the isolated intact labyrinth.

In particular, the secretory capability of the hair cell was evaluated by counting the elementary, quantal synaptic events recorded near the terminal of the primary afferent neuron, at rest and during mechanical rotational stimulation of the posterior canal.

The purpose of this thesis is to verify whether the kinetics of the hair cell currents as well as synaptic transmission at the cytoneural junction in the intact animal undergo significant functional changes when exposed to reduced gravity conditions.

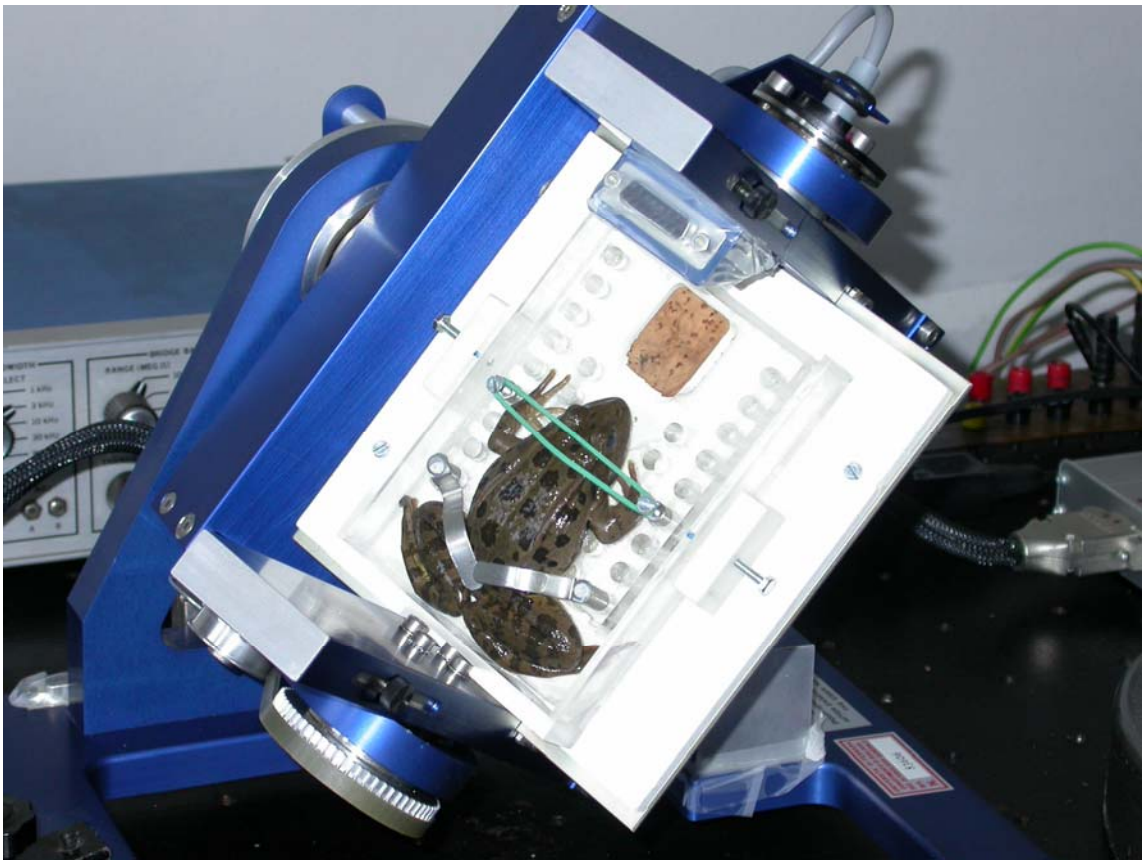

Fig. 36. The anaesthetized frog is positioned on the stage of the internal frame of the Desktop RPM (Random Positioning Machine) during a conditioning period preceding the electrophysiological experiments. The animal is maintained under conditions of simulated microG, obtained by random rotation of both RPM internal and external frames.

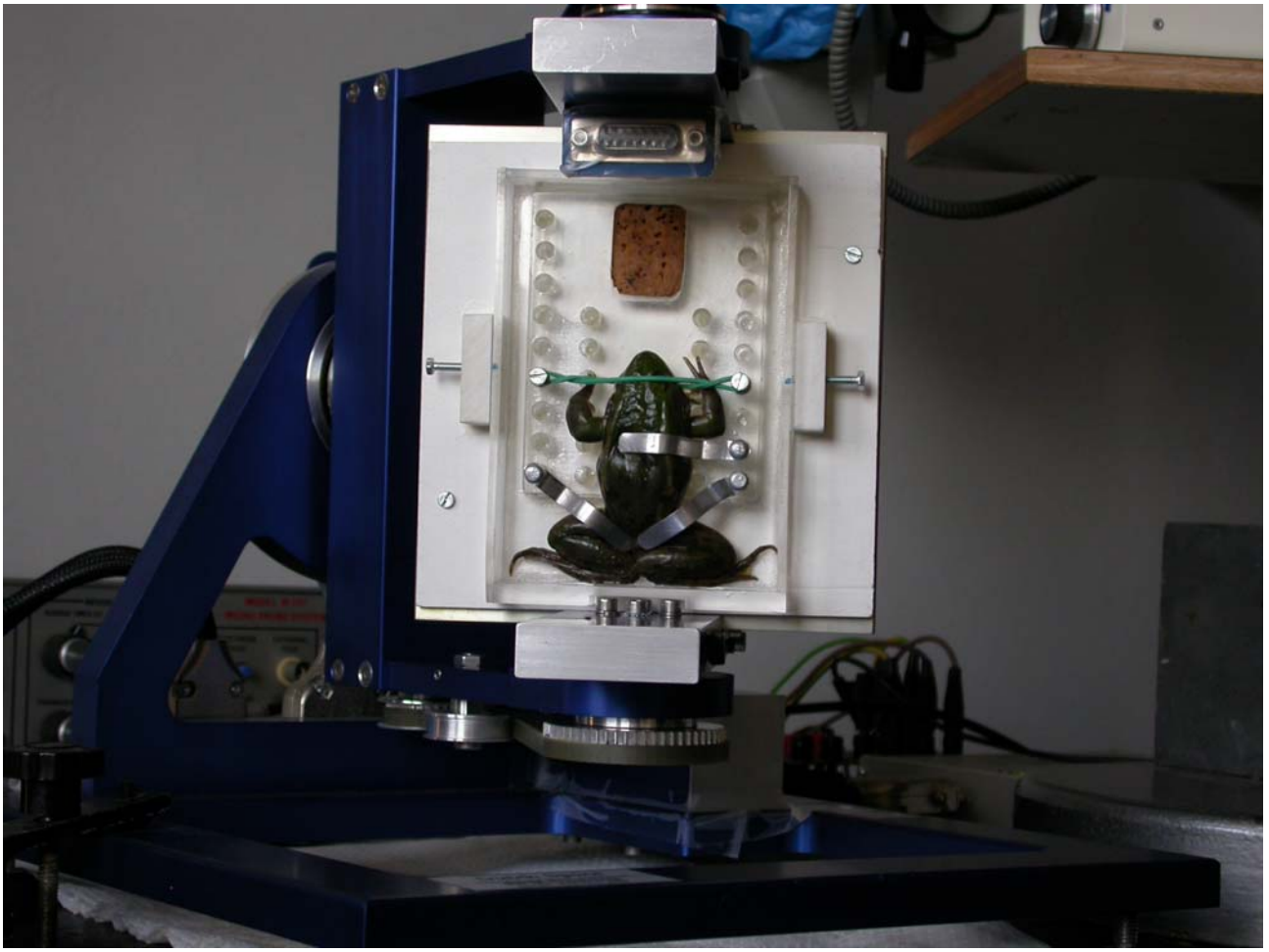

Fig. 37. The anaesthetized frog is positioned on the stage of the internal frame of the Desktop RPM (Random Positioning Machine) during a conditioning period preceding the electrophysiological experiments. The animal rotates around the vertical axis simulating Normo-gravity control conditions. Rotation velocity randomly changes so to produce the same intensity of stimulation on the posterior canal as in Microgravity

MATERIALS AND METHODS

Patch clamp experiments

The experiments were performed on wild frogs (*Rana esculenta*, 25-50 g body weight) at 20-22 °C. All procedures for animal handling and surgery were approved by the Animal Care and Use Committee of the University of Ferrara and authorized by the National Ministry of Health. Frog labyrinth preparation, stimulation and recording procedures have been described in detail previously (Martini et al., 2000; Martini et al., 2007). Briefly, the animals were anaesthetized by immersion in tricaine methane sulfonate solution (1 g/l in water; Sigma) and subsequently decapitated: immediately, to obtain control hair cells, or after 4h conditioning in the presence or absence of gravity. The head was pinned down at the bottom of the dissection chamber and submerged in a dissection solution of the following composition (in mM): 120 NaCl, 2.5 KCl, 0.5 EGTA, 5 Hepes, 3 glucose, 20 sucrose. The final pH was 7.2 and the osmolality 260 mOsmol/kg. The ampullae were isolated from both labyrinths and treated for a period of 20-30 s with subtilisin A, type VIII (50 μg/ml, Sigma); thereafter, they were transferred, in the presence trypsin inhibitor type II-S (Sigma) (final concentration 0.7 mg/ml), into the experimental chamber (500 μl volume), submerged in the standard extracellular solution (mM): 120 NaCl, 2.5 KCl , 2 $CaCl_2$, 1 $MgCl_2$, 5 glucose, 5 Tris buffer (pH 7.3); 245 mOsmol/kg. The hair cells were mechanically dissociated from the ampullae by gently scraping the epithelium with fine forceps. Some 30 min elapsed between the end of preconditioning and the start of electrophysiology.

Recordings were carried out by using the patch-clamp recording technique in the "whole-cell" configuration. Pipettes were pulled from 50 μl glass capillaries, and fire-polished to a final resistance of 3-4 MΩ. The pipette was filled with the following solution (mM): 110 KCl, 2 $MgCl_2$, 1 ATP (K salt), 0.1 GTP (Na salt), 5 EGTA-NaOH, 10 Hepes-NaOH (pH 7.2; 235 mOsmol/kg).

When calcium currents were recorded, the composition of the chamber solution was (mM): 100 NaCl, 6 CsCl, 20 TEACl, 4 $CaCl_2$, 10 HEPES, 6 glucose (pH 7.2); 260 mOsmol/kg. Pipette solution was as follows (mM): 90 CsCl, 20 TEACl, 2 $MgCl_2$, 1 ATP (K salt), 0.1 GTP (Na salt), 5 EGTA-NaOH, 10 Hepes-NaOH, (pH 7.2; 235 mOsmol/kg).

Isolated hair cells exhibited high membrane resistance (> 1 GΩ) at –70 mV. These values indicate that no major conductances, such as hyperpolarization-activated currents or current through transduction channels (possibly open at rest in the native hair cell), were

significantly active. Series resistance ranged between 8 and 22 MΩ. The cell capacitance and series resistance were electronically compensated (50-75%) before each voltage-clamp protocol was run. The uncompensated series resistance component introduced an error in the applied voltage command, which was limited to 10-12 mV when the largest currents were recorded. Leak was measured near resting potential with a 10 mV × 15 ms hyperpolarizing pulse; this leakage current was subsequently subtracted, assuming a linear behavior, in correcting current recordings off-line.

Cd^{2+} (200 μM) was used as blocker of voltage-dependent calcium channels. It was applied by rapidly (typically < 50 ms) changing the external solution by horizontally moving (with a computer-controlled stepping motor) a multi-barrelled perfusion pipette positioned in front of the recorded cell.

Cells were viewed through a TV monitor connected to a contrast enhanced video camera (T.I.L.L. Photonics, Planegg, Germany). The camera was coupled to an inverted microscope (Olympus IMT-2, Tokyo, Japan) equipped with a 40× Hoffman-modulation contrast objective. The current was recorded with a commercial patch-clamp amplifier (EPC-7, List-Electronic, Darmstadt, Germany); the command protocol and data acquisition were performed with a Digidata 1322A computer interface and a pClamp package (Version 9.0) running on a Pentium computer. The recordings, filtered at 2, 6, or 10 kHz via an eight-pole Butterworth filter, were acquired at 5, 12.5, or 40 kHz, respectively, and stored on disk. Mathematical procedures were implemented with Matlab (Version 5.3, The Math Works, Natick, MA, USA).

Voltage-dependent parameters were fitted throughout by Boltzmann equations of the form $B(V) = A \cdot \left[1 + \exp\left(-b \cdot \left(V - V_{½}\right) \cdot F/RT\right)\right]^{-1}$, where A is maximum amplitude, b is the slope coefficient and $V_{½}$ is the value of potential for which the equation has half its maximum value ($B\left(V_{½}\right) = A/2$).

The differences among various experimental conditions were examined by two-way ANOVA. When necessary, logarithmic transformation of data was performed to homogenize variances. This was necessary for current amplitudes, which markedly varied with membrane potential and generally displayed, at each value of potential, a variability among cells roughly proportional to the average value. Values of F and P are reported in the text for significance of treatment effect; contrasts between pairs of treatments were examined by Student's *t*-test; significant differences ($P < 0.05$, two tails) are reported as either absolute or percentage change with 95% confidence limits (CL95). In the figures, data are presented by pooling the results obtained from several cells under

each experimental condition. Average values and SEM are plotted for each condition.

Intracellular recordings

Electrophysiological experiments were performed on the isolated and intact frog labyrinth after exposure to the appropriate treatment: the animal was anaesthetised by immersion in tricaine methane sulfonate solution (1 g/l in water) and subsequently decapitated. The head was pinned down at the bottom of the dissection chamber and submerged in a dissection solution of the following composition (in mM): 120 NaCl, 2.5 KCl, 0.5 EGTA, 5 HEPES, 20 sucrose, 3 glucose (pH 7.2). The osmolality of the solution was 260 mOsmol/kg. The labyrinth was isolated. The posterior canal was exposed with its nerve in the right half of the frog head; then the labyrinth, protected by the remaining bone, was separated from the head and transferred and fixed to the bottom of a small Perspex chamber mounted at the centre of a turntable. The turntable assembly, adapted for electrophysiological examination of the labyrinthine function, includes a custom-made miniaturised microelectrode amplifier (0-5 kHz bandwidth) and is driven by a servo-motor controlled by a function generator. The preparation was accurately positioned so that the posterior canal lay in the plane of table rotation. Mechanical stimulation experiments were performed by subjecting the canal to sinusoidal angular velocity stimuli at 0.1 Hz, peak accelerations 12.5 deg/s^2. Intracellular recordings were obtained at rest and during rotation using glass microelectrodes (30-40 MΩ resistance), filled with 3 M KCl, inserted into the posterior nerve within about 500 μm from the synapse. The recorded potentials are transferred through low-noise sliding contacts to the oscilloscope, recorded on tape and analysed off-line. The afferent discharge recorded from single fibres of the posterior nerve was examined both in terms of spike frequency and of frequency and waveform of miniature excitatory post synaptic potentials.

RESULTS

Hair cell passive properties

Hair cells of several different morphologies have been observed in the frog crista ampullaris, and position-specific differences have been reported for some bioelectrical properties of hair cells (Masetto et al., 1994; Russo et al., 2007). In dissociated hair cells

Table 1. Hair cell passive properties

Cell type	Cell input Resistance GΩ	Cell input Capacitance pF	Zero current membrane potential mV
Cylinder-like			
Control (n = 98)	1.6 ± 0.1	9.8 ± 0.4	-72.3 ± 2.3
NormoG (n= 6)	2.0 ± 0.1	8.7 ± 0.7	-81.6 ± 1.6
MicroG (n = 50)	1.9 ± 0.2	10.8 ± 0.7	-73.5 ± 3.3
Pear-like			
Control (n= 40)	1.4 ± 0.2	9.9 ± 0.6	-67.1 ± 3.4
NormoG (n=7)	2.1 ± 0.4	8.2 ± 0.8	-71.8 ± 4.2
MicroG (n= 14)	1.9 ± 0.8	9.0 ± 1.9	-70.2 ± 1.2
Club-like			
Control (n= 9)	0.9 ± 0.5	9.0 ± 0.4	-72.1 ± 3.6
NormoG (n=4)	1.9 ± 0.4	10.1 ± 0.5	-73.5 ± 7.4
MicroG (n=5)	2.9 ± 0.3	8.8 ± 0.1	-68.7 ± 4.0

no indication could be obtained about the original position within the crista ampullaris; only the cell type could be recognized. The cells used in this study were classified, and their passive parameters measured, as indicated in Table 1.

These data indicate that the basic resting properties of the isolated hair cells that survived the dissection procedures were relatively homogeneous and unaffected by the previous treatments under micro-gravity or normal gravity conditions. As previously reported (Martini et al., 2009), the magnitude and kinetic properties of single ionic currents did not display any consistent differences and/or correlations in the different cell types. No further attention has been therefore paid to the specific cell type in subsequent analyses and comparisons among the experimental conditions.

Distinctive current properties

Compound currents are evoked by depolarizing the hair cell. The mix of currents that are actually activated, however, strictly depends on the membrane potential level prevailing before the depolarization; this is particularly evident for the potassium currents. A pivotal role is sustained by the transient IA; its inactivation properties rule out any IA

participation when currents are evoked from holding levels positive to -40 mV, whereas its contribution becomes progressively larger at more negative potential, as inactivation is removed. In control hair cells, command steps from a holding potential of -40 mV (as in Fig. 38 *A*) evoked summated currents comprised of inward calcium current (I_{Ca}) and two outward potassium currents (the slow I_{KV} and the calcium-dependent I_{KCa}). The compound current rapidly built-up in the tracings to a maximum value, that was monotonically related with the amplitude of the command voltage step, V_C (Fig. 38 *A*). At later times, a steady level was reached and maintained over time. This steady level increased with V_C up to +40mV, but its magnitude decreased for more positive voltages, giving rise to an "N-shaped" I-V relation (Fig. 38 *A* and 39 *A*). At very positive command potentials a component of K^+ currents rapidly set off and vanished; this component might be sustained by Ca^{2+} dependent channels, and its time course related to the kinetics of Ca^{2+} inflow, characterized by an increasingly fast onset and rapid decrease and fading as the command membrane potential approaches the Ca^{2+} equilibrium potential. In the presence of Cd^{2+} (200 μM, a powerful blocker of any voltage-dependent Ca^{2+} channels), a major fraction of the current was cancelled and the initial transient peaks at highly positive potentials were abolished, thereby confirming the role of Ca^{2+} inflow in controlling this particular feature of K^+ currents. Representative current tracings in the presence of external Cd^{2+} are shown in Fig. 38 *C*. The current time courses became homogeneous, the initial transient peak virtually disappeared, a monotonic relation of current to voltage became apparent with no sign of the "N"-behavior of control cells. The current variance, which paralleled the steady-state I-V curve in control cells, was drastically reduced by Cd^{2+}, suggesting that a major contribution to current variance arose from Ca^{2+}-activated channels (presumably BK type, in particular, due to their large conductance: the variance/mean ratio is proportional to single-channel conductance). The hair cells extracted from preparations previously exposed to micro-gravity exhibited an overall behavior reminiscent of the normal untreated cells in the presence of Cd^{2+} (Fig. 38 *B*): the I-V plot was monotonic, a small transient initial peak was present in single current tracings but no large peaks occurred at very positive potentials (Fig. 37 *B*), the "N" shape of the I-V curve was cancelled (Fig. 39 *A*), and the current variance increase with progressively positive voltage steps was small (Fig. 39 *C*).

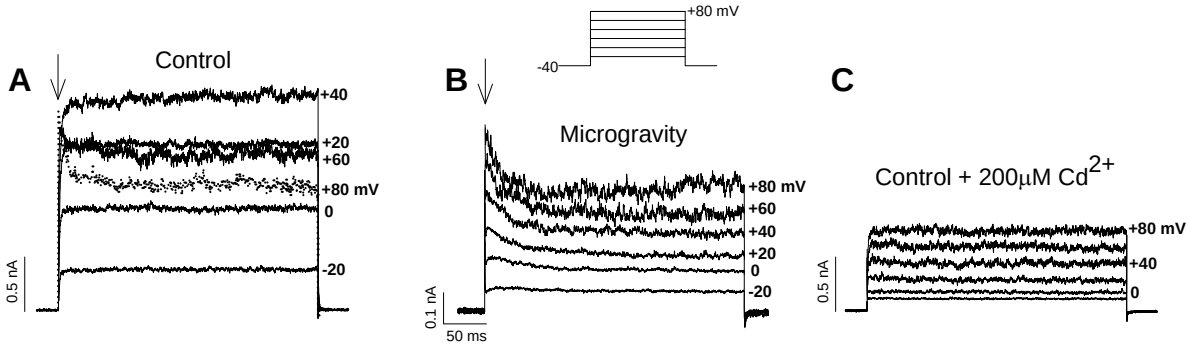

Fig. 38 **A-C**, representative families of K^+ currents evoked in the -20/+80 mV membrane potential range recorded in a control, unstimulated hair cell *A*, in a control hair cell in the presence of 200 μM Cd^{2+} in *C*, and in a cell dissociated from a preparation stimulated for 4 h under microG conditions (in *B*, notice the amplified vertical scale). Holding potential was -40 mV throughout to inactivate I_A.

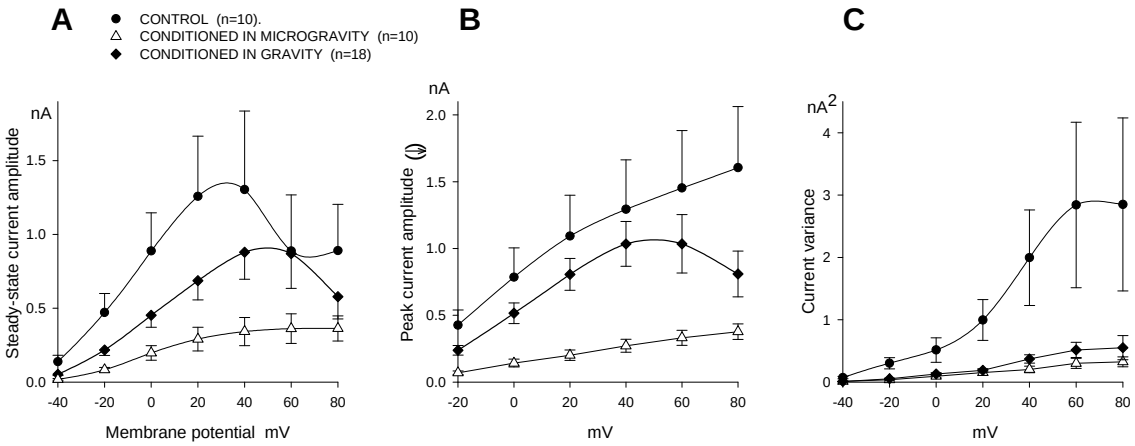

Fig. 39 **A**, I-V plots of steady-state current amplitude of hair cells dissociated from control labyrinths (circles) and from preparations preconditioned under microG (triangles) or gravity conditions (diamonds). Mean values ± SEM in a 10-18 cell sample. **B**, I-V plots of peak current amplitude (arrows in Fig. 38 *A*-*B*) measured in the same groups shown in *A*. **C**, steady-state current variance at different membrane potential levels in the same cells shown in *A*.

The hair cells dissociated from semicircular canals stimulated in the presence of gravity exhibited intermediate current properties between control and micro-gravity-conditioned cells: the "N" profile of the I-V curve was still present but less pronounced compared to controls, the early current peak at positive potentials was attenuated, and the current variance was similarly reduced.

From these data, it appeared that labyrinth stimulation produced marked changes in steady-state current amplitude. In general, for each group of cells, the standard deviation of steady state current was roughly proportional to the average, at any value of potential; thus, ANOVA was performed after homogenizing variances by logarithmic transformation of the data. The difference among treatments was confirmed (two-way ANOVA: $F = 31.0$, $P < 0.01$). In particular, stimulation under normo-gravity produced a 28% decrease (CL95 = –9-43%), compared to controls; micro-gravity conditioning resulted in a 68% decrease (CL95 = –58-76%) compared to controls, and in a 56% decrease (CL95 = –44-65%) with respect to normo-gravity. Similar results were obtained when either the amplitude of early peak ($F = 49.0$, $P < 0.01$) or the steady-state current variance ($F = 19.9$, $P < 0.01$) were considered. The transient peak amplitude was reduced by 26% (CL95 = –8.2-40 %) in gravity-conditioned hair cells, compared to controls; stimulation performed under micro-gravity conditions produced a decrease by 75% (CL95 = –67-81%) with respect to controls, and by 67% (CL95 = –58-73%) with respect to normo-gravity stimulation. The current variance also decreased with stimulation under either normo-gravity (by 81%, CL95 at least –58%) or micro-gravity (by 88%, CL95 at least –55%), with respect to control, but in this case the difference between the two stimulation conditions did not reach statistical significance. The voltage dependence of current variance also displayed a significant difference among treatments ($F = 2.2$, $P<0.01$), and in particular it was reduced after normo-gravity and even more after micro-gravity conditioning.

The calcium current

Attention was thereafter focussed on the Ca^{2+} current, which is expected to play a central role in controlling both quantal release at the cytoneural junction and the potassium conductance of the hair cell basolateral membrane. Calcium currents were readily recorded in control and micro-gravity-conditioned hair cells (two typical I_{Ca} families are illustrated in Fig. 40 *A*). They usually exhibited a large variability in amplitude and shape (14), so that a relatively large number of observations had to be collected. An initial transient current peak was in fact discernible in 17/44 control hair cells and only in 7/48

of the cells exposed to micro-gravity (statistically different frequency; chi squared test: $P < 0.001$). In all the tracings, the inward current settled to a plateau level: 78.0 ± 9.5 pA in control hair cells and significantly lower (47.0 ± 7.0 pA, $P < 0.01$) in micro-gravity-exposed cells. The histograms of the I_{Ca} amplitude distributions in control and micro-gravity-conditioned hair cells are shown in Fig. 40 *B*. The two distributions proved statistically different (Kolmogorov-Smirnov test: $D = 0.28$, $P = 0.05$), confirming that the micro-gravity conditioning produces a decrease in I_{Ca}. The average I-V plot of the nine largest I_{Ca} measured in control hair cells (circles) was compared (Fig. 40 *C*) with that of the eight smallest currents observed in micro-gravity-conditioned hair cells (triangles); in Fig. 40 *D* the same curves are normalized to the maximum current amplitude in each cell: it clearly appears that, although I_{Ca} current is much reduced, its voltage-dependence is unaffected by the micro-gravity treatment, especially in the voltage range of physiological interest (negative to 0 mV). Some differences did appear for the largest voltage commands, suggesting that control hair cells might exhibit a more positive equilibrium potential for calcium ions (E_{Ca}). This would be consistent with lower intracellular Ca^{2+} levels. It should be considered, however, that with large positivity some unspecific caesium ion permeation might occur through the calcium channels (14), so that the experimental null point of Fig. 3*C* actually reflects the balance between Ca^{2+} and Cs^{+} flows. The decrease in calcium current might thus contribute to make the apparent E_{Ca} less positive in micro-gravity-conditioned hair cells. The activation and deactivation properties of I_{Ca} have been analysed to better define possible kinetic modifications. The mono-exponential activation time constant of the current at -10 mV was 1.23 ± 0.07 ms (n = 6) in control preparations and was not altered (1.18 ± 0.15 ms) in micro-gravity-conditioned hair cells (n = 6). Current deactivation ensued with a two-exponential time course: in the same cell sample, with -10 mV command potential the fast time constant was 1.58 ± 0.30 ms in controls and 1.18 ± 0.15 ms in micro-gravity-exposed hair cells, while the slow time constant was 8.33 ± 0.65 in controls and 8.42 ± 2.19 ms after micro-gravity treatment. It would thus appear that micro-gravity results in a decrease of I_{Ca} amplitude, which is simply scaled down with respect to controls, without any relevant modification of the basic activation-deactivation processes.

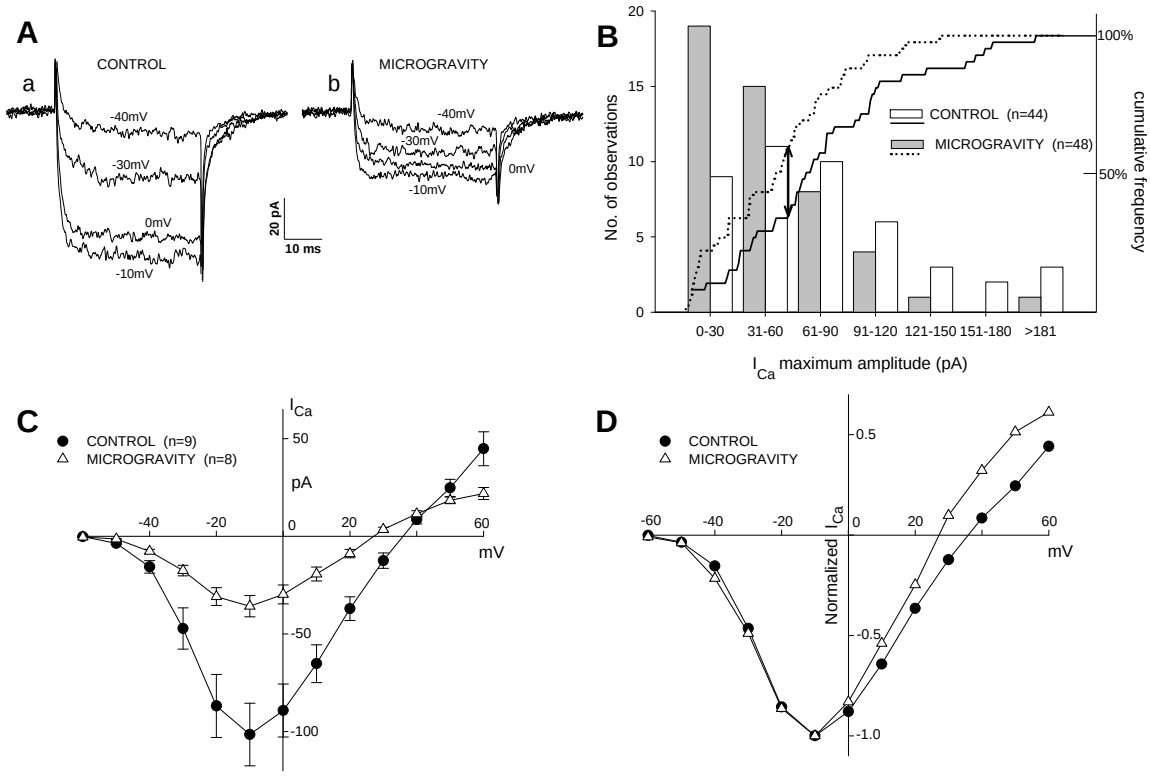

Fig. 40 **A**, typical I_{Ca} families recorded in control (**a**) and microG-conditioned hair cells (**b**) at the command potentials indicated close to each trace. Holding potential was -70 mV throughout. **B**, histograms show the distribution of the I_{Ca} maximum amplitude measured at -10 mV in control (*white*) and microG conditioned hair cells (*grey*). Continuous lines depict the cumulative distributions, that indicate a significant difference in microG vs. control (Kolmogorov-Smirnov test). **C**, I-V plots of the I_{Ca} measured in control hair cells (circles; mean of the nine largest currents of the sample) or in microG-exposed cells (triangles; mean of the eight smallest currents). **D**, normalized I_{Ca} values (the same as shown in *C*) to demonstrate the overlap of the I-V curves virtually over the whole membrane potential activation range.

Transient and persistent potassium current dissection

Hair cells express a fast transient potassium current, I_A, which is rapidly and completely inactivated at potentials above -40 mV. Hyperpolarizing conditioning pulses remove this inactivation. Following such conditioning, positive voltage pulses evoke a mix of currents in which delayed currents summate to I_A. A simple procedure to isolated the I_A component consists in subtracting the tracings without preconditioning to those obtained after preconditioning at negative potentials. This current subtraction procedure was successfully applied in the past (Belluzzi et al., 1985; Connors and Stevens, 1971), but it is valid only provided that I_{KD} does not display any inactivation. We have recently shown that the delayed current actually exhibits a slow inactivation mechanism in frog hair cells; both the development and the removal of inactivation display a slow kinetic component (time constants of several seconds) and, in addition, the slow recovery mechanism ensues with a substantial delay (Martini et al., 2009). If this aspect is not taken into account, the slow time- and voltage-dependent inactivation of I_{KD} complicates the usual procedure of IA dissection (Martini et al., 2009). However, an efficient voltage protocol can be devised to dissect and study the I_A and delayed currents in isolation, over a wide voltage range in the same cell, in the absence of any pharmacological treatment (Martini et al., 2009). An example of this procedure is illustrated in Fig. 41 for a cell previously exposed to micro-gravity conditioning.

The protocol is based on applying pairs of identical voltage steps, separated by a 300 ms sojourn at –40 mV, and exploring the range of V_C from –20 to +80 mV (Fig. 41). In *A* the cell was held for 30 s at -40 mV, to fully inactivate IA and the fraction of delayed currents that is susceptible to inactivation; the series of paired steps was subsequently applied (a and b). In Fig. 41 *B* (a different cell), a 1-s conditioning pulse at -100 mV was applied before each pair of steps, to remove inactivation of both IA and delayed currents; the two currents were thereafter evoked together in each trial (Fig. 41 *B*,cd). The interval between the two test pulses in each cycle features a sufficiently positive voltage (–40 mV) to maintain full IA inactivation and a duration which minimizes the development of slow current inactivation (due to its significant delay in onset): thus the second test pulse only evokes pure and virtually unaffected I_{KD} components. In the cell shown in *A*, the

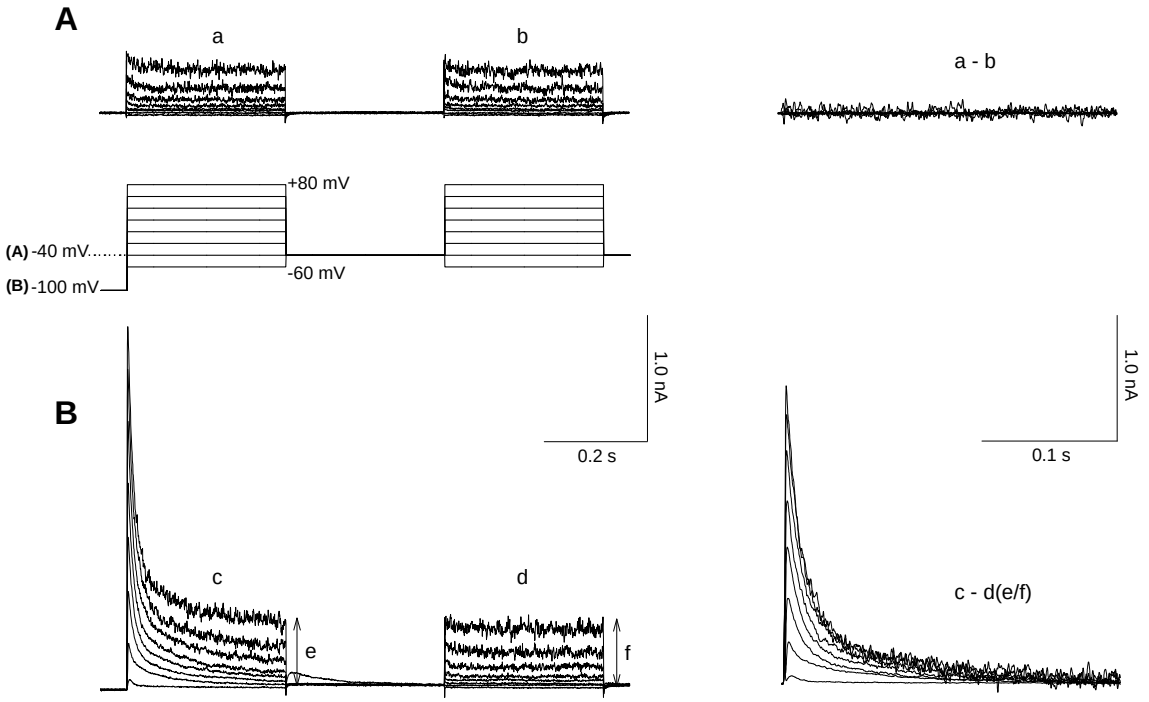

Fig. 41 Dissecting out I_A. **A**, ionic currents elicited in the -40/+80 mV voltage range from a holding potential of -40 mV (I_A fully inactivated). Two 300-ms pulses at the same test potential, separated by a 300 ms at –40 mV, were applied in each trial (a and b). The difference current is almost zero (**a – b**) for each current pair. **B**, after 1 s conditioning at -100 mV, the two-pulse series as in *A* were applied. The first pulse in each pair elicited both I_A and I_{KD} (**c**), whereas the second only evoked the I_{KD} component (**d**), because I_A had fully inactivated during the first pulse and the interposed 300 ms at –40 mV; (**e**) and (**f**) indicate the final values of current at the end of periods (**c**) and (**d**), respectively. Successive trials were separated by 30 s intervals to reset the inactivation mechanism. Subtraction of the records in Bd (after multiplying by the ratio e/f to compensate for the onset of partial inactivation of I_{KD} during 300 ms at -40 mV) from the corresponding ones in Bc dissects out the pure I_A currents.

difference current (a–b) is almost zero for any current pair. In some cells, however, a marginal amount of I_{KD} inactivation is detectable during the protocol, as revealed by a slight decrease in current amplitudes at the end of the second test pulse (Fig 41 *B*,f) with respect to the end of the first one (Fig. 41 *B*,e). The second pulse currents (Fig. 41 *B*,d) can be corrected for this slight amplitude drift, so that the difference currents (c-d·(e/f) in Fig. 41 *B*) dissect out the complete family of I_A curves in isolation.

Comparison of I_A general properties

By applying the procedure just described, separate I-V curves were obtained in control and micro-gravity-conditioned hair cells for peak I_A and maximum I_{KD} over the -50/+80 mV voltage range; they are shown in Fig. 42, *A* and *B* (control: circles; micro-gravity: triangles).

As concerns I_A, the current appeared to be significantly activated in all cells at membrane potentials more positive than -40 mV; above this value, its amplitude increased monotonically with increasing depolarization. The I-V plots of Fig. 42 *A* are virtually coincident in control and micro-gravity-conditioned hair cells. From these curves a rough estimate of the g_A conductance vs. voltage relationship was obtained by using the relation $g = I/(V - V_K)$, with $V_K = -96$ mV, as is the case for pure potassium currents. Conductance data points were fit in control hair cells by a Boltzmann-type equation with the following parameters: size, $g_{Amax} = 19.3$ nS; centre voltage, $V_{½} = -7.7$ mV; slope factor, $b = 1.1$. The corresponding values in micro-gravity-conditioned cells were $g_{Amax} = 21.1$ nS; centre voltage, $V_{½} = -14.1$ mV; slope factor, $b = 1.2$.

A first-order kinetics could be systematically detected in the current rising phase; at -40 mV the rise time constant was 2.5 ± 0.4 ms in controls (n = 9) vs. 2.3 ± 0.4 ms in micro-gravity (n = 11); its value became 1.1 ± 0.3 ms vs. 1.3 ± 0.5 ms at 0 mV; 0.8 ± 0.3 ms vs. 0.6 ± 0.1 ms at +40 mV; 0.6 ± 0.2 ms vs. 0.4 ± 0.1 ms at +80 mV.

Once activated, the I_A rapidly declined to zero, but the decay pattern was different depending on command voltage and preconditioning: the results are summarized in Fig. 44 *A*. In control and normo-gravity-conditioned cells the decay time course of the current was mono-exponential for command potentials in the range -40/+0 mV, whereas it was clearly bi-exponential at positive voltage levels in 10 out of 12 examined cells, i.e. a late slow phase of decay ensued. In micro-gravity-conditioned cells the decay of I_A was bi-exponential at all tested voltages (though the -40 mV point was ill-defined) and the mean values of the slow decay time constant were larger compared to controls (Fig. 7*A*, upper

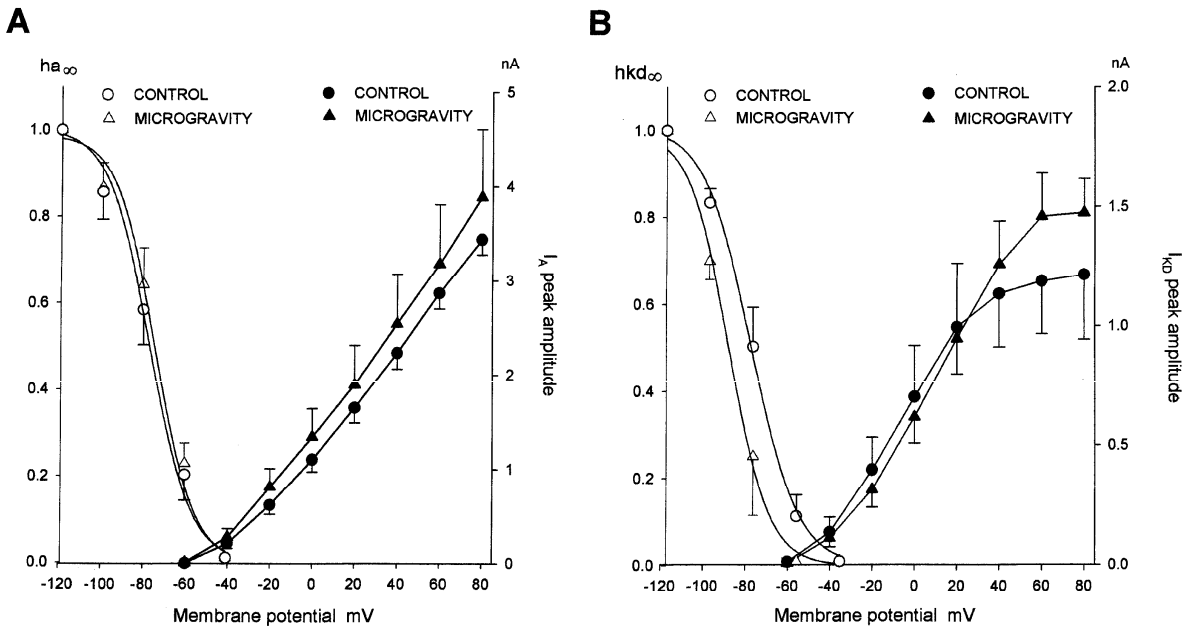

Fig. 42 **A**, mean I_A activation curve in control (solid circles, *n* = 9) and microG-exposed hair cells (solid triangles, n =10). Mean steady-state inactivation curve, ha_∞, in control (open circles, n = 7) and microG-exposed hair cells *(n* = 6). **B***:* mean I_{KD} activation curves in control (solid circles, n = 10) and microG-exposed hair cells (solid triangles, n 10). Mean steady-state inactivation curve, hkd_∞, in control (open circles, *n* =-- 6) and microG-exposed cells (open triangles, *n* 7). I_A was isolated from difference tracings according to the procedure illustrated ín Fíg. 41. Steady-state inactivation parameters were obtained from experiments similar to that illustrated in Fig. 44 *B,* by normalizing peak I_A currents, or the increment of hm above its vane at -40 mV holding potential, to their respective maximum values. *See* text for the Boltzmann-type equations best fitting the underlying conductances and steady-state inactivation curves (continuous lines).

panel). When the slowly decaying current component was present, the total charge it carried (Q_s) was always larger than that carried by the fast component (Q_f). In particular, the Q_s/Q_f ratio (indicated by the numbers in Fig. 44 *A*) was systematically larger after microG treatment than in control hair cells. In the voltage range in which the slow component was present in both groups (+20/+60 mV), ANOVA analysis showed that the slow decay time constants were statistically different ($F = 5.76$, $P < 0.05$), and in particular they increased in micro-gravity by 44% (CL95 = +10-79 %).

Comparison of I_{KD} general properties

The delayed currents were investigated either when evoked from holding potentials sufficiently positive to inactivate the I_A (-40 mV in the examples of Fig. 38) or from any more negative holding voltage level (-100 mV in Fig. 41 *B*), after applying the isolation procedure described in Fig. 41. It should be noted, however, that the -100 mV preconditioning removes not only I_A inactivation but also I_{KD} inactivation (though fractionally less relevant). As reported above, the delayed current, which was originally thought to be exempt of inactivation, exhibited a well detectable process of slow recovery from inactivation; in control hair cells such recovery only ensued after a delay of about 300 ms and developed following a single exponential time course with a time constant in the order of seconds, thereby producing a consistent final increase of I_{KD} amplitude after prolonged sojourns at well polarized potentials (Martini et al., 2009). By comparing the I_{KD} current amplitude presented in Fig. 39 *A* (holding potential –40 mV, steady state I_{KD} inactivation present) with those in Fig. 42 *B* (1s sojourn at -100 mV, partial inactivation removal), it turns out that that the typical "N" shape of steady state current vs. voltage (illustrated for control cells in Fig. 39 *A*) was attenuated by negative preconditioning, and that inactivation removal had limited effects on the amplitude of currents in control hair cells. Conversely, in microG-conditioned cells, inactivation removal brought about a dramatic increase in I_{KD} amplitude, bringing it up to values comparable to control cells (an increase by a factor of 3.1 at +0 mV, and 3.7 at +40 mV, with respect to cells held at –40 mV). It appears therefore that the steady-state I_{KD} amplitude is markedly reduced in microG-conditioned hair cells, at -40 mV, but I_{KD} inactivation mechanism becomes so sensitive to high membrane potential negativity that 1s at -100 mV is sufficient to produce a recovery of steady state current amplitude to values close to those of controls.

For mild depolarizations the current onset was usually so fast that it was hardly resolved from the capacitive transients; the peak amplitude was rapidly attained and was

maintained constant during the whole voltage step, giving a virtually rectangular shape to the tracings evoked in the range -40/+0 mV (Figs. 38, 41, 43). For large positive pulses the current time course was complicated with increasing frequency by the onset of a transient peak (Figs. 38, *A* and *B*) and/or the occurrence of a mild current decay during long-lasting pulses. This general description regards both control and microG-conditioned cells, although in the latter group six out of 22 cells exhibited a slow onset over the -20/+80 mV voltage range, with a single time constant little sensitive to voltage (9.5 ± 4.1 ms at 0 mV, 7.3 ± 1.1 ms at +80 mV).

The I-V plots of Fig. 42 *B* yield an estimate of the g_{KD} conductance-voltage relationship, which is described by a Boltzmann-type equation with the following parameters: g_{KDmax} = 7.9 nS, $V_{½}$ = -29.3 mV and b = 2.2 in control; g_{KDmax} = 9.1 nS, $V_{½}$ = –16.6 mV and b = 1.6 in microG-exposed hair cells.

Isolation and comparison of I_{KCa} amplitudes

The possible involvement of the I_{Ca}/I_{KCa} system in the microG-induced dysfunction urged a more detailed analysis of these current components. The data presented in Fig. 40 *B* indicate a significant reduction of I_{Ca} peak amplitude after microG conditioning; the differences versus the controls, however, were relatively limited, and the cell sample required to reliably quantify them so large to discourage any extension of this type of analysis to the hair cells stimulated in the presence of gravity. Thus, as an alternative approach, we preferred to consider the effect of calcium movements on the calcium-dependent potassium conductance under control-, normogravity- and microG-conditions, rather than directly studying the calcium inflow. The calcium-dependent fraction of I_{KD} in single hair cells was evaluated in a new set of experiments by applying 200 μM Cd^{2+} by fast superfusion: the difference current recorded before and after blockade of Ca^{2+} influx isolates I_{KCa} at each command potential. Considering that the apparent equilibrium potential for calcium ion is about +40 mV in these cells (Martini et al., 2000) and that the N-shaped behaviour of the compound current above this membrane potential level was not systematically observed in all the units, we analysed the I_{KCa} families in the limited range from –40 to +40 mV, with the aim of focussing on the direct priming effect of calcium inflow on the I_{KCa}, rather than on the subsequent voltage-dependent I_{KCa} development. The mean I-V curves for the pure I_{KCa} are shown in Fig. 43 A for the three experimental groups.

ANOVA was performed after homogenising variances by logarithmic transformation of the data. The difference among treatments was analysed (two-way ANOVA: F = 25.2, P

< 0.01). In particular, stimulation under normogravity produced a 21% decrease of I_{KCa}, compared to controls, but the difference between the two conditions did not reach statistical significance; micro-gravity conditioning resulted in a significant 76% decrease (CL95 > 44%) compared to controls, and in a 69% decrease (CL95 > 23%) with respect to normogravity. The distributions of the individual I_{KCa} amplitudes measured in the three groups are shown in Fig. 43 *B*; they proved statistically different (Kolmogorov-Smirnov test: $D = 0.6$, $P = 0.01$) only when comparing control and microG-conditioned hair cells, confirming that microG produced a rather specific impairment in the I_{Ca}/I_{KCa} system.

Steady-state inactivation and I_A inactivation removal

The steady-state value of the inactivation process was studied by the conventional method of varying the holding potential and depolarizing the cell to a fixed test voltage. The double step procedure illustrated in Fig. 41 dissects pure IA tracings (Fig. 44 *B*) by using the subtraction protocol and yields the corresponding families of I_{KD}. Steady-state inactivation is classically expressed by an "h_∞" parameter comprised between 0 (full inactivation) and 1 (inactivation completely removed). The steady-state inactivation curves ($h_{a\infty}$ for I_A and $h_{kd\infty}$ for I_{KD}, vs. holding potential) are illustrated in Fig. 42, *A* and *B* (open circles: control; open triangles: microG-exposed cells) and show the mean values measured for each of the two currents in individual cells (n = 6-7). To obtain $h_{a\infty}$, peak I_A currents were normalized to their largest value; for I_{KD} only the fraction subject to inactivation was considered, and $h_{kd\infty}$ was therefore computed considering only the increments of current amplitude above the values observed at -40 mV. The continuous lines through data points depict normalized Boltzmann-type equations; the coefficients of the curves fitting $h_{a\infty}$ were $V_{½} = -76.8$ mV, $b = -2.2$ in control vs. $V_{½} = -75.1$ mV, $b = -2.6$ in microG-exposed cells; for $h_{kd\infty}$ the corresponding values were $V_{½} = -80.9$ mV, $b = -2.3$ in control, vs. $V_{½} = -88.7$ mV, $b = -3.1$ in microG-exposed cells. ANOVA analysis indicated that the curves for microG-exposed hair cells were not different from control as regards $h_{a\infty}$; conversely, the difference was statistically significant for $h_{kd\infty}$ curves ($F = 7.33$, $P < 0.01$), the curve for microG-exposed hair cells being shifted to the left and inactivation removal being apparently more sensitive to voltage. The time course of removal of I_A inactivation was investigated in double-pulse experiments by holding the cells at -40 mV (I_A fully inactivated) and stepping to +20 mV after a conditioning pulse

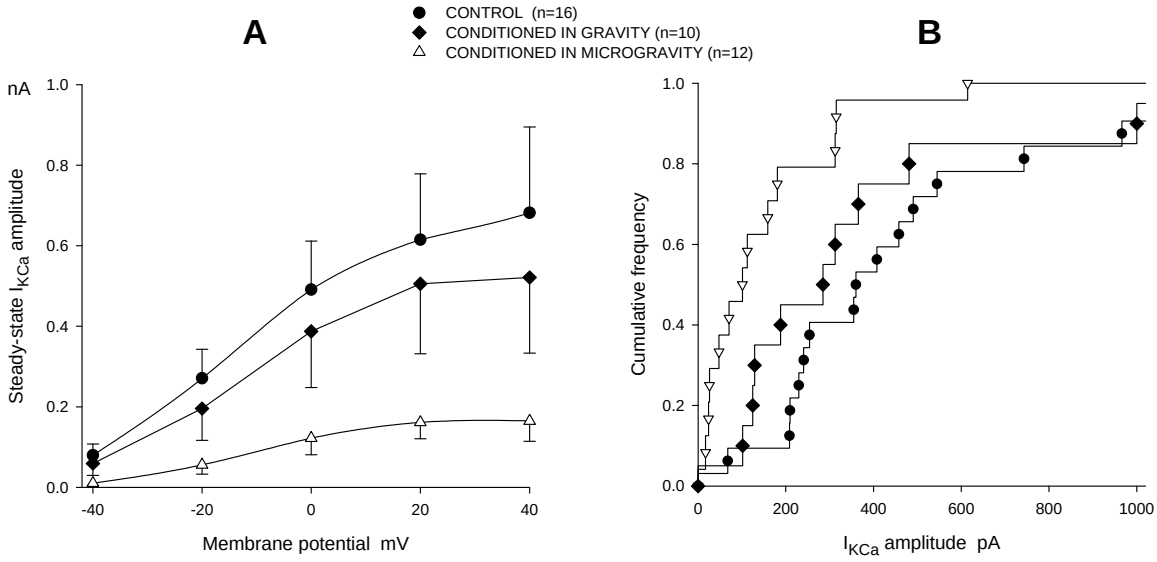

Fig. 43 **A**, I-V plots of I_{KCa} steady-state amplitude of hair cells dissociated from control labyrinths (circles) and from preparations preconditioned under microG (triangles) or gravity conditions (diamonds). Holding potential was -40 mV throughout. Mean values ± SEM in 10-16 cell samples. **B**, distribution of the I_{KCa} maximum amplitude measured at +40 mV in the same groups shown in *A*. Lines depict the cumulative distributions; a significant difference in microG vs. control is indicated by the Kolmogorov-Smirnov test.

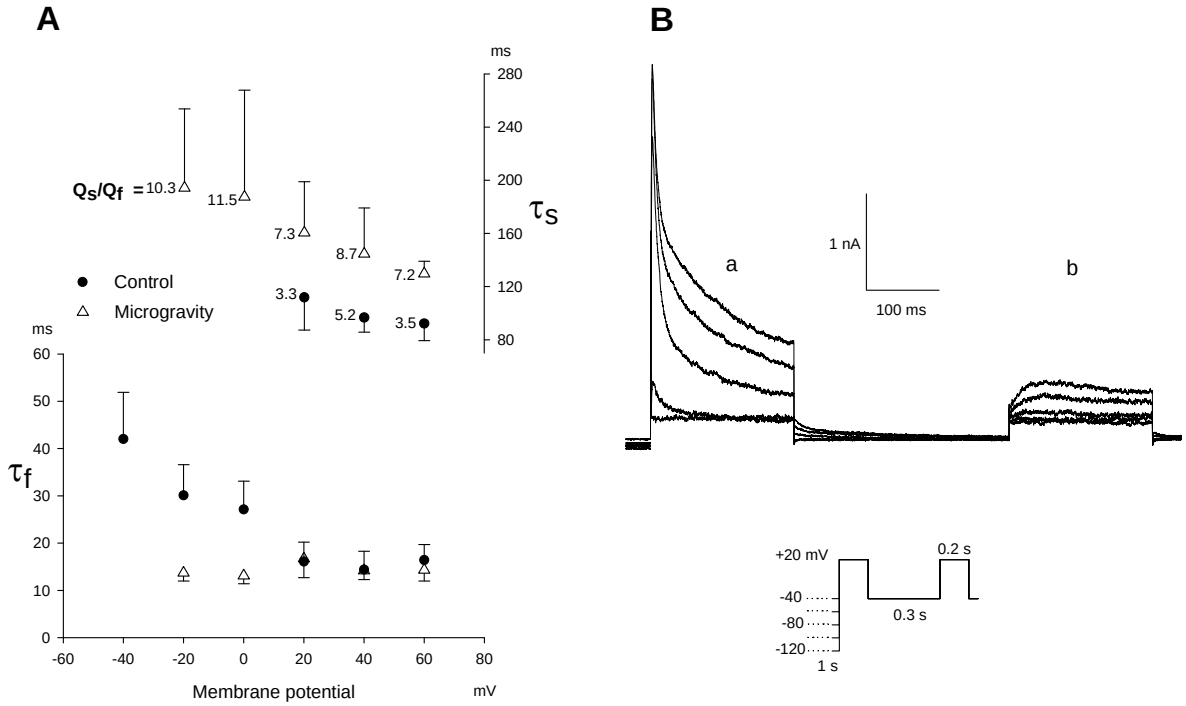

Fig. 44 **A**, I_A decay time constants in control (circles, n = 10) or microG-treated hair cells (triangles, n = 10). I_A was isolated from difference tracings according to the procedure illustrated in Fig. 41. The late (slow) decay time constant (τ_s) and the initial (fast) decay time constant (τ_f) are illustrated in the upper and lower panel, respectively. Note that the slow phase of decay was present in control cells only for command voltages >0 mV. Q_f and Q_s respectively indicate the total charge flowing during the fast and slow phases of current decay, and the numerical value of the ratio Q_s/Q_f is indicated close to each τ_s data point, in control and microG conditioned cells. **B**, measurement of steady-state inactivation in a microG-conditioned cell. Tracings illustrate currents evoked by pairs of pulses to +20 mV, separated by 0.3 s at –40 mV (to fully inactivate I_A), following 1 s conditioning in the -40/-120 mV voltage range. Both I_A and I_{KD} contribute to tracings in (**a**), whereas the sole I_{KD} contributes to tracings in (**b**). The subtraction procedure illustrated in Fig. 41 is applied to isolate the pure I_A family (not shown).

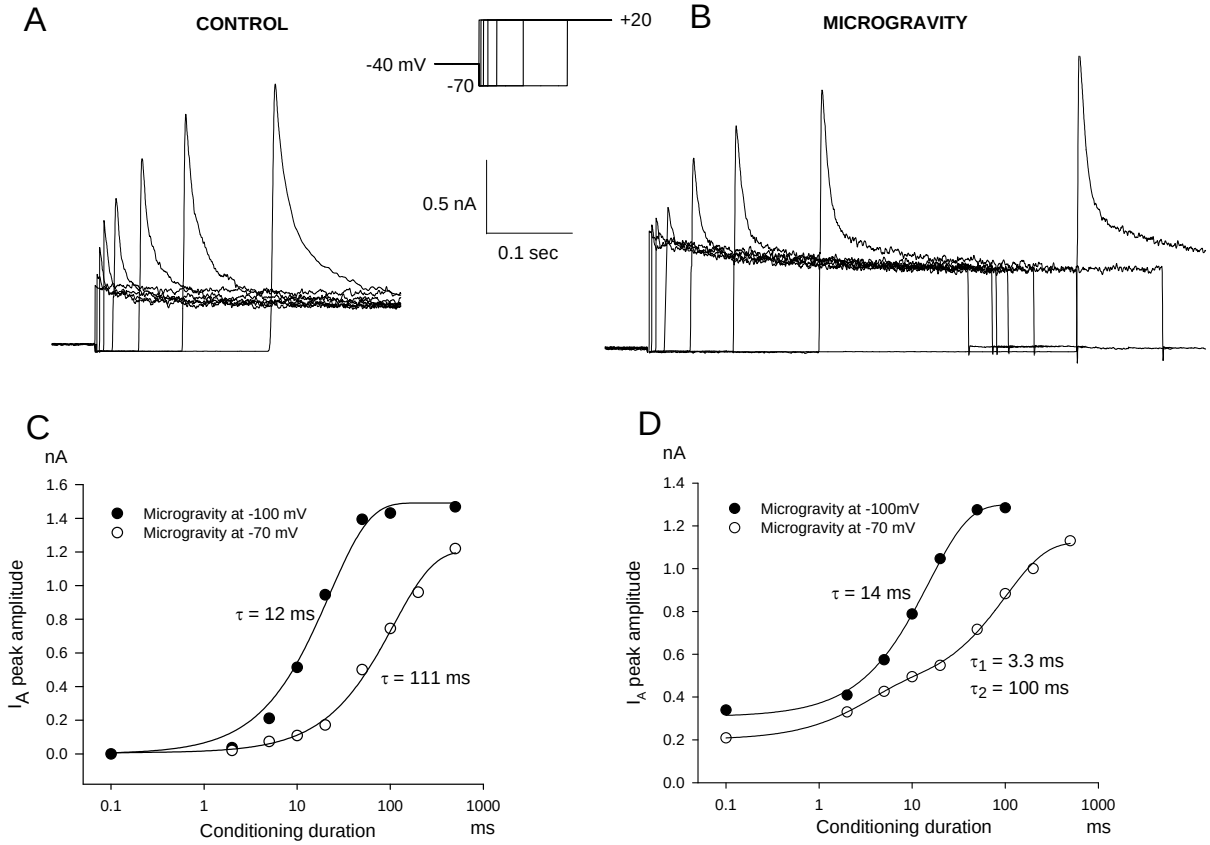

Fig. 45 **A**, time course of fast I_A recovery at -70 mV. Starting from a –40 mV holding potential (I_A fully inactivated), the currents were repeatedly elicited in a control hair cell at +20 mV following a conditioning pulse of variable duration at –70 mV. **B**, same as in *A*, in a microG-conditioned hair cell, to demonstrate the more prolonged time course of inactivation removal (time constant = 110 ms in *B* vs. 20 ms in *A*). **C**, I_A peak amplitude, recorded in the same microG-exposed cell, is plotted vs. the conditioning period duration either at -100 mV (filled circles) or -70 mV (open circles). **D**, same as *C* to show, in a different cell, the bi-exponential time course of I_A inactivation removal, together with the persistent fraction, incompletely removed at -40 mV. The best fitting lines, and the corresponding time constants, are reported close to each curve.

(at -70 or –100 mV) of variable duration. Peak I_A was computed by subtracting to these current recordings the current measured without pre-pulse. A fast process of I_A recovery (inactivation removal) was apparent, with a single exponential time course (see Fig. 45 *A*). The mean value of its time constant, τ_{hA} , was 18.2 ± 1.6 ms (n = 6) in control vs. 21.2 ± 2.0 ms (n = 8) in microG-exposed cells at -100 mV (12 ms and 14 ms in the particular examples in Fig. 45, *C* and *D*, filled circles);

fast recovery was complete within about 0.5 s in all tested hair cells, and was stable thereafter. In this same range of preconditioning pulse durations, no changes were observed in I_{KD} amplitude (see Fig. 45, *A* and *B*), thereby indicating that possible inactivation of delayed K^+ currents was not removed by brief preconditioning pulses.

I_A recovery was studied also at -70 mV, a membrane potential close to the zero-current level of the isolated cells. Again, inactivation removal ensued in controls with a single-exponential time course; the mean value of τ_{hA} = 18.3 ± 4.6 ms was virtually identical to the value observed with pre-pulses at -100 mV. Quite a different behavior was observed in microG-exposed hair cells: I_A inactivation removal became systematically slower, displaying a mean time constant of 130.9 ± 30.2 ms (n = 8). Furthermore, the time course of recovery often became more complex: in 4 out of 8 cells of the sample a second fast time constant became discernible, with a mean value of 11.7 ± 3.4 ms (an example in Fig. 45*D*, open circles). In addition, a small rapidly inactivating current (therefore identifiable as IA) was observed in 5 out of 8 cells even starting from –40 holding potential with no or very brief hyperpolarizing pre-pulse, indicating incomplete inactivation of I_A at –40 mV in these cells (see the example in Fig. 45*D*). This unexpected behavior, however, appears to be related to stimulation rather than to microG per se; in fact, similar results were observed (with -70 mV pre-pulses) in 3/8 hair cells which had been stimulated under normo-gravity conditions.

Sinusoidal voltage commands mimic the physiological membrane potential shifts

The zero current membrane potential, about -70 mV in our experiments, can be considered close to the cell membrane potential of the “silent” hair cell, i.e. in the absence of active ionic conductances and receptor current flow. This membrane potential value, however, would be obtained in the native cell only by closing the transduction channels, that are instead open at rest and maintain the cell sufficiently depolarized (in the range -50/-40 mV) to sustain a basal calcium influx which is responsible for transmitter release at the resting cytoneural junction. The membrane potential of the hair

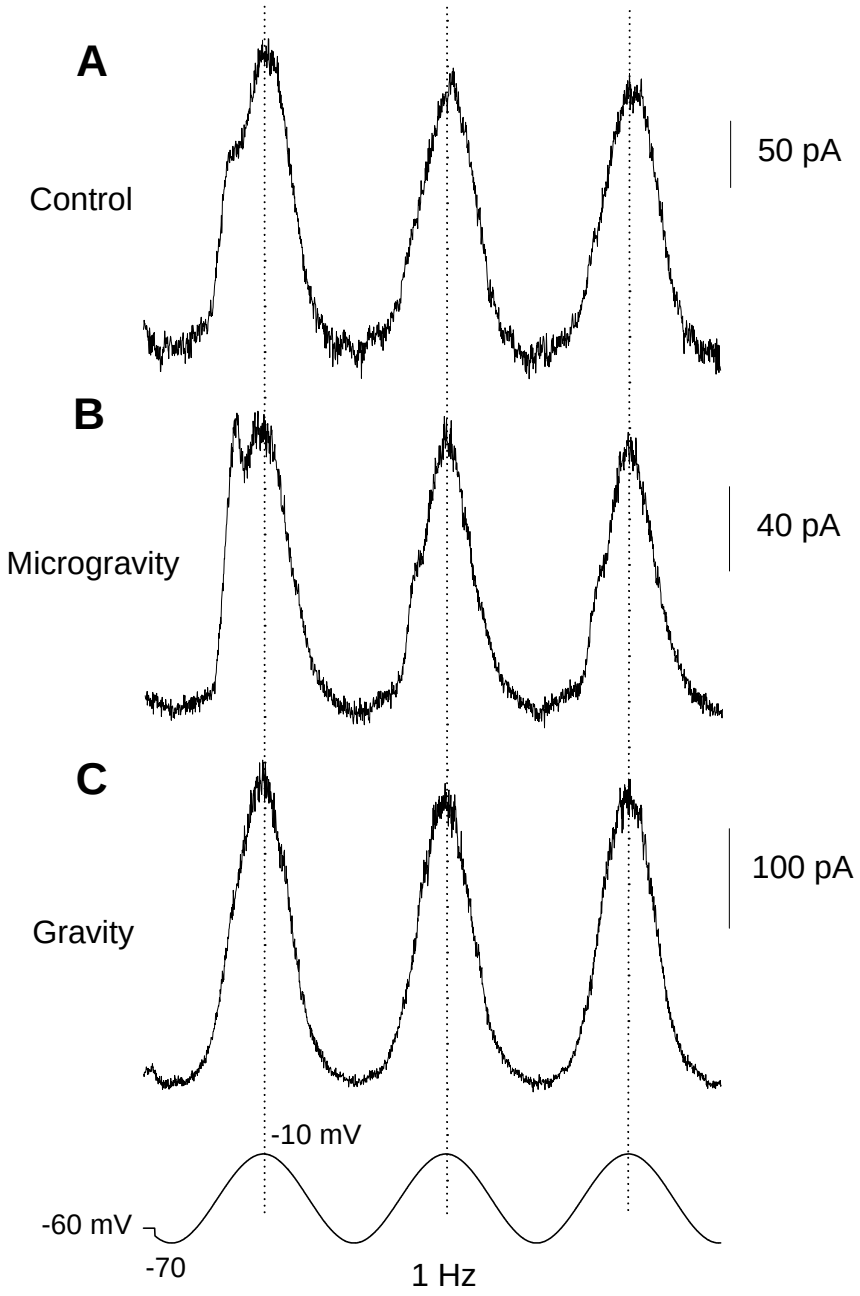

Fig. 46 Typical currents elicited by sinusoidal voltage commands mimicking the effects of a receptor potential generated by bidirectional (excitatory-inhibitory) hair bundle movements. Cells were subjected to a sinusoidal voltage command oscillating at 1 Hz from –70 mV to -10 mV. **A**, control hair cell; **B**, cell exposed to microG; **C**, cell stimulated under gravity conditions. Dotted vertical lines are centred at the positive peak of the voltage command, to help visualizing asymmetries in the rising and falling phases of the cycle (hysteresis).

cell is thus expected to fluctuate physiologically from a 'resting' status close to -40 mV (cilia in an intermediate position, a fraction of the receptor transduction channels open), towards -70 mV, when all channels are closed by the inhibitory deflection of the cupula, or towards a more positive voltage level after deflection of the sensory hair bundle and activation of additional transduction channels, during the excitatory movements of the cupula.

We mimicked the receptor potential time course by driving the hair cell membrane potential with a sinusoidal waveform that fluctuated from –70 to –10 mV, to simulate the excitatory/inhibitory deflections of the hair bundle, or from –40 to –10 mV to simulate the excitatory effects only (Fig. 46).

The currents evoked by the voltage swing down to -70 mV exhibited clear-cut asymmetries during the sinusoidal voltage shifts: the hyperpolarizing portion of the command effectively removed I_A inactivation, causing an initial excess in outward current during depolarization, due to I_A activation, that appears as a shoulder in the current profile (Fig. 46, *A* - *C*). We measured the ratio between the total outward charges evoked at membrane potential levels positive to -50 mV during the depolarizing vs. the repolarizing phase of the command (we indicated this ratio as 'hysteresis index', h.i.). Conversely, when membrane potential fluctuated within the -40/-10 mV voltage range, active currents operated during the whole cycle and the on-off phases became virtually symmetrical, since I_A was inactivated all over.

We evaluated the hysteresis index in control, either in the absence or in the presence of external Cd^{2+}, in microG and in normogravity-exposed hair cells. Representative tracings are shown in Fig. 46 (only -70/-10 mV cycles) and the results are summarized in Table 2. Direct comparison of the h.i. values shows that significant asymmetries arose systematically and exclusively during the -70/-10 mV cycles, independent of the experimental condition tested. Hysteresis was particularly prominent in control hair-cells exposed to external Cd^{2+} and in microG-conditioned hair cells. In particular, the hysteresis index in the microG group was significantly higher than in controls as well as in the gravity group (*P* values reported in Table 2).

In control cells some hysteresis was clearly evident during the first cycle, but appeared to vanish during the subsequent cycles of rotation, suggesting that at 1 Hz the 0.5 s inhibitory half cycle (and the very brief sojourn close to –70 mV) was not sufficient to remove I_A inactivation produced by the excitatory phase of the previous rotation cycle. The same occurred when stimulation in the RPM machine was performed in normal gravity conditions, whereas control cells in the presence of Cd^{2+} and cells exposed to this

Table 2. Hysteresis index evaluated in single hair cells during sinusoidal voltage command oscillating at 1 Hz in the -70/-10 mV range (three cycles) or in the -40/-10 mV range.

	Sinusoidal stimulation: -70/-10 mV			-40/-10 mV
	1st cycle	2nd cycle	3rd cycle	1st cycle
Control (n=10)	1.17 ± 0.03*	1.02 ± 0.02	0.99 ± 0.03	1.03 ± 0.03*
Control + Cd^{2+} (n=3)	1.43 ± 0.22	1.25 ± 0.19	1.20 ± 0.13	
MicroG (n=6)	1.37 ± 0.09**§	1.13 ± 0.04	1.12 ± 0.05	1.07 ± 0.04**
NormoG (n=10)	1.10 ± 0.05§	1.02 ± 0.03	1.0 ± 0.02	1.01 ± 0.02

Values are expressed as means ± SEM. Hair cells were obtained from labyrinths dissected in untreated controls, in controls exposed to 200µM Cd^{2+}, in animals previously stimulated for 4h either under microgG or under normoG conditions. The magnitude of the observed hysteresis during the -70/-10 mV cycles (1st cycle) vs. the -40/-10 mV cycle are statistically different in control and microG conditioned hair cells (*P<0.01; ** P<0.05). The hysteresis index values during the first cycle in microG vs. normoG experiments are also statistically different (§ P<0.05).

suggests that under these conditions I_A is at least partly recovered with faster kinetics. microG displayed some hysteresis during the second and third cycle of rotation as well;

This would be in agreement with the observations discussed above and illustrated in Fig. 44 *D*, i.e. with a more complex behavior of I_A recovery in micro-gravity exposed cells (a fraction of IA not inactivated at –40 mV, in some cells, and the detection of a second, fast recovery time constant that accounts for rapid recovery of about 30% of total I_A current). ANOVA analysis of the h.i. values of the three -70/-10 mV cycles in each group demonstrated a statistical difference among treatments ($F = 12.2$, $P < 0.01$) and among successive cycles ($F = 12.4$, $P < 0.01$). In particular hysteresis was more evident in micro-gravity (h.i. = 1.21) than either in control (h.i. = 1.06; difference = +0.15; CL95 = +0.07-0.22) or in normo-gravity (h.i. = 1.04; difference = +0.17; CL95 = +0.10-0.23). Hysteresis generally decreased from the first cycle (average h.i. = 1.19) to the second and third (average h.i. = 1.04; difference = –0.15; CL95 = –0.09-0.21).

When starting from -70 mV holding potential, hysteresis was evident also at command potentials that did not reach -10 mV, namely during -70/-40 mV voltage cycles (which produce minimal I_{Ca} activation and a slight but noticeable IA activation), and when calcium movements were blocked by external Cd^{2+}.

Intracellular recordings in the isolated and intact frog labyrinth

Preliminary results obtained by recording resting and evoked discharge from single fibres of the posterior nerve, in the isolated and intact frog labyrinth, show that after a 4-hour conditioning of the anaesthetized frog on the Desktop RPM both mEPSP and spike frequency decreased with respect to those evaluated in control preparations. An example of this behaviour is illustrated in Fig. 47.

A comparison of the measurements of quantal activity and spike firing in two typical units (control and microG units), at rest and during mechanically evoked activity, is graphically depicted in Fig. 48

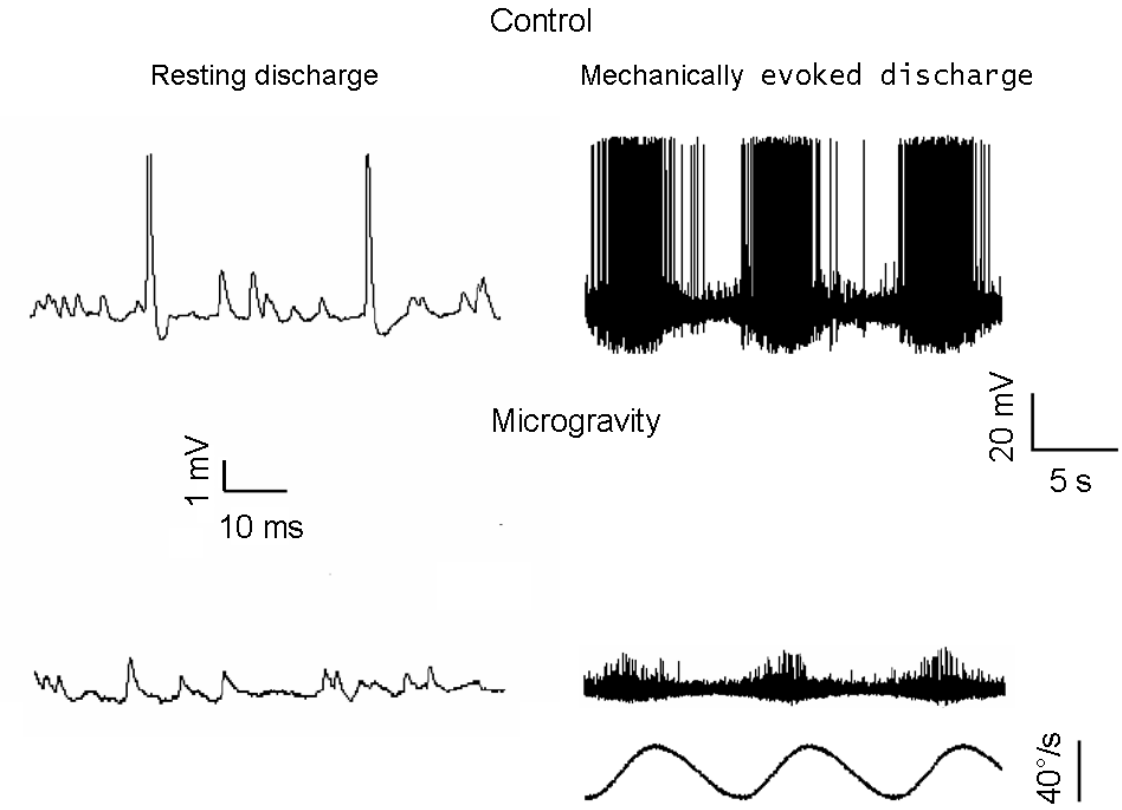

Fig. 47 Resting and mechanically evoked sensory discharge from two typical posterior canal afferent fibers in control (upper panels) and after microG treatment (lower panels). Canal stimulation is obtained by positioning the posterior canal of the intact labyrinth in the plane of rotation of a turn-table. The 0.1 Hz rotation results in a peak acceleration of 12.5°/s^2. The turn-table sinusoidal angular velocity in indicated below the recordings.

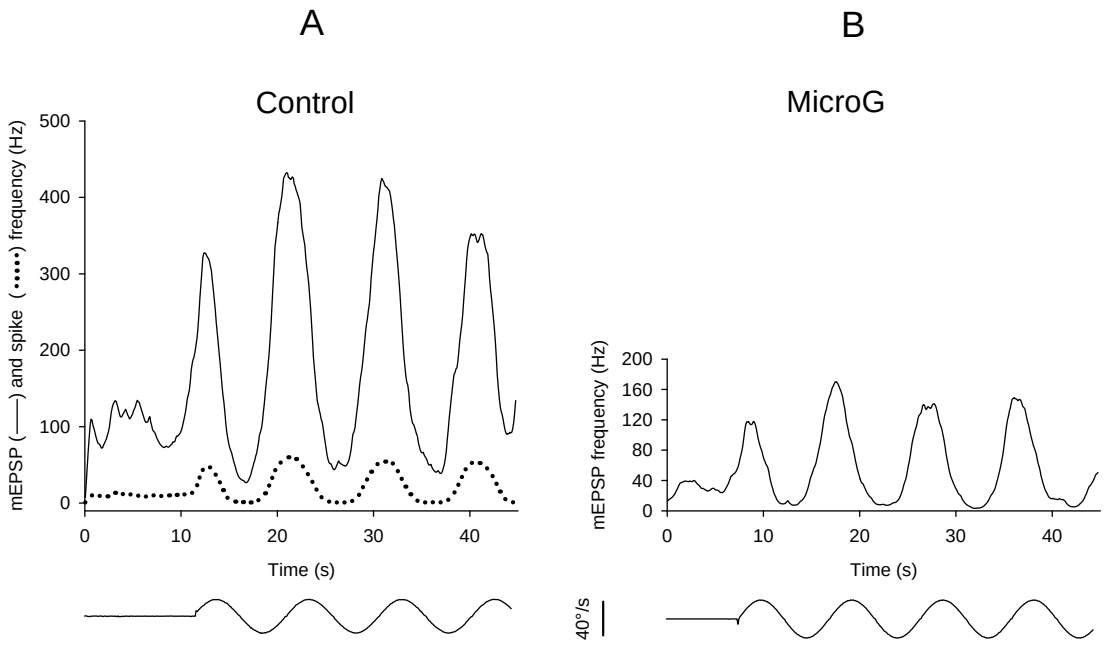

Fig. 48 Smoothed time courses (0.5 s time constant) of the sensory discharge frequency measured in two typical units at rest and during sinusoidal rotation at 0.1 Hz. **A**, mEPSP (continuous line) and spike (dotted line) frequency in a control unit. **B**, mEPSP frequency in a microG-conditioned unit in which spike firing is lacking. Note in B the low mEPSP rate at rest and during rotation. Lower traces display turntable angular velocity (deg/s).

DISCUSSION

The major targets of microG exposure appear to be the calcium/potassium current system and the I_A kinetic mechanisms. The interplay between calcium entering the hair cell and the consequent activation of the basolateral potassium calcium-dependent conductance is a well known mechanism governing the hair cell activation-deactivation cycle. We show here that the calcium current amplitude is significantly decreased in hair cells conditioned under microG conditions and that the compound delayed current I_{KV} is drastically reduced. The latter effect mirrors the actions of Cd^{2+} previously reported and confirmed here: namely, a marked decrease of the steady-state current and cancellation of the typical N-shaped behavior of the I-V curve and of the initial, transient outward peak of the current at very positive command potentials. In this concern, the data presented in Fig. 43 *AB* provide direct evidence that the I_{KCa} current fraction is actually involved in the hair cell dysfunction; they are however unable to discern between the two possibilities: the reduced calcium inflow directly generates decreased I_{KCa} activation, or the I_{KCa} failure is due to an independent basolateral cell impairment. The kinetics of I_{Ca} is apparently unaffected by exposure to microG, so that the decreased I_{Ca} might be sustained by a reduced number of calcium channels susceptible to activation by the depolarizing steps. We have no direct estimate of the relationship between amount of calcium inflow and amount of I_{KCa} activated; in auditory hair cells, it was reported that Ca^{2+} and Ca^{2+}-activated potassium channels are colocalized in such a way that the same Ca^{2+} signal that triggers transmitter release also activates BK channels (Roberts et al., 1990). Should this be case, the present suggestion that the I_{Ca}/I_{KCa} system is directly involved appears to be reasonably self-consistent. It should be noted, however, that, at variance with I_{Ca}, the I_{KD} system typically exhibits a strong inactivation mechanism, whose removal/development greatly affects the actual I_{KD} amplitude. In the hair cells exposed to microG, I_{KD} amplitude evoked from the -40 mV holding level (I_{KD} inactivation completely developed) exhibits a strong reduction (about -72% at +30 mV, compared to controls; Fig. 39 *A*). After conditioning at -100 mV (inactivation removed), however, I_{KD} amplitude becomes comparable to that of control hair cells (Fig. 42 *B*), suggesting that the kinetics of inactivation, and not the number of BK present in the membrane, are primarily involved in controlling the momentary delayed current amplitude. Additional effects of microG on I_{KD} kinetics were the negative shift of the steady-state inactivation curve and a larger sensitivity of inactivation removal to voltage.

Kinetics modifications of individual currents following microG treatment appeared to be

prominent in our experiments. For I_A, although its I-V and steady–state inactivation curves were indistinguishable between control and microG conditions, the current systematically decayed in microG according to a two exponential time course with longer time constants than in control, thus potentially providing a larger potassium charge carried by I_A. Specific dysfunctions in I_A inactivation removal were revealed in microG treated hair cells by the longer recovery time constant measured at -70 mV, further complicated in some units by the development of a two-exponential removal time course. Moreover, whereas I_A inactivation was usually fully developed at -40 mV in normal hair cells, incomplete I_A inactivation was detected in some stimulated hair cells at –40 mV. This appears to be an unexpected, but unspecific behavior, since it was related to stimulation per se rather than to microG exposure.

In summary, in labyrinthine hair cells, after stimulation under microG conditions, the following appear to be the most significant biophysical persistent effects: impairment of the I_{Ca}/I_{KCa} system, most likely sustained by reduced calcium inflow; larger fraction of I_{KD} susceptible to inactivation with a consequent drastically reduced I_{KD} fraction activatable from the -40 mV holding level; prolonged duration of I_A due to slower and biexponential decay time constants; slower removal of I_A inactivation at -70 mV. Stimulation in normo-gravity results in a minor involvement of I_{KD} and, occasionally, in the incomplete I_A steady-state inactivation at -40 mV.

The functional role sustained by each individual conductance present in the hair cell membrane, and their interactions, are far from understood. Similarly undetermined is the time course of the transduction current, either in normo- or microG conditions, and its crucial interaction with the outward current balancing its inflow. As reported above, we believe that a sinusoidal voltage command migrating in the -40/-10 mV voltage range might simulate the effects of the receptor transduction current during the excitatory deflection of the sensory hair bundle, while a -70/-10 mV range might more properly reproduce the entire excitatory/inhibitory cycle of cupula movements in the native hair cell (Martini et al., 2009).

Reduced calcium entry via voltage-dependent calcium channels is clearly linked to neurotransmitter release at the cytoneural junction; therefore, the present results adequately reflect, in principle, the preliminary electrophysiological observation, here reported, of reduced quantal emission when recording from the afferent fibers of the intact frog labyrinth, at rest or during sinusoidal 0.1 Hz stimulation. This conclusion requires some caution, as in the latter case the hair cell is not depolarized by the artificial voltage-clamp step, but rather by the interplay between the transduction current and the

voltage-dependent K^+ currents. The absence of any hysteresis during the -40/-10 mV sinusoidal cycles suggests that the reduced transmitter release at the cytoneural junction might result simply from the interaction between a decreased calcium current and an I_{KD}, reduced in turn, but still of sufficient intensity to counteract the transduction current, limiting its depolarizing effect. When wider membrane potential excursions are experienced (the -70/-10 mV range, or, in other words, during full excitatory/inhibitory actions on hair cell bundle) the additional contribution by I_A should be considered, since its activation-inactivation kinetics are now operated by voltage. During the excitatory phase of the cycle, an I_A of similar peak amplitude is likely activated after either normo- or microG conditioning (the I-V curve is virtually unaffected by microG); under the latter condition, however, an enduring contribution is expected from I_A, because of the much longer decay time constant (τ_s) of this current, exclusively observed in microG-exposed cells. Consistently, hysteresis was present in all the conditions tested during the -70/-10 mV cycles, but became much more evident in the microG exposed hair cells, compared to control and normo-gravity stimulated hair cells. Thus, the repolarizing power of the hair cell was reinforced by a stronger I_A contribution in microG-treated cells, which presumably more than compensated the decreased amplitude of the intrinsically small I_{KD}. This effect shunted the transduction current, shortened the opening time of the calcium channels and eventually decreased the transmitter release at the synaptic pole of the hair cell. Reduced calcium influx via voltage-dependent channels and increased K^+ repolarizing charge, in a variable mix according to the momentary membrane potential shifts, might thus be responsible for the failure in the afferent sensory discharge recorded in the intact labyrinth after microG conditioning.

GENERAL CONCLUSIONS

Patch clamp experiments on isolated hair cells have demonstrated both a decrease in Ca^{2+} current amplitude and a longer time constants of decay of the I_A current in microG with respect to control experiments. The reduced Ca^{2+} influx and the larger potassium charge carried by the I_A, the latter fastening the hair cell repolarization, act in synergy to reduce transmitter release at the cytoneural junction. The effect of such reduction is verified in the isolated, intact labyrinth where, after microG exposure, a decrease in mEPSP and spike frequency recorded from single afferent fibres of the posterior canal at rest and during rotatory stimulation is readily observed.

The results presented in this thesis thus reveal unexpected, clear-cut effects of micro-gravity on the functioning of the peripheral vestibular organs.

REFERENCES

Belluzzi O, Sacchi O, Wanke E. A fast transient outward current in the rat sympathetic neurone studied under voltage-clamp conditions. *J Physiol* **358**: 91-108, 1985.

Connors JA and Stevens CF. Voltage clamp studies of a transient outward membrane current in gastropod neural somata. *J Physiol* **213**: 21-30, 1971.

Fettiplace R and Ricci AJ. Adaptation in auditory hair cells. *Curr Opin Neurobiol* **13**: 446-461, 2003.

Holt JC, Lysakowski A, Goldberg JM. Mechanisms of efferent-mediated responses in the turtle posterior crista. *J Neurosci* **26**: 13180-13193, 2006.

Housley GD, Norris CH, Guth PS. Electrophysiological properties and morphology of hair cells isolated from the semicircular canal of the frog. *Hear Res* **38**: 259-276, 1989.

Housley GD, Norris CH, Guth PS. Cholinergically-induced changes in outward currents in hair cells isolated from the semicircular canal of the frog. *Hear Res* **43:**: 121-33, 1990.

Hudspeth AJ and Corey DP. Sensitivity, polarity, and conductance change in the response of vertebrate hair cells to controlled mechanical stimuli. *Proc Nat Acad Sci USA* **74**, 2407−2411, 1977.

Kennedy HJ, Evans MG, Crawford AC, Fettiplace R. Fast adaptation of mechanoelectrical transducer channels in mammalian cochlear hair cells. *Nat Neurosci* **6**: 832–836. 2003.

Kros CJ, Rüsch A, Richardson GP. Mechano-electrical transducer currents in hair cells of the cultured neonatal mouse cochlea. *Proc Biol Sci* **249**: 185-93, 1992.

Martini M, Rossi ML, Rubbini G and Rispoli G. Calcium currents in hair cells isolated from semicircular canals of the frog. *Biophys J* **78**: 1240-1254, 2000.

Martini M, Farinelli F, Rossi ML, Rispoli G. Ca^{2+} current of frog vestibular hair cells is modulated by intracellular ATP but not by long-lasting depolarisation. *Eur Biophys J* **36**: 779-786, 2007.

Martini M, Canella R, Fesce R, Rossi ML. Isolation and possible role of fast and slow potassium current components in hair cells dissociated from frog crista ampullaris. *Pfluegers Archiv* **457**: 1327-1342, 2009.

Masetto S, Russo G and Prigioni I. Differential expression of potassium currents by hair cells in thin slices of frog crista ampullaris. *J Neurophysiol* **72**: 443-455, 1994.

Norris CH, Ricci AJ, Housley GD, Guth PS. The inactivating potassium currents of hair cells isolated from the crista ampullaris of the frog. *J Neurophysiol* **68**: 1642-1653, 1992.

Ohmori H. Mechano-electrical transduction currents in isolated vestibular hair cells of the chick. *J Physiol* **359**: 189-217, 1985.

Robertson D and Paki B. Role of L-Type Ca^{2+} channels in transmitter release from

mammalian inner hair cells. II. Single-Neuron Activity. *J Neurophysiol* **87**: 2734–2740, 2002.

Rossi ML, Valli P, Casella C. Post-synaptic potentials recorded from afferent nerve fibres of the posterior semicircular canal in the frog. *Brain Res* **135**: 67-75, 1977.

Rossi ML, Prigioni I, Valli P, Casella C. Activation of the efferent system in the isolated frog labyrinth: effects on the afferent EPSPs and spike discharge recorded from single fibres of the posterior nerve. *Brain Res* **185**: 125-137, 1980.

Rossi ML, Bonifazzi C, Martini M, Fesce R. Static and dynamic properties of synaptic transmission at the cyto-neural junction of frog labyrinth posterior canal. *J Gen Physiol* **94**: 303-27, 1989.

Rossi ML and Martini M. Efferent control of posterior canal afferent receptor discharge in the frog labyrinth. *Brain Res* **555**: 123-134, 1991.

Rossi ML, Martini M, Pelucchi B, Fesce R. Quantal nature of sunaptic transmission at the cytoneural junction in the frog labyrinth. *J Physiol* **478**: 17-35, 1994.

Russo G, Calzi D, Martini M, Rossi ML, Fesce R, Prigioni I. Potassium currents in the hair cells of vestibular epithelium: position-dependent expression of two types of A channels. *Eur J Neurosci* **25**: 695-704, 2007.

Soto E, Vega R, Budelli R. The receptor potential in type I and type II vestibular system hair cells: a model analysis. *Hear Res* **165**: 35-47, 2002.

Wilson VJ and Melvill Jones G. Mammalian Vestibular Physiology, *Plenum Press* NY 1979, pages 5-76.

Zeddies DG and Siegel JH. A biophysical model of an inner hair cell. *J Acoust Soc Am* **116**: 426-41, 2004.

ACNOWLEDGEMENTS

I thank Prof. Maria Lisa Rossi, Prof. Oscar Sacchi, Dr. Marta Martini and Dr. Rita Canella for help and advice.